1 Dislocation Theory and Metallurgy

After a brief discussion of "plasticity" and "elasticity," the chapter presents a minimal set of basic concepts about "dislocations." Following an overview of dislocation theory, specific notions such as the "Lomer–Cottrell (LC) sessile junction" and "stacking fault energy" (SFE) are detailed. These are exceptionally important to gain a comprehensive understanding of many of the characteristics of dislocation–dislocation interactions and their strengths in particular. The next part of the chapter provides a simple introduction to metallurgy, especially to crystallographic structures, placing special emphasis on the substantial distinction between face-centered cubic (FCC) and body-centered cubic (BCC) structures, which is expected to further understanding of the associated contrasting features between the two.

1.1 Elasticity versus Plasticity

Let us take steel as an example to clarify the distinction between "plasticity" and "elasticity," although their names are similar. Figure 1.1.1 presents a relatively diverse range of plasticity-related mechanical properties, such as yield stress, maximum tensile stress, hardening characteristics, and ductility measured by uniform elongation. Two to three orders of difference can be found, for example, in the yield stress, that is, from tens of MPa up to a few GPa. The elastic properties such as Young's modulus, however, are not basically altered; they usually have values of around 200 GPa, even for alloys containing a number of alloying elements, those associated with metallurgical microstructures produced via heat treatments, and those with different crystal structures, that is, FCC austenite (SUS304 [or type 304] stainless steel, for instance). Such insensitivity is attributed to the origin of the elastic deformation in metals. The elastic modulus is a manifestation of the resistance against the interatomic bonding force that displaces the composing atoms, which is substantially determined by electronic interactions (hence, based on quantum mechanics). Thus, it cannot be controlled (altered) in principle. Plasticity, however, can be artificially controlled relatively easily, because it is carried by the motion of dislocations.

Further contrasting features are also indicated in Figure 1.1.1, and are summarized in Figure 1.1.2, including (a) "controllable versus uncontrollable," (b) compressive versus incompressive, and (c) conservative versus dissipative. The former is manifested as Poisson's ratio in elasticity, which is around $\nu = 0.3$ for metals, allowing

https://doi.org/10.1017/9781108874069.003 Published online by Cambridge University Press

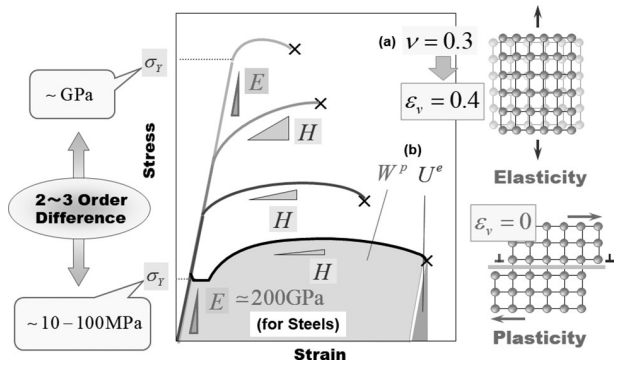

Figure 1.1.1 Schematic comparison of stress–strain curves for various steels of mild to high-strength types in terms of elastic and plastic properties. Typical contrasting features between elasticity and plasticity, (a) and (b), are also indicated.

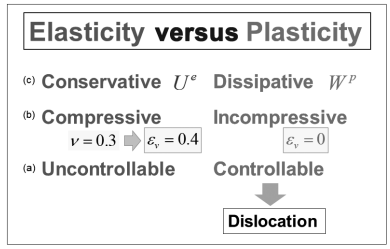

Figure 1.1.2 Comparison between "elasticity" and "plasticity," consolidated into three typical categories, where category (a) leads to the "dislocation" concept that follows.

volumetric change (e.g., tension by 1 in one direction results in −0.3 in the other two directions, respectively, resulting in a volumetric strain of $\varepsilon_v = 0.4$, that is, an increase in volume). Plasticity, on the other hand, exhibits volume constancy in general, simply because it is brought about by shear deformation, or, more precisely, slip deformation of the crystal lattice. For the latter, (b), more than 90% of the work done by plastic deformation, measured by the area swept by a stress–strain curve, is known to be dissipated into heat, meaning that plasticity is a kind of nonequilibrium (far-from-equilibrium) process, whereas elastic strain energy is fully recoverable. Note that these twofold aspects of the elastoplasticity in metals play crucial roles when we think about evolutionary aspects of inhomogeneities in the present field theory of multiscale plasticity (FTMP) (cf. Chapter 15).

1.2 Fundamentals of Dislocations

1.2.1 Overview

Figure 1.2.1 presents the reason why the notion of dislocation arose. The concept itself had been introduced many years before it was micrographically confirmed (observed),

https://doi.org/10.1017/9781108874069.003 Published online by Cambridge University Press

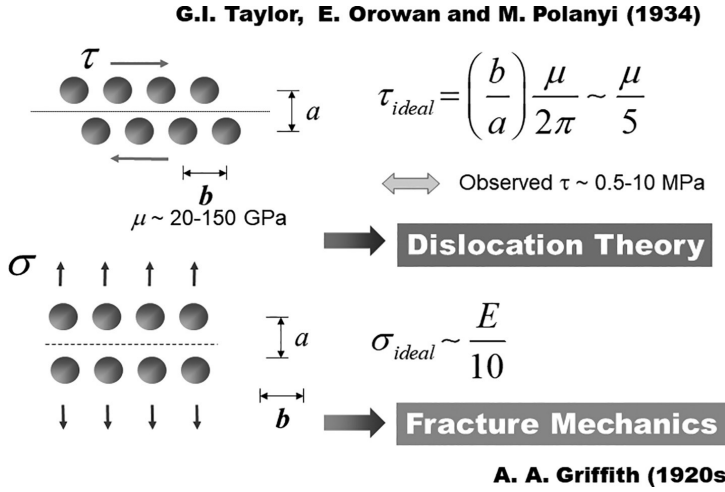

Figure 1.2.1 The extremely large gap between ideal strength for shear deformation and experimental observation for yield stress triggered the birth of dislocation theory (Taylor, 1934a). This story resembles that for fracture mechanics (Griffith, 1921).

in order to explain why the empirically observed yield stress is much smaller than the estimate based on the ideal strength under shear (Orowan, 1934a, 1934b; Polanyi, 1934; Taylor, 1934a, 1934b; Yamaguchi, 1928). The ideal strength needed for shear deformation to occur predicts one-fifth of the shear modulus, whereas experiments show 0.5–10 MPa for pure metals, resulting in a three- to four-order difference in magnitude. In the 1930s, Taylor, Orowan, and Polanyi independently advocated the concept of dislocation to explain this gap. Also, we must remember that V. Volterra, an Italian mathematician, introduced essentially the same notion purely within the framework of the mechanics of continua (Love, 1944; Volterra, 1907). This can be acknowledged as the origin of the notion of continuously distributed (CD) dislocations (cf. Figure 6.2.22). This story is quite similar to the case of the birth of "fracture mechanics"; A. A. Griffith, an English aeronautical engineer, proposed the basis for this in 1921 (Griffith, 1921).

Figure 1.2.2 indicates the motion of a dislocation, which is often compared to a crawling inchworm. Another intuitive metaphor is a row of wrinkles in a carpet. In order to shift the carpet position, what we need to do is to transfer the "wrinkle row" to the edge of the carpet, resulting in a shift of the carpet position by the amount of the wrinkle-row width. Moving the entire carpet, even a millimeter, requires extraordinary strength, as you can imagine.

The most important thing here is that plastic deformation is carried by the motion of dislocations. Accordingly, the stress needed for plastic deformation to occur can be completely replaced by that needed for moving the dislocations, which are generally preexisting within crystalline samples.

Another significant factor to bear in mind is that the plasticity (i.e., the resistance against plastic deformation) can easily be altered by introducing various "obstacles"

https://doi.org/10.1017/9781108874069.003 Published online by Cambridge University Press

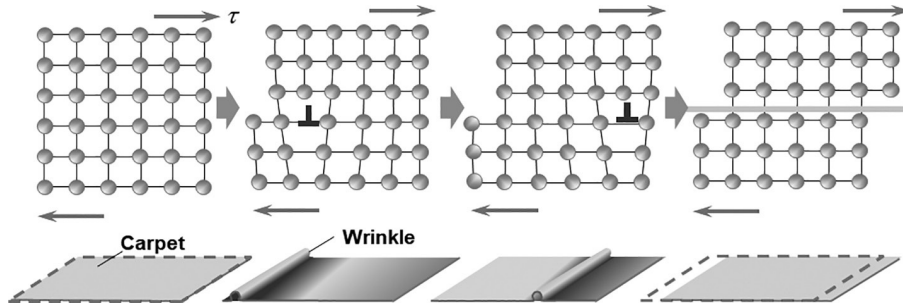

Figure 1.2.2 Schematics of a dislocation as a carrier of plastic deformation, often compared to a crawling inchworm or wrinkles in a carpet.

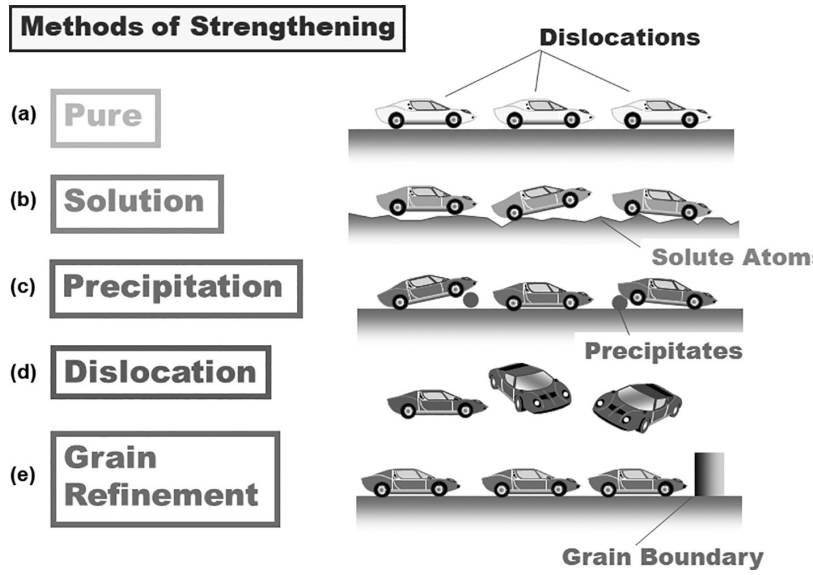

Figure 1.2.3 Schematic drawing of strengthening mechanisms showing various kinds of resistance against dislocation motion using motor vehicles as examples (inspired by an illustration by Tanino, 1966).

to obstruct dislocation movements. This means that the plasticity can be artificially controlled (or we should say, freely controllable), which is substantially different from "elasticity" that is uncontrollable in principle, as stated in Section 1.1 (see Figure 1.1.2(a)). Figure 1.2.3 illustrates representative obstacles against the motion of dislocations in a cartoonish manner (adapted from Tanino, 1996). They are (b) impurities or solute atoms for solution hardening, (c) small precipitates for precipitation hardening, (d) dislocations for dislocation hardening (resembling traffic congestion), and (e) grain boundary (GB) for GB hardening.

https://doi.org/10.1017/9781108874069.003 Published online by Cambridge University Press

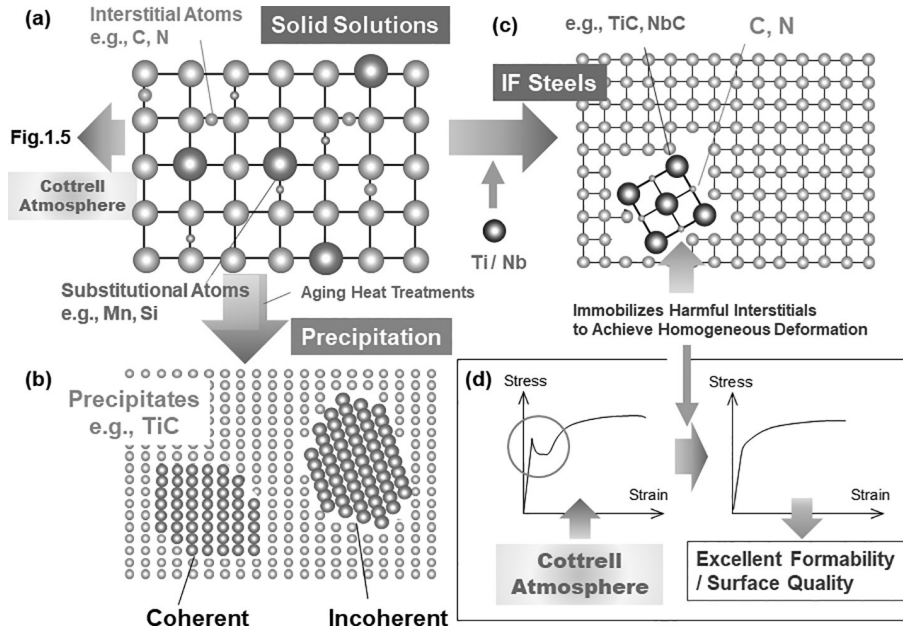

Figure 1.2.4 Schematic illustration of strengthening mechanisms via (a) solid solutions (interstitial and substitutional types) and (b) precipitations (coherent and incoherent types), together with (c) schematics about interstitial-free (IF) steel, and (d) the attendant improved stress–strain relationship with respect to "nonsmooth" yielding.

Practically, especially in high-strength steels and metals, these strengthening mechanisms are combined to achieve the desired strength properties. More detail on (b) and (c) can be found in Figure 1.2.4(a) and (b), respectively; in Figure 1.2.4(a) two types of solution, interstitial and substitutional types, are schematically depicted, while two types of precipitate are indicated in Figure 1.2.4(b), coherent and incoherent.

Figure 1.2.5 shows a schematic indicating the Cottrell atmosphere typical in commercially pure Fe or low-carbon steels, where carbon and nitrogen atoms tend to gather around (below) an edge dislocation – below because of the larger space due to the extra half plane of an atomic layer intruding from above. Under stress, trapped dislocations must break away to start moving, causing nonsmooth yielding in mild steels (Figure 1.2.4(c)), which can also trigger inhomogeneous postyield plasticity, for example, Lüders elongation, which is normally undesired in practical situations.

Note that, for steels, even a ppm order of C and/or N can cause such "yielding" phenomena in Fe and steels. Since the complete removal of them is quite difficult practically, they are inactivated by adding Ti and/or Nb to form TiC/NbC, which anchors these interstitials. Such steel is known as IF steel (Figure 1.2.4(c)) and is further detailed in Section 1.4.2.

Looking again at Figure 1.2.4(a)–(d), we can review the previous discussion, together with schematic stress–strain curves (d) indicating nonsmooth and smooth yielding, corresponding to that associated with the Cottrell atmosphere (Figure 1.2.5)

https://doi.org/10.1017/9781108874069.003 Published online by Cambridge University Press

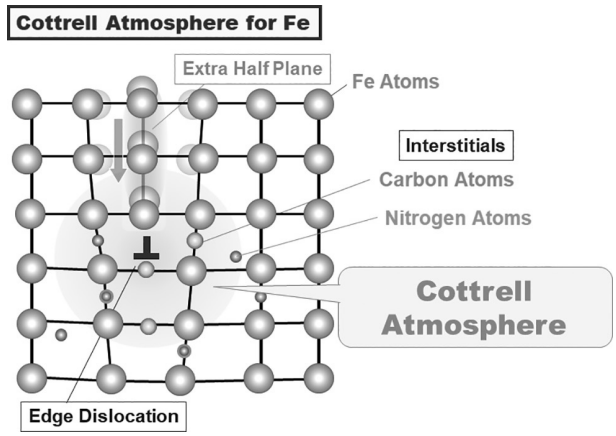

Figure 1.2.5 Schematic of Cottrell atmosphere for iron around an edge dislocation, where the insertion of an extra half plane from the top is illustrated for the purpose of emphasizing the induced compressive/tensile stress field above/below.

and IF steels, respectively, from which we also recognize the importance of impurities in metals and alloys in terms of their roles and thus their pertinent controls.

By appropriately combining the strengthening methods (b) through (e) in Figure 1.2.3, along with well-controlled heat treatment processes, we can design "microstructures" to achieve desired strength-related mechanical properties. A wide variety of such metallurgical microstructures for Fe and steels, together with typical stress–strain curves, are presented in Figure 1.2.6(a) and (b), while representative structural factors such as characteristic sizes are also indicated in Figure 1.2.6(a) (Tomota, 2001).

A noteworthy example in the present context is the lath martensite structures in high Cr heat-resistant ferritic steels, for example, Mod. 9Cr-1Mo steel, where the alloys are strengthened not only by lath martensite structures with high dense dislocations (Figure 1.2.6(a), (e), and (d)) and the associated block/packet structures (Figure 1.2.6(a) and (e)), but also by precipitations via V/Nb additions, that is, MX/$M_{23}C_6$ (Figure 1.2.6(a) and (c)), together with W/Mo solid solutions (Figure 1.2.6(a) and (b)). As noted, all the strengthening methods are combined to achieve an excellent high-temperature creep strength. One more thing worth mentioning concerns the hierarchically emerging nature of the strengths as summarized in Figure 1.2.7, revealed via the multisized indentation technique (NIMS, 2003). As can be seen, the macro-strength indicated by the broken line cannot be achieved until the indentor size becomes large enough, whereas, for example, the scale corresponding to the minute lath with high dense dislocations does not support the strength alone. This implies there exists an intimate interplay among the composing hierarchical scales for achieving the macroscopically observed strength, meaning "the partial sum is not necessarily the whole." A schematic stress–strain relationship is also shown on the right, whose stress levels are built up from the base strength. Therefore, modeling such complex material systems requires a "genuine" multiscale perspective, which is tackled in Chapter 9 and based on the FTMP discussed in the present book.

https://doi.org/10.1017/9781108874069.003 Published online by Cambridge University Press

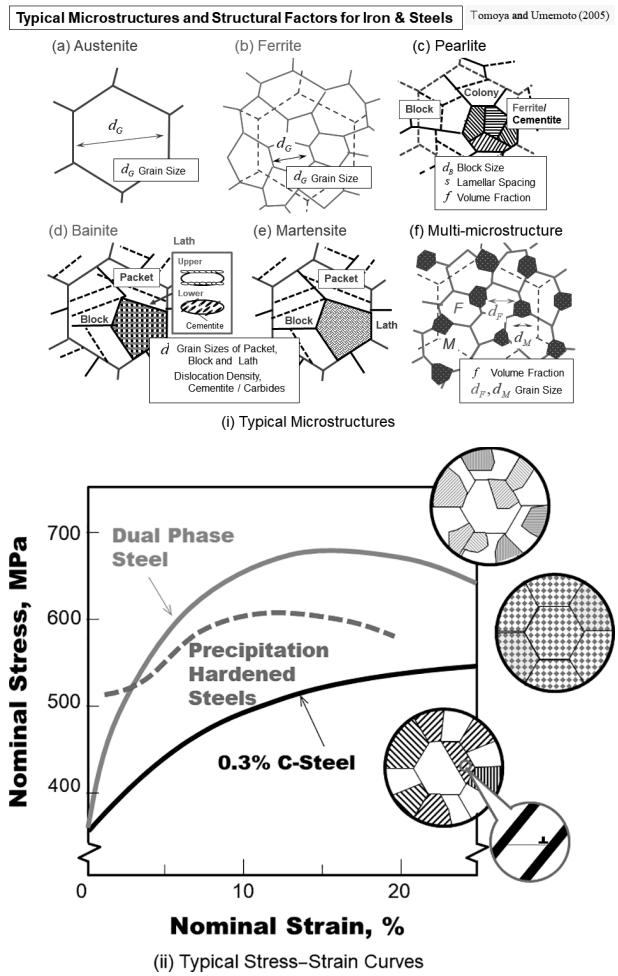

Figure 1.2.6 Typical metallurgical microstructures for Fe and steels (a) as a variety of combinations of strengthening mechanisms in Figure 1.2.3, together with typical stress–strain curves (b) for representative microstructures.

Let us return to "dislocations." Figure 1.2.8 is a micrograph showing an atomistic image of a dislocation (dislocated region). A Burgers circuit encircling the disturbed region is drawn, showing that the Burgers vector b surely exists. This proves or corroborates the single-edge dislocation existing within the circuit.

It should be noted that the notion of a dislocation "line" is conceptual in the sense that it is not a substantial object, but a "state" of being disturbed in a background (crystalline) field existing a priori. This implies that the notion of "field" is suitable for describing dislocations, as will be frequently mentioned throughout the book. A multilevel image of a dislocation field is presented in Chapter 5 (Figure 5.1.1) in terms of three representative field theories.

https://doi.org/10.1017/9781108874069.003 Published online by Cambridge University Press

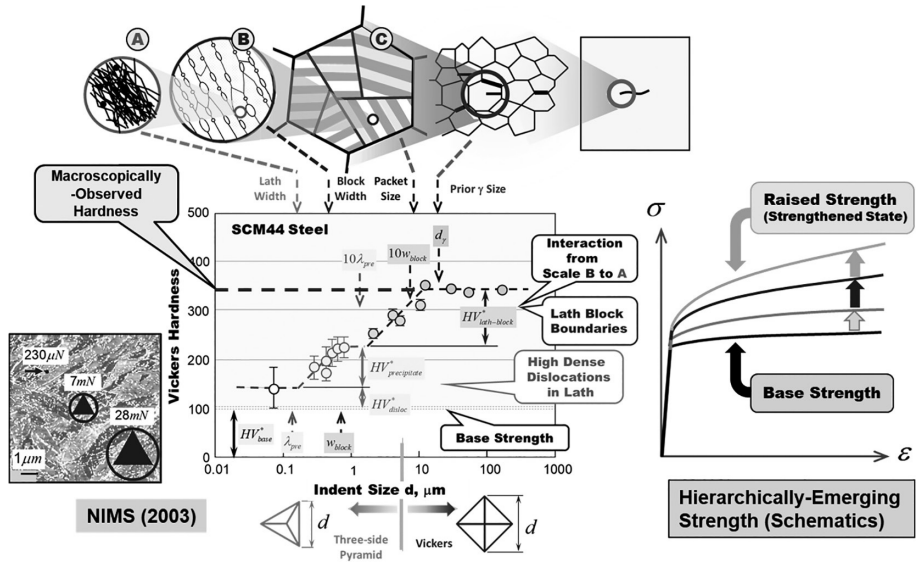

Figure 1.2.7 Example of appropriate combinations of all the strengthening methods in Figures 1.2.3 and 1.2.4, that is, high Cr ferritic steel composed of martensite lath/block/packet structures embedded within prior austenitic grains, whose hierarchically emerging strengths are revealed via multiscale indentation tests (NIMS, 2003).

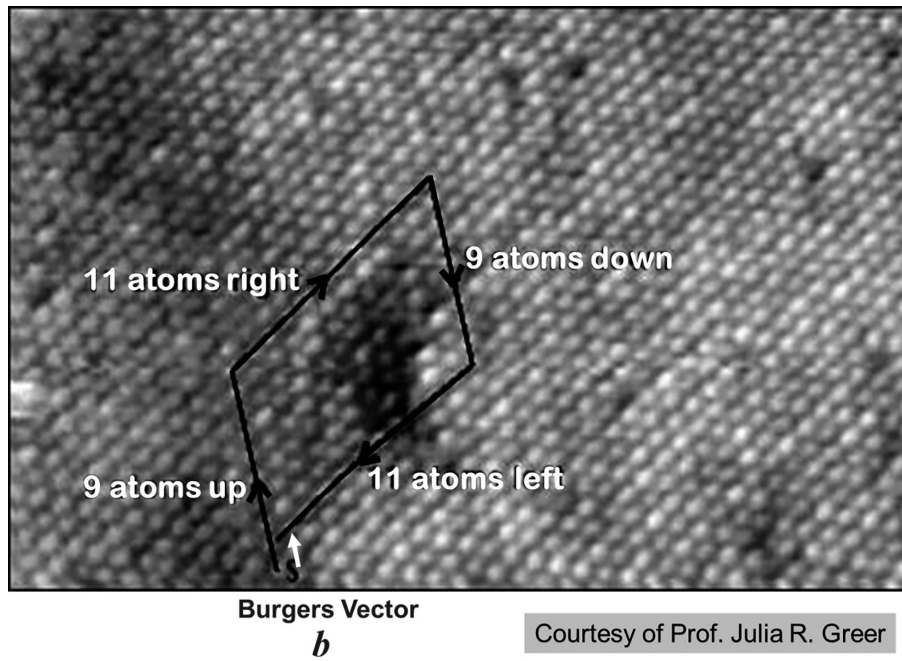

Figure 1.2.8 Atomistic image demonstrating the existence of dislocation, where the Burgers circuit encircling a dislocated region is shown to produce closure failure measured by the Burgers vector (courtesy of Prof. Julia R. Greer).

https://doi.org/10.1017/9781108874069.003 Published online by Cambridge University Press

1.2.2 Types of Dislocation

There are three types of dislocation – edge, screw, and mixed. The former two are more important than the third, since the last is expressed by combinations of the other two.

Various ways to draw or schematize an edge dislocation exist, as shown in Figure 1.2.9. Here we provide several typical examples found in conventional textbooks. Some emphasize an extra half plane (b) and some highlight the Burgers circuit or closure failure (c). Some are suitable for stress-field calculation (a). It is important to observe that the direction of the dislocation line $\boldsymbol{l}$ is always perpendicular to the Burgers vector, $\boldsymbol{b}$, that is, $\boldsymbol{l} \perp \boldsymbol{b}$, which is the mathematical definition of the edge dislocation component.

One can note that the intuitive image of the edge dislocation is quite tangible compared with the screw counterpart. However, as will be discussed later, the stress field produced around an edge dislocation is much more complex than that for the screw dislocation, and, furthermore, is difficult to calculate.

The former has both the normal and shear components of stress, whereas the latter has shear components only.

Screw dislocation is often exemplified by "stair-case steps." Figure 1.2.10 shows various schematics depicting a screw dislocation. The important thing again is the relationship between the directions of dislocation line and the Burgers vector, that is, they must be mutually in parallel, $\boldsymbol{l} \parallel \boldsymbol{b}$. This allows screw dislocations to cross slip onto other intersecting planes sharing the same Burgers vector. Also the screw dislocation is a good example for understanding the topological nature of dislocations in terms of multivaluedness. (This is also true for the edge dislocation, but the present

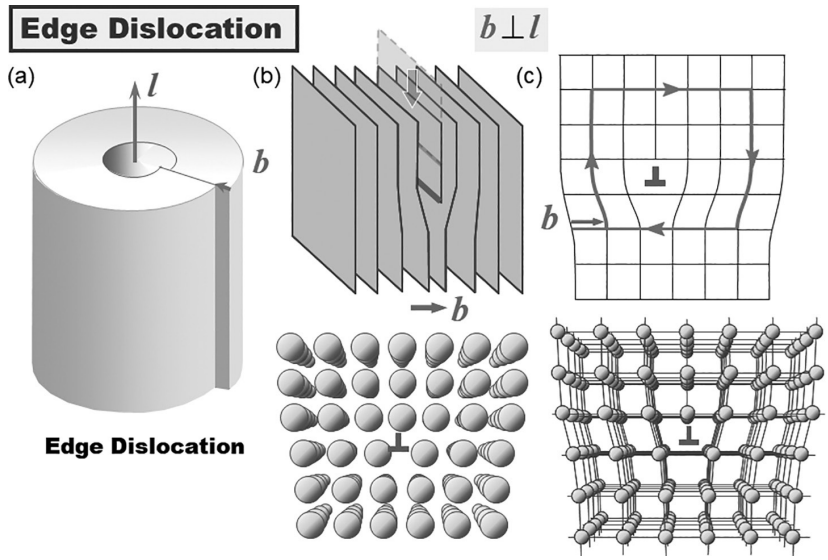

Figure 1.2.9 Various representations of an edge dislocation.

https://doi.org/10.1017/9781108874069.003 Published online by Cambridge University Press

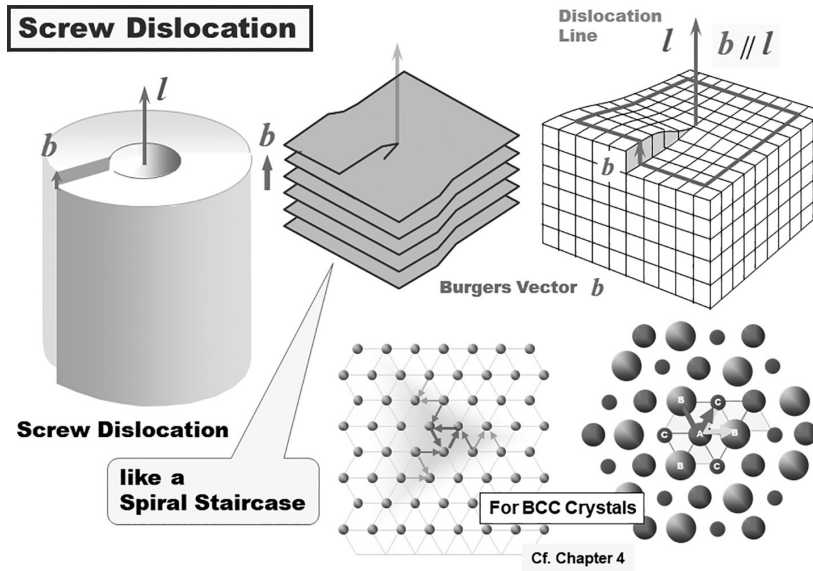

Figure 1.2.10 Various representations of a screw dislocation.

case is more intuitive.) The starting point, after encircling the Burgers circuit, does not coincide with the ending point, as can easily be confirmed with any one of the examples shown in the figure. This emphasizes that dislocation is a topological object or imperfection. It is also important for understanding the differential geometrical aspects of dislocation theory (to be detailed in Chapter 6). This closure failure means torsion of the space in the context of differential geometry.

Another type of dislocation is termed a "mixed" component. Figure 1.2.11 displays various schematics. It is usually very difficult to gain a clear image of the mixed portion of a dislocation. Fortunately, the mixed components can always be resolved into edge and screw components and expressed by combinations of the two.

As is understood from the so-called Volterra operation, explained in Figure 1.2.12, dislocation can be viewed as a region in a medium (crystalline body) where there is a boundary between "slipped" and "nonslipped" regions. Since the "slipped" region has experienced shear deformation, the distribution of shear strain for a dislocation loop becomes similar to that represented in Figure 1.2.11(b). You can notice the "strain gradients" where dislocation lines exist; this will be revisited in Section 6.5.1 (Figure 6.5.1) in Chapter 6.

One should notice the difference between real objects and dislocation as an excitation of a medium. As schematically shown in Figure 1.2.13, the screw dislocation line, for example, moves perpendicularly to the direction of the force (shear stress), which seems to be against the rule of common-sense mechanics. The edge component, on the other hand, moves in the same direction as the applied (shear) force in accordance with our intuition. The former resembles the act of peeling a poster off a wall from one corner, where the boundary between the already-peeled off and unpeeled regions corresponds to the screw dislocation. Figure 1.2.14 provides more tangible images for both cases.

https://doi.org/10.1017/9781108874069.003 Published online by Cambridge University Press

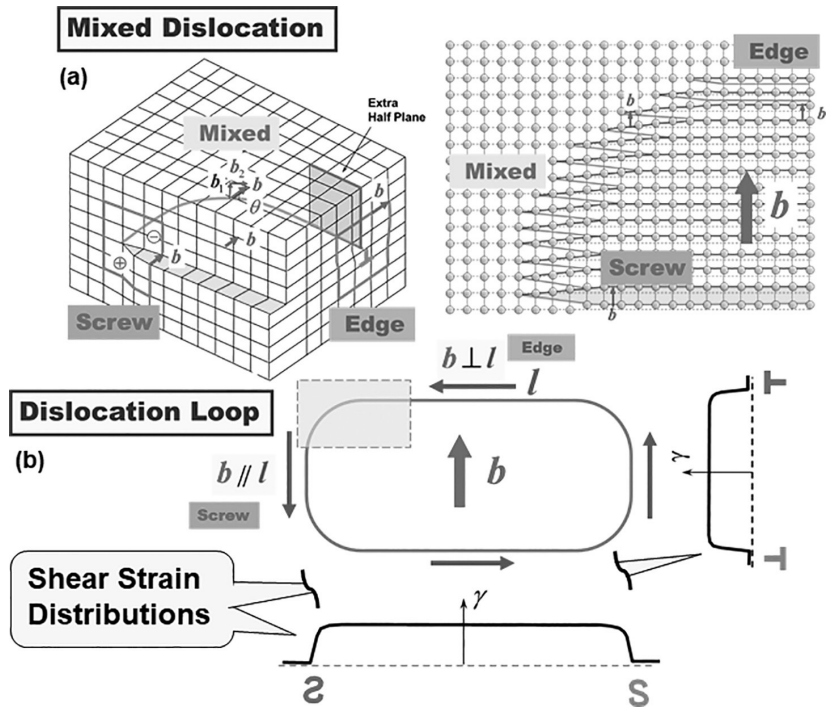

Figure 1.2.11 Schematics of a mixed dislocation (a), together with a dislocation loop and corresponding strain distribution (b), where regions with finite strain gradient detect a dislocation line.

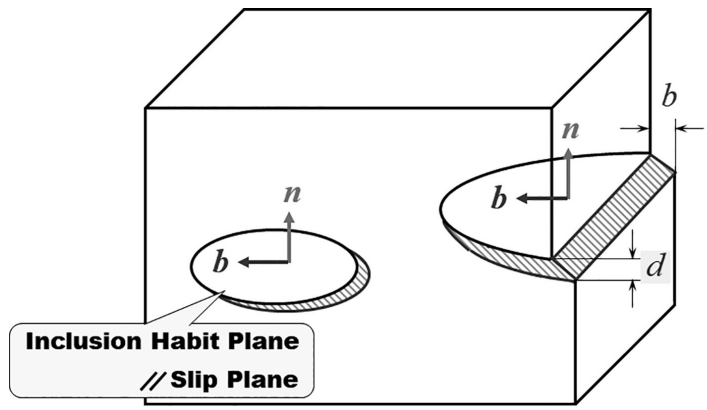

Dislocations Can be also Described as a Set of Coherent Misfitting Platelet Inclusions,

Whose Stress-Free (Misfit) Strain is an Invariant Plane Strain

$$\varepsilon^0_{ij} = \frac{b_i n_j}{d} \qquad \boldsymbol{\varepsilon}^0 = \frac{1}{d}\boldsymbol{b} \otimes \boldsymbol{n}$$

Figure 1.2.12 Schematic illustration explaining the "Volterra operation," providing another representation of the dislocation loop that can be well described mathematically based on micromechanics.

https://doi.org/10.1017/9781108874069.003 Published online by Cambridge University Press

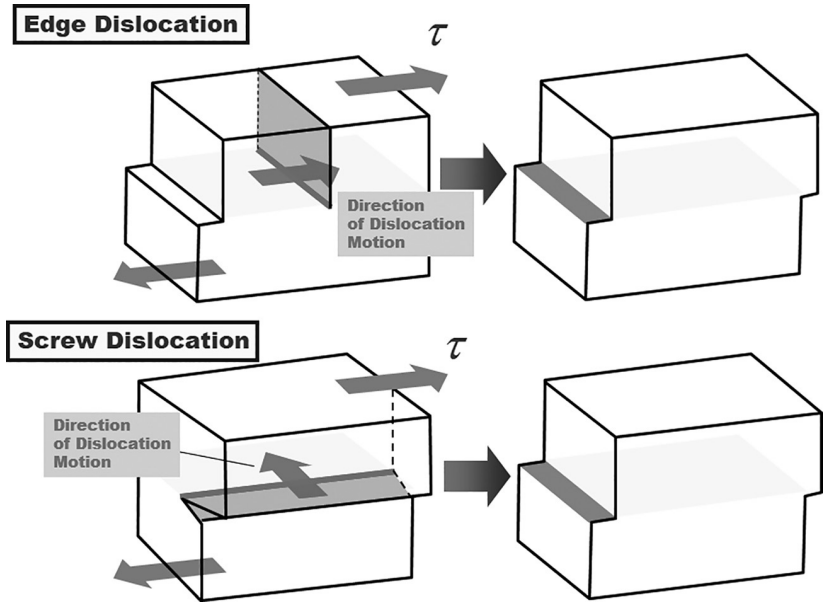

Figure 1.2.13 Comparison of moving directions between edge and screw components against external shear stress.

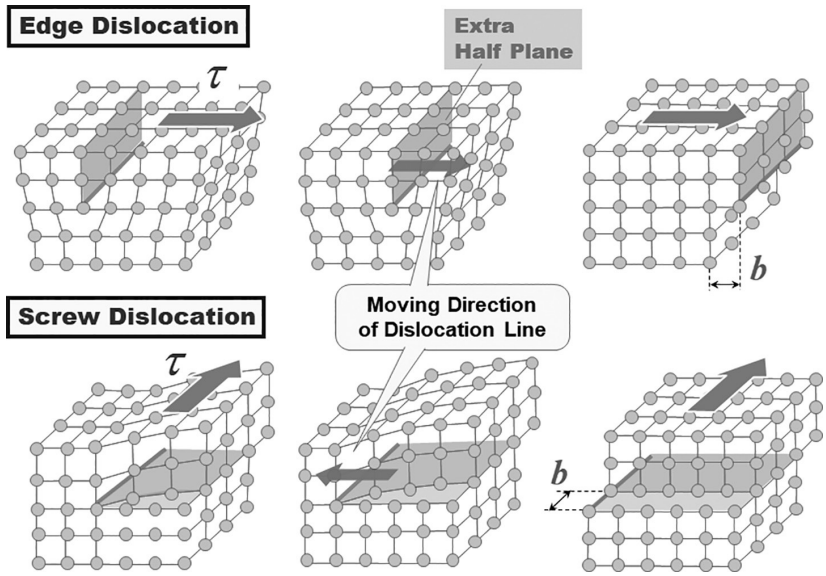

Figure 1.2.14 Atomic lattice-based representation of moving dislocations against external shear stress comparing the directions between them for edge and screw components (Smallman, 1970).

https://doi.org/10.1017/9781108874069.003 Published online by Cambridge University Press

1.2.3 Stress Field around Dislocations

One important feature of dislocations is their long-range nature, that is, inversely proportional to the distance from them r, $\propto 1/r$. Not only does this make numerical treatments difficult, for example, the "cutting-off" treatments in discrete dynamics simulations, but it also provides the origin of the long-range stress field evolved within dislocation s, differentiating them from other substructures, to be discussed in Chapter 3. Here, we deal with the most fundamental case of single straight dislocation lines.

For straight dislocations, it is relatively easy to find the stress fields around them in the sense just discussed, although the edge dislocation requires some elaborate techniques. This is largely due to the absence of the self-stress in the straight segments, whereas, for curved dislocation lines, the treatments become extremely complicated, as briefly mentioned in Section 6.4.

1.2.3.1 Screw Dislocation

To obtain the stress field around a straight screw dislocation, a typical setup, together with a cylindrical polar coordinate system (r, θ, x_3), is depicted in Figure 1.2.15, where the displaced cylinder along the axial direction coincides with x_3 is prepared, containing a coaxially extending screw-dislocation line. The displacement field in the x_3 direction is easily expressed as

$$u_3^{\text{screw}} = \frac{b}{2\pi}\theta = \frac{b}{2\pi}\tan^{-1}\left(\frac{x_2}{x_1}\right) \tag{1.2.1}$$

Otherwise, $u_1^{\text{screw}} = u_2^{\text{screw}} = 0$. From Eq. (1.2.1), the strain field and, thus, stress field, can be obtained. They are given, respectively, as

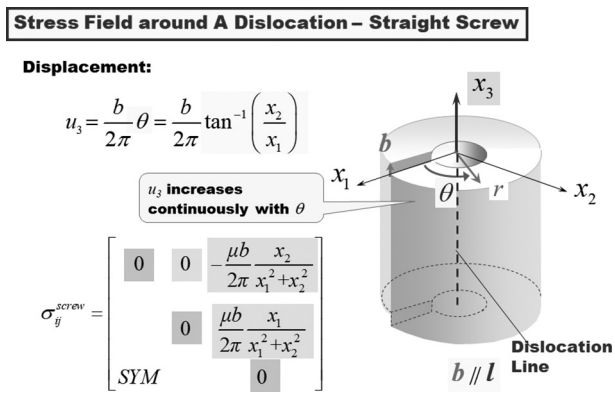

Figure 1.2.15 Cylindrical polar coordinates introduced around a straight screw dislocation, used for finding the stress field therein.

https://doi.org/10.1017/9781108874069.003 Published online by Cambridge University Press

$$\varepsilon_{ij}^{\text{screw}} = \begin{bmatrix} 0 & 0 & \frac{b}{4\pi}\frac{1}{r} \\ & 0 & 0 \\ \text{SYM} & & 0 \end{bmatrix} \tag{1.2.2}$$

and

$$\sigma_{ij}^{\text{screw}} = \begin{bmatrix} 0 & 0 & \frac{\mu b}{2\pi}\frac{1}{r} \\ & 0 & 0 \\ \text{SYM} & & 0 \end{bmatrix}, \tag{1.2.3}$$

where μ is the shear modulus and b the magnitude of the Burgers vector, $b \equiv |\boldsymbol{b}|$.

1.2.3.2 Edge Dislocation

The inset in Figure 1.2.16 shows the setup for obtaining the stress field for a straight-edge dislocation, which is basically the same as that for the screw dislocation. Since no displacement in the x_3 direction exists, we can assume the plane strain condition. In this case, even if it is straight, one needs a special sort of technique, because the treatment of the displacement field is not straightforward as in the screw counterpart: There is a jump at $\theta = \pi$ which prevents us from expressing u_1 by a simple function (unlike in the screw case), because doing so violates the stress-equilibrium condition.

To cope with this, it is necessary to use an elaborated stress-function method, in which we need to seek a suitable form of the stress function that satisfies the biharmonic equation, that is, $\nabla^4 \chi = 0$ with the Laplacian

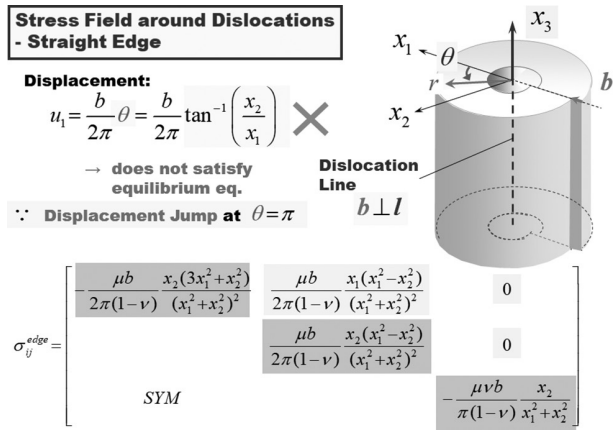

Figure 1.2.16 Cylindrical polar coordinates introduced around a straight-edge dislocation, to be used for finding the stress field therein.

https://doi.org/10.1017/9781108874069.003 Published online by Cambridge University Press

$$\nabla^2 \equiv \frac{\partial^2}{\partial r^2} + \frac{1}{r}\frac{\partial}{\partial r} + \frac{1}{r^2}\frac{\partial^2}{\partial \theta^2}, \tag{1.2.4}$$

$$\nabla^4 \equiv \Delta^2 = \left(\frac{\partial^2}{\partial r^2} + \frac{1}{r}\frac{\partial}{\partial r} + \frac{1}{r^2}\frac{\partial^2}{\partial \theta^2} \right)^2 \tag{1.2.5}$$

for the cylindrical coordinates. For the edge dislocation problem, the following form of the stress function can be used:

$$\begin{aligned} \chi(r,\theta) = R(r)\phi(\theta) &= \frac{\mu b}{2(1-\nu)} r \sin\theta \ln r \\ &= \frac{\mu b}{2(1-\nu)} y \ln\left(x^2 + y^2\right)^{1/2}, \end{aligned} \tag{1.2.6}$$

from which we readily obtain

$$\begin{cases} \sigma_{rr} = \sigma_{\theta\theta} = -\dfrac{\mu b}{2(1-\nu)} \dfrac{\sin\theta}{r} \\ \sigma_{r\theta} = \sigma_{\theta r} = \dfrac{\mu b}{2(1-\nu)} \dfrac{\cos\theta}{r} \end{cases}. \tag{1.2.7}$$

In Eq. (1.2.6), $R(r)\phi(\theta)$ is intended to emphasize the separable nature of the stress function, in this case via respective functions of r and θ. Since the present case satisfies the plane-strain condition, another component is given by $\sigma_{zz} = \nu(\sigma_{rr} + \sigma_{\theta\theta})$.

Note that a more sophisticated method based on micromechanics is also available (Mura, 1963). For the anisotropic case, refer, for example, to Asaro et al. (1973) and Willis (1970).

The stress field around a straight-edge dislocation is rewritten in matrix form as

$$\sigma_{ij}^{\text{edge}} = \begin{bmatrix} -\dfrac{\mu b}{2\pi(1-\nu)} \dfrac{\sin\theta}{r} & \dfrac{\mu b}{2\pi(1-\nu)} \dfrac{\cos\theta}{r} & 0 \\ & -\dfrac{\mu b}{2\pi(1-\nu)} \dfrac{\sin\theta}{r} & 0 \\ \text{SYM} & & -\dfrac{\mu \nu b}{\pi(1-\nu)} \dfrac{\sin\theta}{r} \end{bmatrix}, \tag{1.2.8}$$

where not only the shear component (off-diagonal) but also the normal components (diagonal) exist. Detailed derivation processes can be found in Hirth and Lothe (1982), Kato (1999) and Suzuki (1967).

The corresponding expressions to Eqs. (1.2.3) and (1.2.8) with respect to the Cartesian coordinates are given by

$$\sigma_{ij}^{\text{screw}} = \begin{bmatrix} 0 & 0 & -\dfrac{\mu b}{2\pi} \dfrac{x_2}{x_1^2 + x_2^2} \\ & 0 & \dfrac{\mu b}{2\pi} \dfrac{x_1}{x_1^2 + x_2^2} \\ \text{SYM} & & 0 \end{bmatrix} \tag{1.2.9}$$

and

https://doi.org/10.1017/9781108874069.003 Published online by Cambridge University Press

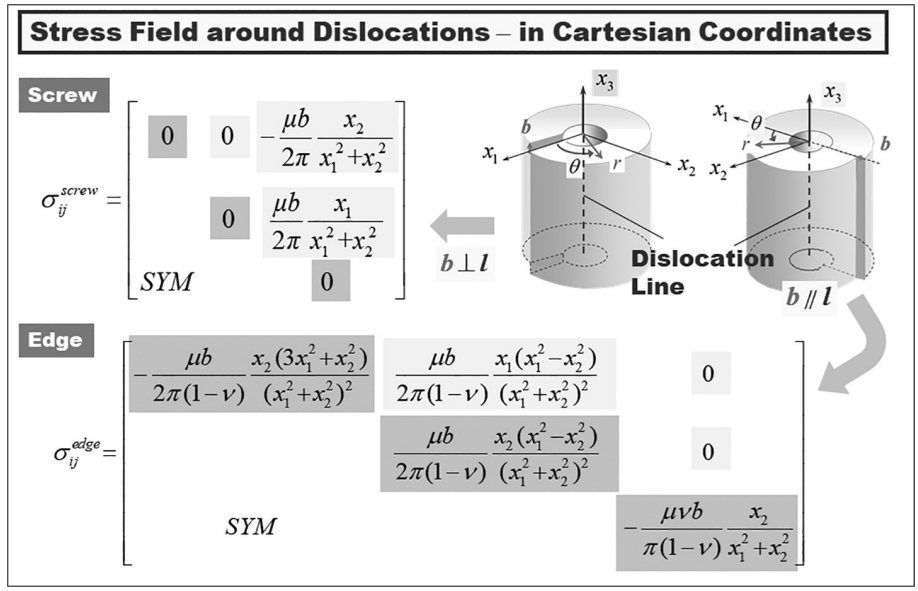

Figure 1.2.17 Stress field around straight screw and edge dislocations with respect to the Cartesian coordinate system.

$$\sigma_{ij}^{\text{edge}} = \begin{bmatrix} -\frac{\mu b}{2\pi(1-\nu)}\frac{x_2(3x_1^2+x_2^2)}{(x_1^2+x_2^2)^2} & \frac{\mu b}{2\pi(1-\nu)}\frac{x_1(x_1^2-x_2^2)}{(x_1^2+x_2^2)^2} & 0 \\ & \frac{\mu b}{2\pi(1-\nu)}\frac{x_2(x_1^2-x_2^2)}{(x_1^2+x_2^2)^2} & 0 \\ \text{SYM} & & -\frac{\mu\nu b}{\pi(1-\nu)}\frac{x_2}{x_1^2+x_2^2} \end{bmatrix}, \quad (1.2.10)$$

respectively. These results are summarized in Figures 1.2.17 and 1.2.18.

One of the most important aspects for us to recognize about the stress fields produced by a dislocation is its long-range nature, for example, decaying in proportion to $1/r$ (see Eqs. (1.2.3) and (1.2.8)). This actually introduces many computational complexities in dealing with dislocation-dislocation interactions (see also Section 1.4.4).

The corresponding strain fields are

$$\varepsilon_{ij}^{\text{screw}} = \begin{bmatrix} 0 & 0 & -\frac{b}{4\pi}\frac{x_2}{x_1^2+x_2^2} \\ & 0 & \frac{b}{4\pi}\frac{x_1}{x_1^2+x_2^2} \\ \text{SYM} & & 0 \end{bmatrix} \quad (1.2.11)$$

and

https://doi.org/10.1017/9781108874069.003 Published online by Cambridge University Press

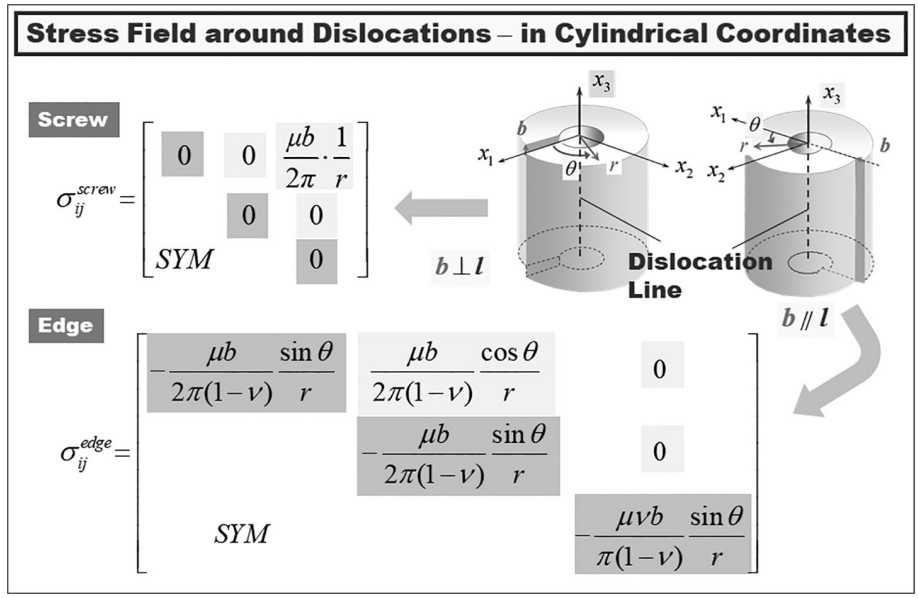

Figure 1.2.18 Stress field around straight screw and edge dislocations with respect to the cylindrical polar coordinate system.

$$\varepsilon_{ij}^{\text{edge}} = \begin{bmatrix} -\frac{b}{2\pi}\frac{x_2\left\{(2\lambda+3\mu)x_1^2+\mu x_2^2\right\}}{(\lambda+2\mu)(x_1^2+x_2^2)^2} & \frac{b}{2\pi(1-\nu)}\frac{x_1(x_1^2-x_2^2)}{(x_1^2+x_2^2)^2} & 0 \\ & \frac{b}{2\pi}\frac{x_2\left\{(2\lambda+\mu)x_1^2-\mu x_2^2\right\}}{(\lambda+2\mu)(x_1^2+x_2^2)^2} & 0 \\ \text{SYM} & & 0 \end{bmatrix} \tag{1.2.12}$$

The displacement field is obtained when the strain field in Eq. (1.2.12) is integrated as

$$\begin{Bmatrix} u_r^{\text{edge}} \\ u_\theta^{\text{edge}} \\ u_z^{\text{edge}} \end{Bmatrix} = \frac{b}{2\pi}\begin{Bmatrix} -\frac{(1-2\nu)}{2(1-\nu)}\sin\theta\ln r + \frac{\sin\theta}{4(1-\nu)} + \theta\cos\theta \\ -\frac{(1-2\nu)}{2(1-\nu)}\cos\theta\ln r - \frac{\cos\theta}{4(1-\nu)} - \theta\sin\theta \\ 0 \end{Bmatrix} \tag{1.2.13}$$

For Cartesian coordinates, the corresponding expression is

$$\begin{Bmatrix} u_1^{\text{edge}} \\ u_2^{\text{edge}} \\ u_3^{\text{edge}} \end{Bmatrix} = \frac{b}{2\pi}\begin{Bmatrix} \tan^{-1}\frac{x_2}{x_1} + \frac{x_1x_2}{2(1-\nu)(x_1^2+x_2^2)} \\ \frac{1-2\nu}{4(1-\nu)}\ln(x_1^2+x_2^2) + \frac{x_1^2-x_2^2}{4(1-\nu)(x_1^2+x_2^2)} \\ 0 \end{Bmatrix} \tag{1.2.14}$$

https://doi.org/10.1017/9781108874069.003 Published online by Cambridge University Press

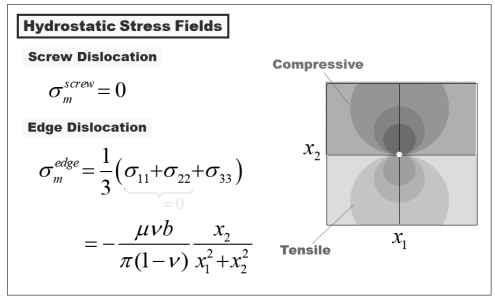

Figure 1.2.19 Hydrostatic stress distribution around screw and edge dislocations. Nonzero hydrostatic stress for edge components brings about interactions with point obstacles.

1.2.3.3 Stress Contours

Let us consider the hydrostatic stress $\sigma_m \equiv (\sigma_{11}+\sigma_{22}+\sigma_{33})/3$ for both the components as a representative. Figure 1.2.19 shows the hydrostatic stress fields for both the dislocations. Screw dislocation always yields zero hydrostatic stress, that is,

$$\sigma_m^{\text{screw}} = 0, \tag{1.2.15}$$

simply because of the absence of the normal component of stress, as in Eqs. (1.2.3) or (1.2.9).

For edge dislocation, on the other hand, the hydrostatic stress is calculated as

$$\sigma_m^{\text{edge}} = -\frac{\mu b}{3\pi}\left(\frac{1+\nu}{1-\nu}\right)\frac{x_2}{x_1^2+x_2^2} \tag{1.2.16}$$

One can immediately notice that this is in proportional to the σ_{33} component. Therefore, the hydrostatic stress field around a straight-edge dislocation, displayed in the inset of Figure 1.2.19, is identical to that for σ_{33}, as far as the profile is concerned. As can be imagined from the atomic configuration, we have a compressive stress field in the upper region, due to the insertion of an extra atomic layer, and a tensile stress field in the lower region. The latter tends to attract interstitials, as discussed in Figure 1.2.5 in the context of the Cottrell atmosphere.

1.2.4 Elastic Strain Energy of Dislocations

Based on the stress field we have just obtained, we can evaluate the strain energy for the dislocations (Figure 1.2.20). For a straight screw dislocation extending infinitely along the x_3 direction, we have

$$\begin{aligned} E^{\text{screw}} &= \frac{1}{2}\int_{V\to\infty} \sigma_{ij}^{\text{screw}}\varepsilon_{ij}^{\text{screw}}\,dx \\ &= \frac{1}{2}\int_0^{2\pi} d\theta \int_{r_0}^{R} dr \int_{-\infty}^{\infty} dx_3 \left(\sigma_{\theta x_3}^{\text{screw}}\varepsilon_{\theta x_3}^{\text{screw}}\right), \\ &= \frac{1}{2}\int_0^{2\pi} d\theta \int_{r_0}^{R} dr \int_{-\infty}^{\infty} dx_3 \left(\frac{\mu b^2}{8\pi^2 r^2}\right) \end{aligned} \tag{1.2.17}$$

https://doi.org/10.1017/9781108874069.003 Published online by Cambridge University Press

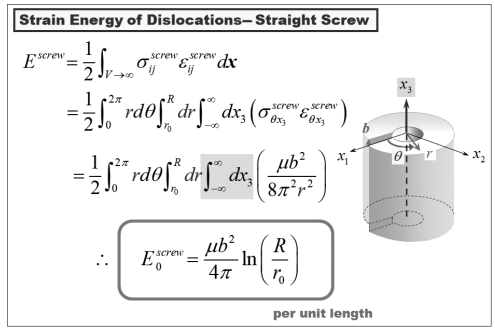

Figure 1.2.20 Strain energy evaluation for a straight screw dislocation.

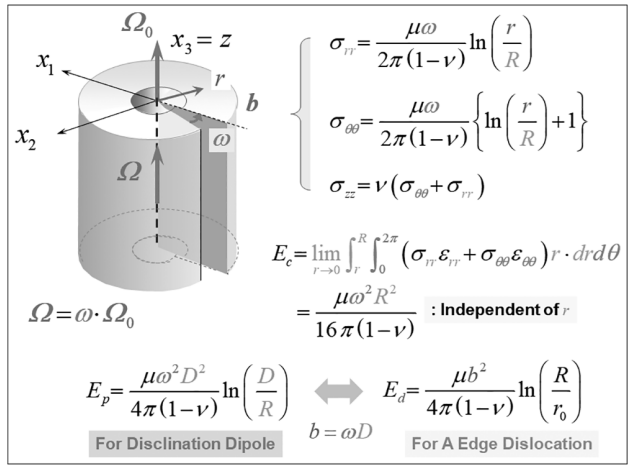

Figure 1.2.21 Strain energy for a disclination dipole, demonstrating its mathematical equivalence to that for an edge dislocation line, together with that for a single disclination line as well as its stress field.

Since $\int_{-\infty}^{\infty} dx_3$ is proportional to the length, we can find an explicit expression per unit length as

$$E_0^{\text{screw}} = \frac{\mu b^2}{4\pi}\ln\left(\frac{R}{r_0}\right), \tag{1.2.18}$$

where R and r_0 are the upper and lower bounds in the radial integral with $r_0 \sim 5b$ corresponding to the core radius. Note that since, with $R \to \infty$, E_0^{screw} logarithmically diverges, we need to set a cut-off radius, normally taken as being a mean free path of the order of 10 μm. Here the subscript "0" shows that the quantity is represented per unit length, that is, $E_0^{\text{screw}} \equiv E^{\text{screw}}/L$.

Note that the same logarithmic-type strain energy representation can be obtained for a disclination dipole, as concisely summarized in Figure 1.2.21, although a single disclination line produces the strain energy in proportion to the square of the sample

https://doi.org/10.1017/9781108874069.003 Published online by Cambridge University Press

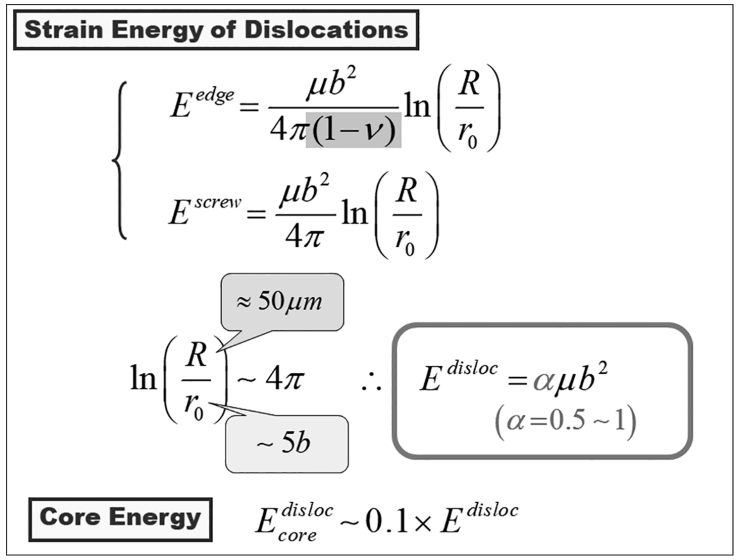

Figure 1.2.22 Rough estimation of strain energy of dislocations, together with that for core regions.

size, that is, R^2, which strongly inhibits its existence within metallic crystals in general. Here, Ω represents the Frank vector that specifies disclinations, corresponding to the Burgers vector against dislocations. More details are mentioned in Chapter 6, in the context of differential geometry.

Similarly, for a straight-edge dislocation we have

$$E_0^{\text{edge}} = \frac{\mu b^2}{4\pi(1-\nu)} \ln\left(\frac{R}{r_0}\right); \tag{1.2.19}$$

this also relates to per unit length. Since both cases yield the same form, we may roughly express them together (as in Figure 1.2.22):

$$E_0^{\text{disloc}} = \alpha\mu b^2 \left(\alpha = 0.5 \sim 1\right) \tag{1.2.20}$$

The energy of the core region can normally be regarded as about 10% of E_0^{disloc}. Hence, it can be taken into account altogether in E^{disloc} by replacing $r_0 \sim 5b$ with $1b$. It is important to remember that the energy of dislocations, whatever the types, are given in proportion to b^2.

Figure 1.2.23 provides an example of the energy of a screw dislocation for Cu. We have $E_0^{\text{screw}} = 2.5 \times 10^{-9}\,\text{J}$ per unit length, and $6.4 \times 10^{-19}\,\text{J}$ per atom. This roughly corresponds to 4 eV, which is much larger than that for a vacancy (~1 eV), meaning the dislocations are thermodynamically unstable within a crystal (Kato, 1999). Note that $1\ \text{eV} \simeq 1.602\,176 \times 10^{-19}\ \text{J}$.

For a mixed component, a simple superposition can be utilized, since there are no overlapping components of stress fields between the two, as can be confirmed by

https://doi.org/10.1017/9781108874069.003 Published online by Cambridge University Press

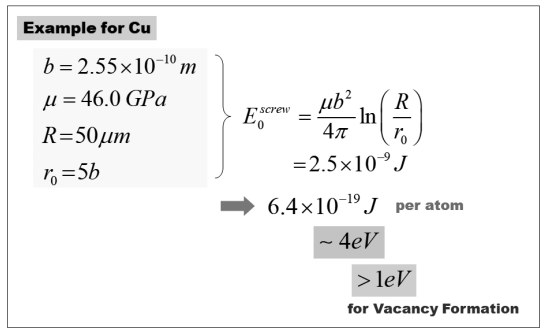

Figure 1.2.23 Example of strain energy for Cu.

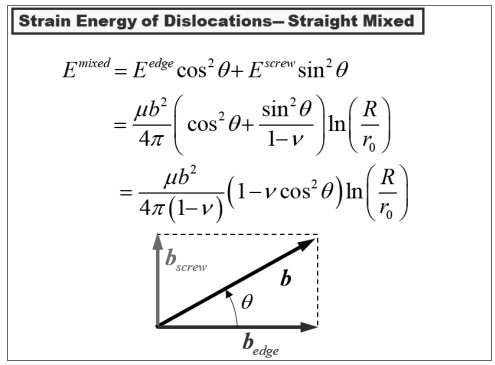

Figure 1.2.24 Strain energy for straight mixed dislocation per unit length, given as a simple superposition of those for edge and screw components, rationalized due to the nonoverlapping of stress-field components between the two.

Eqs. (1.2.2) and (1.2.3). Figure 1.2.24 shows the process to obtain the corresponding energy per unit length, that is,

$$\begin{aligned} E_0^{\text{mixed}} &= E_0^{\text{edge}}\cos^2\theta + E_0^{\text{screw}}\sin^2\theta \\ &= \frac{\mu b^2}{4\pi(1-\nu)}\left(1-\nu\cos^2\theta\right)\ln\left(\frac{R}{r_0}\right), \end{aligned} \tag{1.2.21}$$

where θ is the angle between the two components.

1.2.5 Dislocation Processes (Important Features)

This subsection presents and details several important dislocation processes. One immediate feature that must be pointed out is that the dislocations are created and annihilated. We will discuss the multiplication (i.e., creation) due to the Frank–Read mechanism, and the annihilation due to cross slip (Figure 1.2.25), which is followed by the LC junction formation. In particular, for understanding the latter two, the SFE associated with dislocation dissociation is defined and its significances are emphasized. The

https://doi.org/10.1017/9781108874069.003 Published online by Cambridge University Press

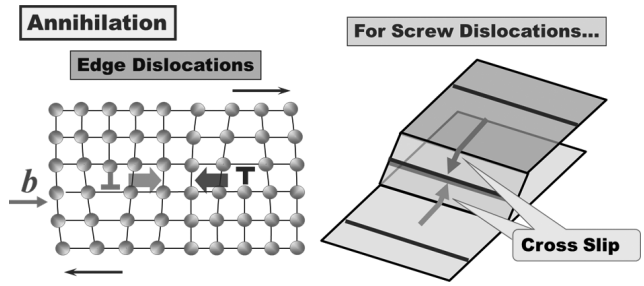

Figure 1.2.25 Schematic drawing of pair annihilation of two dislocations of opposite sign, together with a possible process yielding the reaction via two screw dislocations cross slipped onto a common slip plane sharing the same Burgers vector.

cross slip is considered to be responsible for efficiently reducing dislocation density during the course of deformation, called "dynamic recovery." This is further responsible for the dislocation cell formation, extensively discussed in Chapter 2.

1.2.5.1 Frank–Read Source and Multiplication

Schematics of the Frank–Read source (Frank and Read, 1950) and associated multiplication mechanisms are presented in Figure 1.2.26. The multiplication process from the Frank–Read source is one of the most important mechanisms, among other possibilities. Consider a pinned segment (see Figure 1.2.16(a)) with a length L that, under the force $f = \tau b$ (step 1), starts bowing out (step 2) until the critical configuration (a half-circular arc [step 3]) is reached, after which the segment becomes unstable and continues to expand spontaneously. The critical shear stress τ_{cr} corresponding to the critical configuration is given by

$$\tau_{cr} = \frac{2T}{bL} = \frac{2\alpha\mu b}{L}, \tag{1.2.22}$$

where T is the line tension of the dislocation segment evaluated as $T = \alpha\mu b^2$ with α a proportional factor. The critical stress is also called Orowan stress. If expansion continues, the curved segments tend to go around the pinning points from both sides (step 4) until they meet and react on the reverse side to leave an expanding loop (step 5). By repeating this process, dislocations can multiply. This can occur wherever similar pinned segments exist. This series of processes is schematized in Figure 1.2.26(b). Figure 1.2.26(c) provides an example of a double cross-slip event, which is considered one of the possible mechanisms for enhancing the Frank–Read multiplication process (sites for the Frank–Read source to occur).

Examples of the experimentally observed Frank–Read source, in Si (via chemical etching) (Dash, 1957) and in age-hardened Ni-Fe alloy (via transmission electron microscopy [TEM]) (Murr, 2015, 2016) are presented in Figures 1.2.27 and 1.2.28, respectively. Here, the F–R source in Si yields an anisotropic shape, reflecting its anisotropy in the slip systems, whereas, for the Ni-Fe FCC alloy, almost isotropically

https://doi.org/10.1017/9781108874069.003 Published online by Cambridge University Press

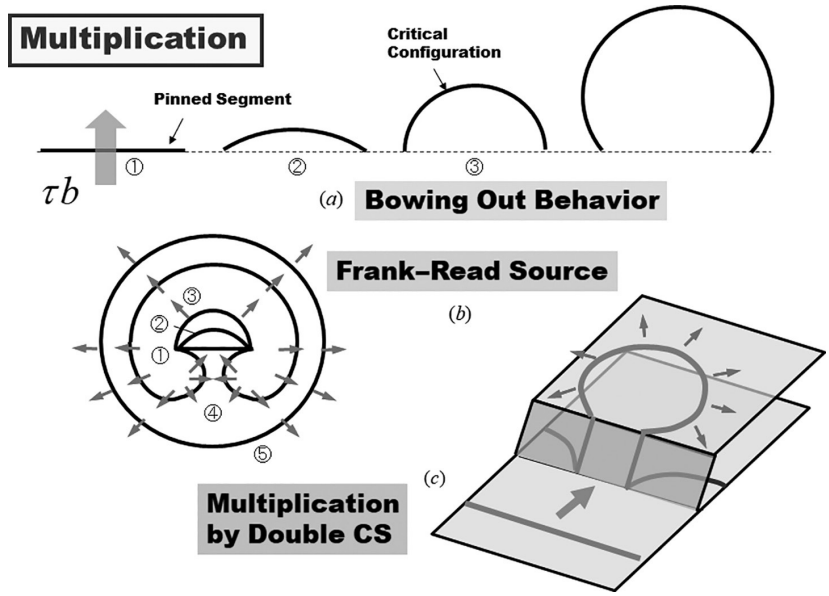

Figure 1.2.26 Multiplication mechanism via the activation of a Frank–Read source based on the bowing-out behavior of a dislocation segment (a) and (b), together with a possible process by which this can occur (c), that is, a double cross slip, which can generate a pinned segment of a screw dislocation.

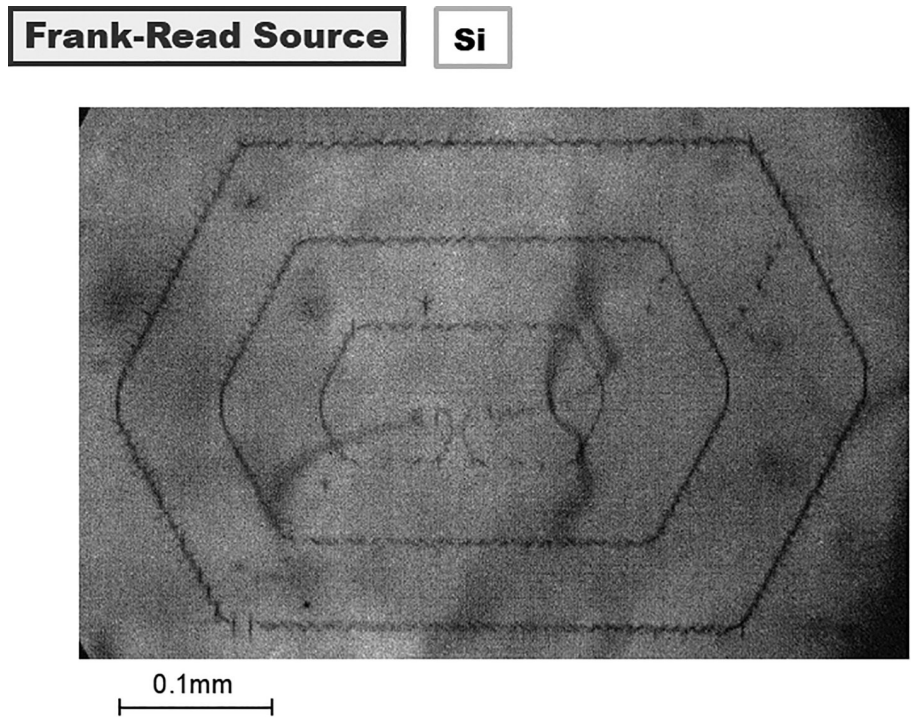

Figure 1.2.27 Example of experimentally observed Frank–Read source in silicon, showing successive generations of anisotropically expanding dislocation loops, which are delineated by chemical etching (Dash, 1957).

https://doi.org/10.1017/9781108874069.003 Published online by Cambridge University Press

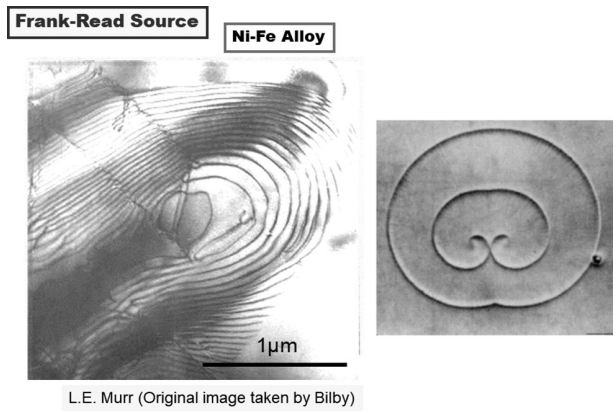

Figure 1.2.28 Example of experimentally observed Frank–Read source in age-hardened Ni-Fe alloy, yielding circular multiplication of dislocation loops (Murr, 2015, 2016).

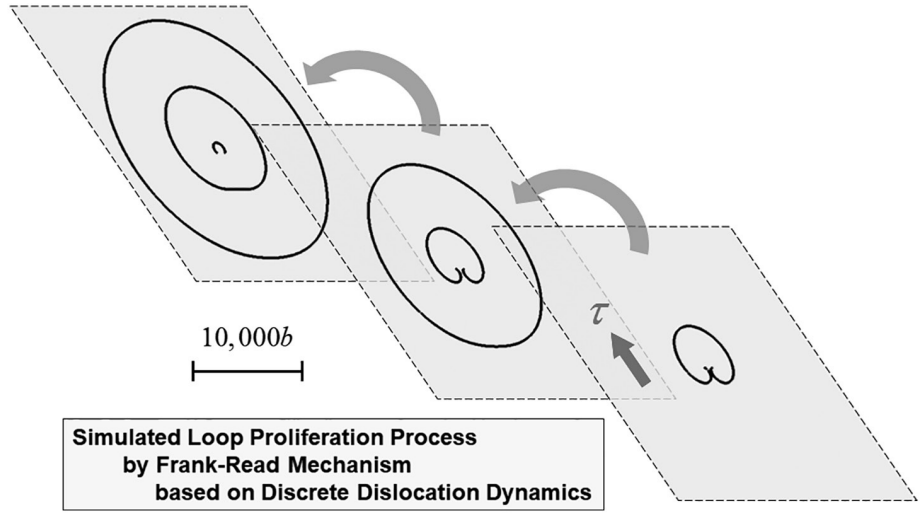

Figure 1.2.29 Example of a simulated series of snapshots for proliferating dislocation loops under shear stress on the [111] slip plane in FCC metal, based on the discrete dislocation dynamics method.

expanding dislocation loops are observed. Figure 1.2.29 displays a series of simulated snapshots of proliferating dislocation loops based on the discrete dislocation dynamics method.

A closely related important interaction of a dislocation against second-phase particles (e.g., relatively large precipitates) to the bowing-out mechanism is the Orowan process (Orowan, 1984). A schematic is given in Figure 1.2.30, where bow-out dislocation segments around spherical particles ultimately leave loops of dislocation behind. These dislocation loops can further act as obstacles against subsequent

https://doi.org/10.1017/9781108874069.003 Published online by Cambridge University Press

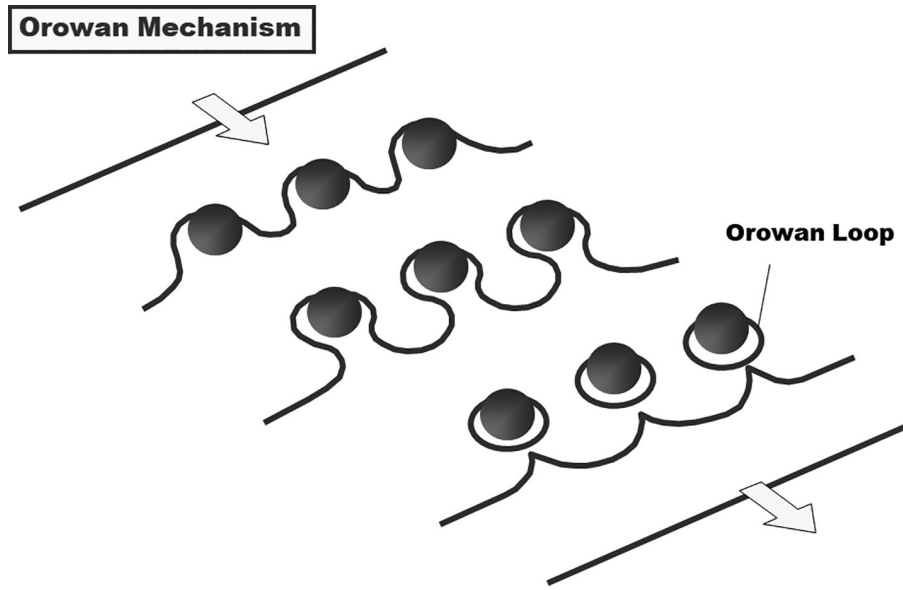

Figure 1.2.30 Schematic illustration of the Orowan mechanism, depicting the dislocation interaction, with second-phase particles leaving behind Orowan loops. When a dislocation line tries to pass through the array of particles, it bows out around them to form loops, which will act as further obstacles against subsequent dislocations.

dislocation motions that pass through, increasingly enhancing the effective diameter of the particles, thus, with decreasing interparticle spacing, this efficiently contributes to strengthening; this is regarded as one of the important strengthening mechanisms in alloyed metals and is known as the Orowan mechanism. Figure 1.2.31 shows a series of snapshots for the Orowan process, simulated by utilizing the discrete dislocation dynamics method together with a precipitate model introduced in Yamada et al. (2008), demonstrating the formation of double Orowan loops. Notice that, in the double Orowan loops, the inner loops have slightly shrunk in diameter due to the stress field of the loop-forming dislocations, and, at the same time, the second loops are elongated in the stressing direction. The former can ultimately lead to the collapse of the particles as the Orowan process continues.

More specifically, this process can take place rather exclusively against incoherent or partially coherent precipitates with relatively large interspacing (or the order of 100 nanometers). On the other hand, dislocations can cut through smaller and coherent precipitates by shearing. A comprehensive summary of this distinction is shown in Figure 1.2.32 (Sugimoto et al., 1991). Note that distinctions between the coherent and incoherent precipitates are shown in Figure 1.2.4(b) and revisited in Section 1.4.4 (Figure 1.4.16).

For further details about strengthening by alloying in general, including more sophisticated and advanced treatments as well as their experimental verifications, refer to a comprehensive monograph by Argon (2012).

https://doi.org/10.1017/9781108874069.003 Published online by Cambridge University Press

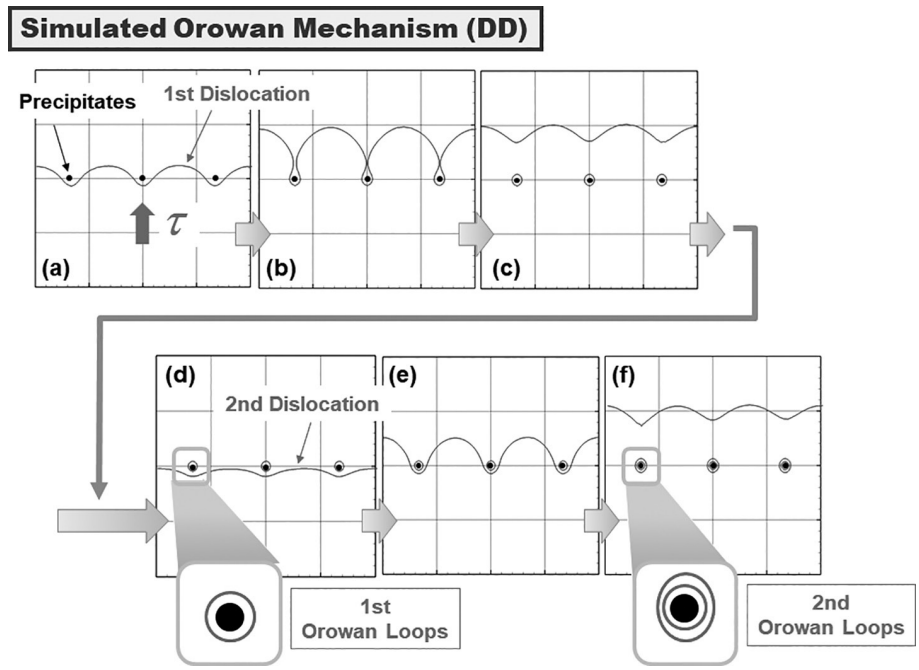

Figure 1.2.31 Simulated series of snapshots of the Orowan mechanism up to the second Orowan loop formations, based on discrete dislocation dynamics, utilizing a precipitate model proposed in Yamada et al. (2008).

	Shear	Orowan Mechanism
Dislocation-Precipitate Interactions	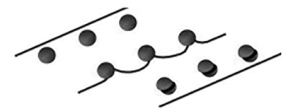	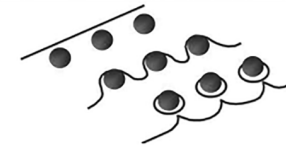
Precipitates	**Coherent GP Zone** $\bar{l}_p < \sim 10^{-7} m$	**Incoherent Partially-coherent** $\bar{l}_p > \sim 10^{-7} m$
Hardening Modulus $\left(\frac{\partial \sigma}{\partial \varepsilon}\right)$	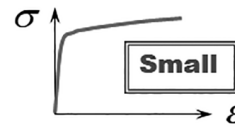	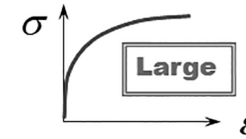
Temperature Dependency of Yield Stress $\sigma_y(T)$	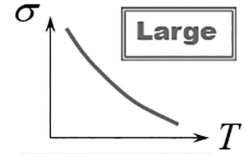 $\sigma_y(T) \propto A - T^{2/3}$	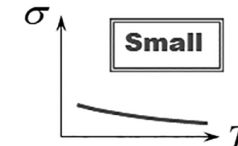 $\sigma_y(T) \propto G(T)$

Figure 1.2.32 Comparison of mechanism for dislocation-precipitate interactions (Sugimoto et al., 1991). Adapted with permission of the publisher (Asakura Publishing Co.).

https://doi.org/10.1017/9781108874069.003 Published online by Cambridge University Press

1.2.5.2 Partial Dislocations and Stacking Fault

SFE is one of the most important notions in understanding the diversity of mechanical behaviors of metals, especially those with an FCC structure, because it substantially controls the dislocation motions in terms of their interactions, such as junction formations and associated strain hardening, cross slip and resultant dynamic recovery, and further, attendant substructure evolutions. Also a sharp distinction can be found between FCC and BCC metals in the light of SFE.

A dislocation can be split into two partial dislocations. Figure 1.2.33 shows an example for FCC metals, where the reaction is expressed as

$$\frac{a}{2}[\bar{1}01] \rightarrow \frac{a}{6}[\bar{1}\,\bar{1}2] + \frac{a}{6}[\bar{2}11], \tag{1.2.23}$$

where a is the lattice constant. This cases shows Shockley's partial dislocations. This dissociation is energetically favorable when the SFE is absent, that is, $|\boldsymbol{b}|^2 > |\boldsymbol{b}_1|^2 + |\boldsymbol{b}_2|^2$, as confirmed by simple arithmetic. We must not, however, ignore the SFE to be added to the right-hand side of the inequality, as shown in Figure 1.2.34. This ultimately decides whether the dissociation takes place or not. The SFE is the interfacial energy for the imperfect stacking sequence of atomic layers situated between the extended dislocations (termed leading and trailing partials, respectively). The table in Figure 1.2.33 lists the values of SFE for typical metals. Roughly speaking, FCC

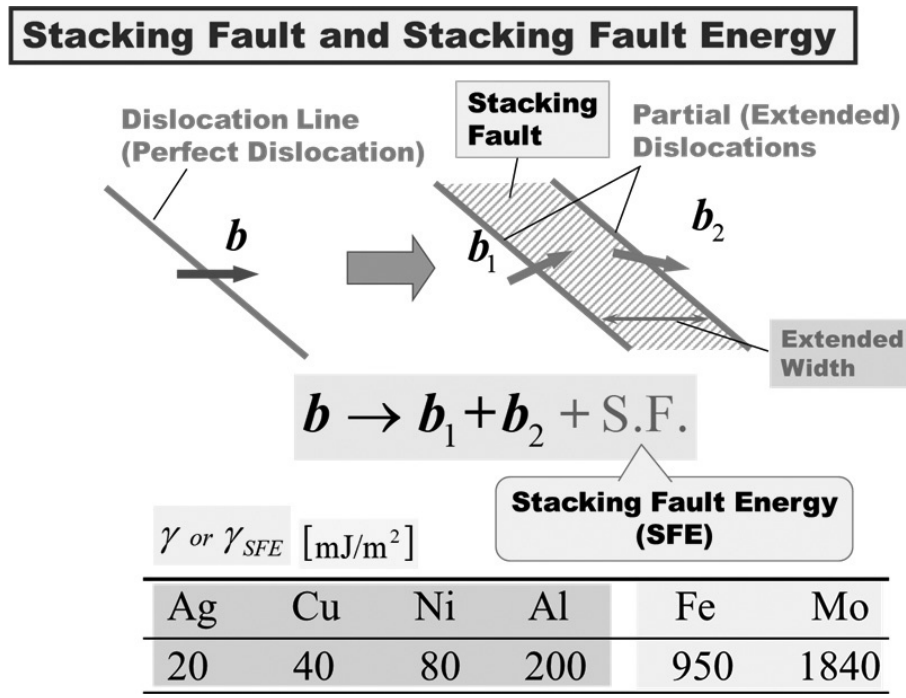

Figure 1.2.33 Dissociated dislocations (called partial dislocations) with a stacking fault located between them, which demands additional energy for creating a planer defect due to the imperfection of a stacking sequence of atomic layers called SFE. The table lists examples of SFE for typical metals.

https://doi.org/10.1017/9781108874069.003 Published online by Cambridge University Press

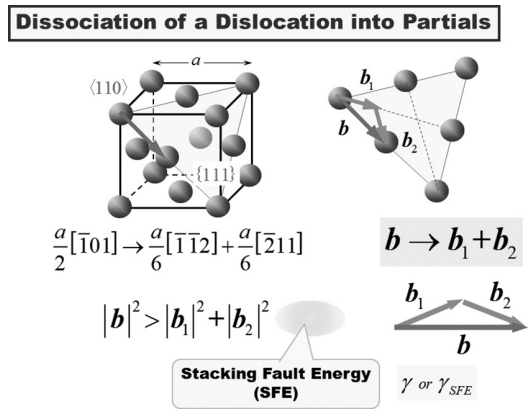

Figure 1.2.34 Schematic drawing of dissociation of perfect dislocation into a pair of Shockley partial dislocations for FCC metals, which is energetically favorable in the absence of stacking fault.

metals have relatively small SFE, while BCC metals yield extremely large values. Aluminum is known to have the largest values, of about 100–200 mJ m^{-2}, among FCC metals, while Cu is recognized as having relatively small SFE, that is, 40 mJ m^{-2}: They are frequently referred to as typical FCC metals with large and small SFE in the literature. The smallest SFE for FCC metals goes to Cu-Si alloys (e.g., Cu-8.8at% Si) with 3–5 mJ m^{-2} or less (e.g., Murr, 1975), followed by aluminum-bronze (Cu-about 10% Al alloys) and α-brass (Cu-less than 35% Zn alloys) with less than 10 mJ m^{-2}, and austenitic stainless steels (e.g., 18–8 or type 304) with around 10–13 mJ m^{-2}.

It is commonly recognized that BCC metals basically do not have a stacking fault because it is not energetically favorable. The values of the SFE are extremely large in comparison even with that for Al. This means that dislocations in BCC metals substantially do not (or never) extend.

Figures 1.2.35 and 1.2.36 show a stacking fault viewed from the top, each indicating shifts in the stacking sequence of atoms above and below, and raised electron density distribution in the SF (Suzuki, 1967), respectively. The inset in Figure 1.2.35 is a table listing the extended widths w for Cu and Al, comparing the values for edge and screw components (Karashima, 1972). Screw component tend to have larger SFE than the edge for both the metals, since the SFE is inversely proportional to the extended width, that is,

$$w = \frac{\mu a^2}{16\pi\gamma_{\mathrm{SFE}}}\left\{\frac{2-3\nu}{3(1-\nu)}\right\}, \tag{1.2.24}$$

where γ_{SFE} stands for the SFE of the material concerned.

1.2.5.3 SFE and Cross Slip

The SFE is closely related to the cross-slip process by the screw dislocations (component). Figure 1.2.37 shows a schematic of the cross-slip process for an extended screw

https://doi.org/10.1017/9781108874069.003 Published online by Cambridge University Press

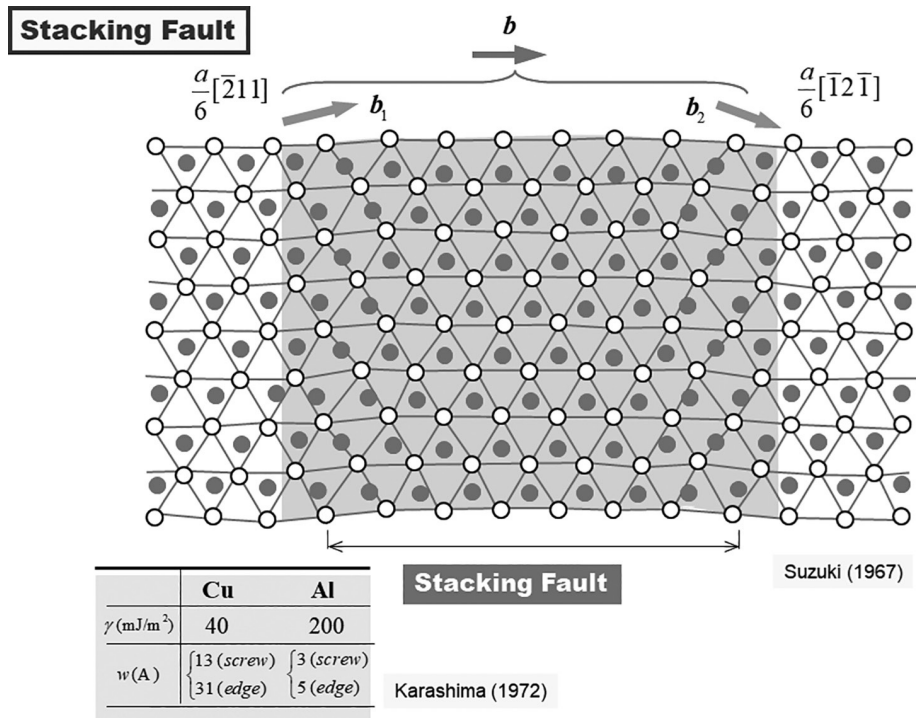

Figure 1.2.35 Schematic drawing of stacking fault illustrated as an imperfect stacking sequence of atomic layers (Suzuki, 1984). Adapted with permission of the publisher.

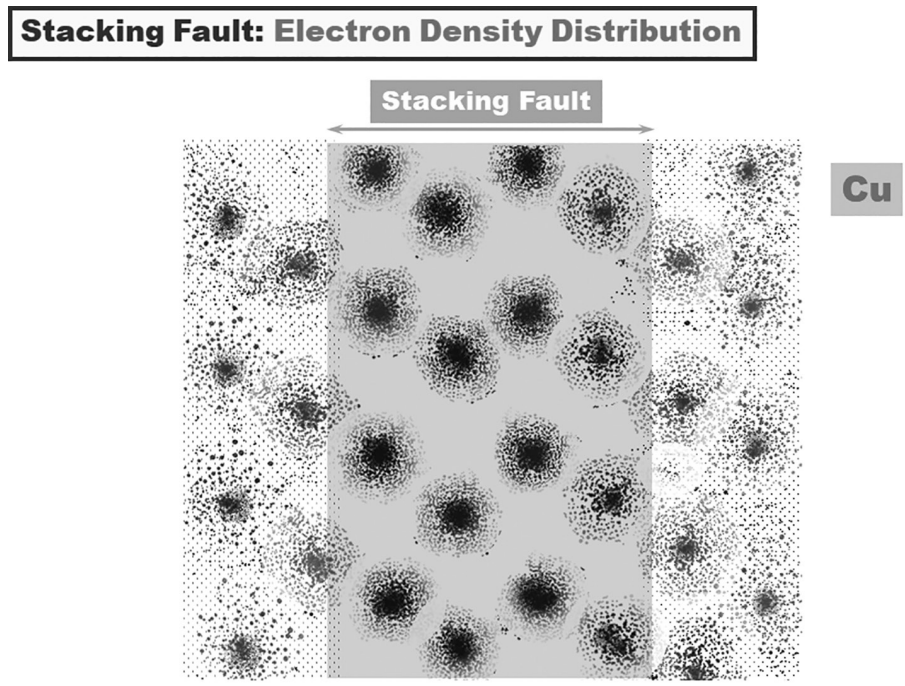

Figure 1.2.36 Representation of a stacking fault as a region with high electron density in Cu (Suzuki, 1967). Adapted with permission of the publisher (Agne Publishing Co.).

https://doi.org/10.1017/9781108874069.003 Published online by Cambridge University Press

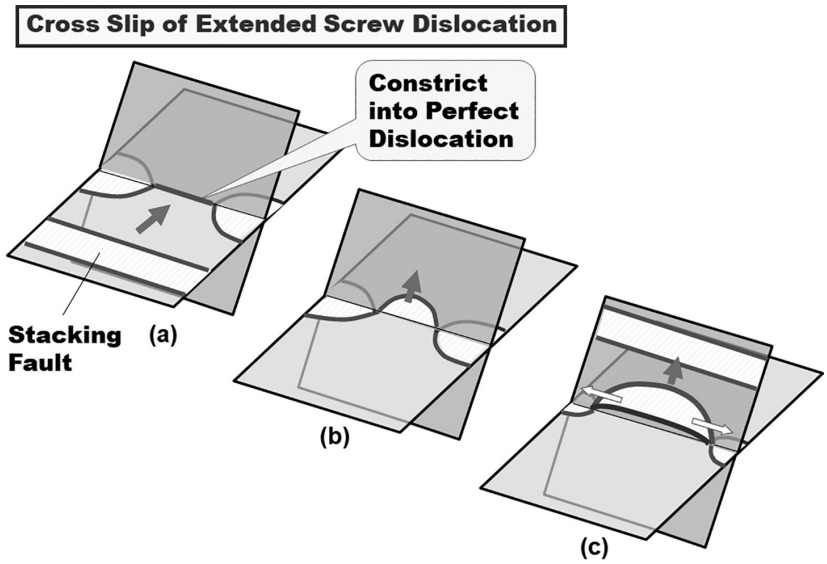

Figure 1.2.37 Schematic drawing of the cross-slip process. Dissociated dislocation must be constricted once in order to realize the cross slip onto another plane, after which double kinking can promote the further motion of the cross-slipped segment.

dislocation. When a cross slip occurs from one slip plane to another (referred to as the cross-slip plane), the extended partial dislocations, each having the Burgers vectors slightly deviating from the line direction, must constrict once in order to change the glide plane, because the Burgers vectors must be parallel to the dislocation line to share the slip planes. Energetically, this cannot take place all at once but can occur partially (Figure 1.2.37(a)), and the constricted part will proceed to the cross-slip plane (Figure 1.2.37(b)). Once this happens, the kinking mechanism can help advance the cross-slipped segment further along the cross-slip plane where the pair of kinks of the cross-slipped segment spread laterally, as depicted by open arrows (Figure 1.2.37(c)). Figure 1.2.38 displays an example of simulated results by discrete dislocation dynamics, providing a series of snapshots for a cross-slip process. This process is assisted by the resolved shear stresses (RSSes) both on the primary and cross-slip planes and particularly the help of thermal vibrations, which will be detailed in Chapter 2 in the context of the thermal activation mechanism.

Since this mechanism requires shrinkage of the extended dislocations into a perfect one, the frequency is substantially controlled by the SFE. As is shown in the table in Figure 1.2.39, the ease or difficulty of the cross slip is measured by the SFE. Metals with smaller SFE yield lower cross-slip frequency, whereas those with higher SFE exhibit higher frequency. Among FCC metals, Al yields the largest frequency of the cross-slip events, while Ag and Cu show greatly restricted cross slip due to their relatively small values of SFE. BCC metals, on the other hand, coupled with relatively larger number of slip systems than FCC metals, have a propensity to yield extremely frequent cross slips during plastic deformation.

https://doi.org/10.1017/9781108874069.003 Published online by Cambridge University Press

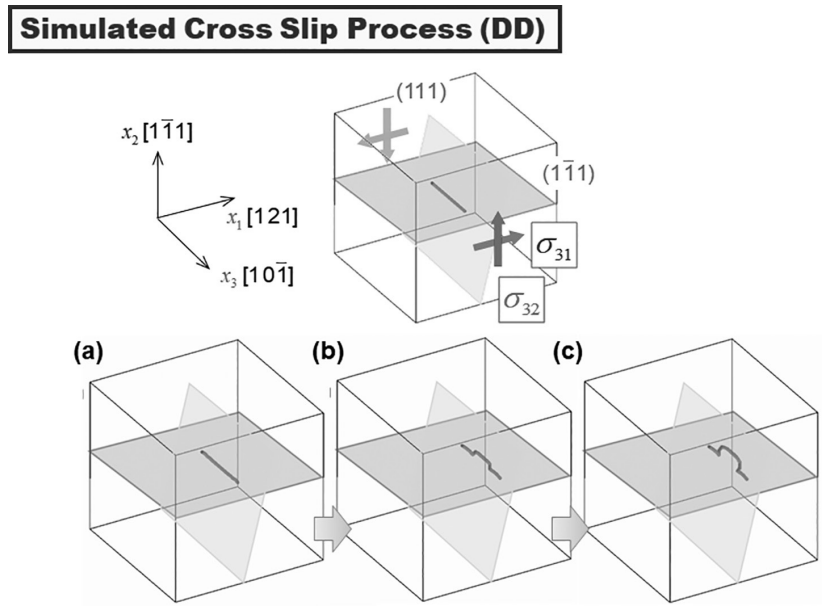

Figure 1.2.38 Simulated cross-slip process by discrete dislocation dynamics.

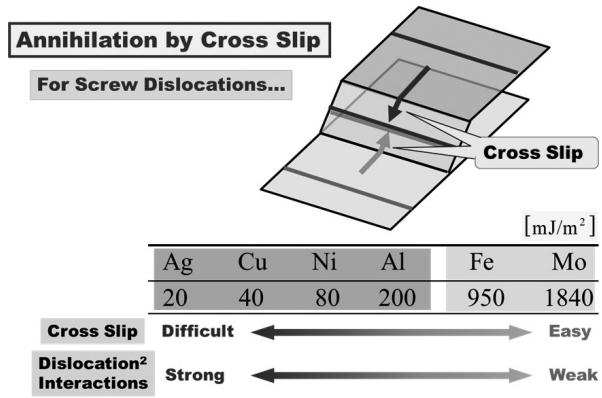

Figure 1.2.39 Relationships between the SFE and dislocation processes, that is, cross-slip and dislocation–dislocation interaction strength. Small SFE yields less frequency of cross slip and large interaction strength, whereas large SEF results in higher frequency of cross-slip phenomena and weaker interaction strength. The table lists typical values of SEF for representative metals including not only FCC but also BCC.

Figure 1.2.40 shows an atomistic simulation result for cross slip from the primary plane (first line) to the cross-slip plane (second line), demonstrating that it takes place quite spontaneously given the initial and final states (Rasmussen et al., 1997). The bottom image in the figure displays an experimentally observed image of the cross-slip process (Robertson and Fivel, 1999).

https://doi.org/10.1017/9781108874069.003 Published online by Cambridge University Press

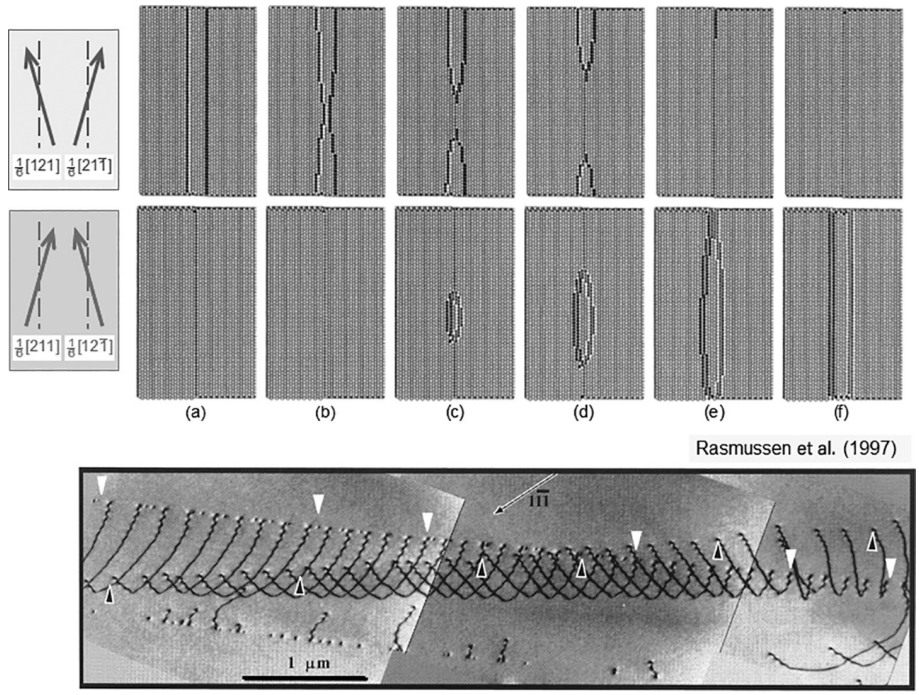

Figure 1.2.40 Live images of cross-slip processes obtained in atomistic simulation (top) (Rasmussen et al., 1997). and that observed experimentally via TEM (bottom) (Phillips, 2001). Adapted with permission of the publishers (APS Publishing Co. for the simulation results, while Cambridge Univ. Press for the TEM micrograph).

One of the manifestations of such trends is the slip-line geometries that emerge on the sample surfaces, as schematically shown in Figure 1.2.41(a)–(c) (Takamura, 1999), where comparison is made among α-brass, Al, and α-Fe. They show sharp contrast: α-brass exhibits straight slip lines due to highly restricted cross slip, while Al shows occasional direction changes in the slip lines as the sign of cross slips. Further, α-Fe exhibits wavy slip lines due to restlessly occurring cross slips together with indefinite slip planes. Figure 1.2.41(d) illustrates such equivocally wandering slip behavior, called "pencil glide" because the slip trace looks like a hexagonal cylinder wall of a pencil.

1.2.5.4 Dislocation–Dislocation Interactions

Dislocation interactions are important ingredients in understanding the hardening phenomena in terms of the metals' responses. Even in 100% pure metals, many complications exist because of the complexities associated with the variation of the interactions and the resultant reaction products. This chapter does not intend to address the state-of-the-art of dislocation interactions, which have seen large advances in their reporting recently, coupled with massive and direct atomistic or dislocation dynamics' simulations (e.g., Bulatov et al., 2006), but rather to concentrate on fundamental but often overlooked issues of importance.

https://doi.org/10.1017/9781108874069.003 Published online by Cambridge University Press

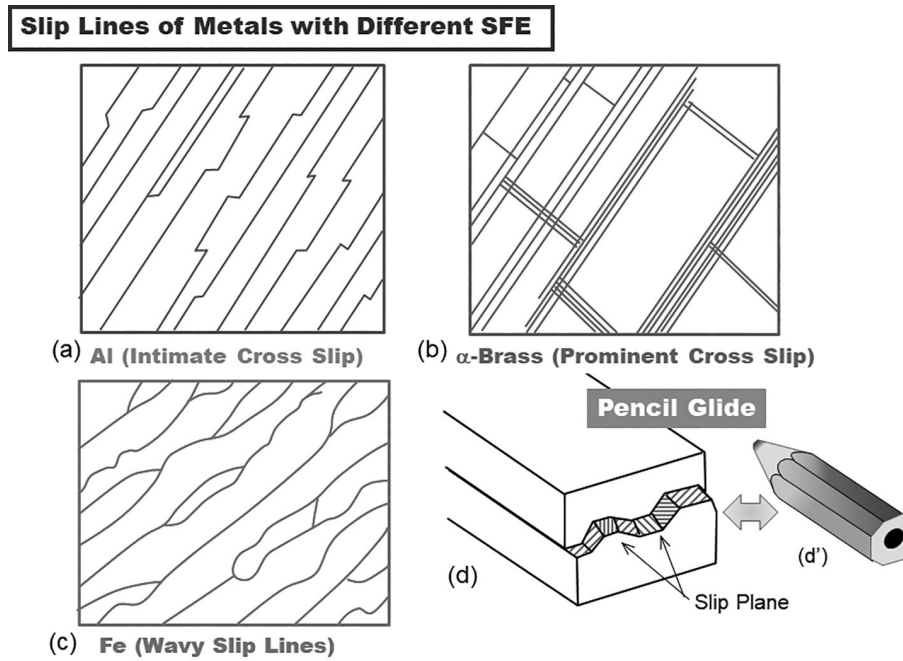

Figure 1.2.41 Schematic illustration of slip lines typically observed on aluminum, alpha-brass, and iron sample surfaces, together with pencil glide for iron (Takamura, 1999). Adapted with permission of the publisher (Kyoto University Press).

One may gain the impression that even a single interaction process of dislocations involves many details. Although the elucidation of such details is certainly relatively important, what is paramount is why such microscopic details do not have much effect on the macroscopic response, showing, in a sense, a sort of "universality," rather than "specificity." A candidate mechanism for this "specificity–universality" transition problem will be given in Chapter 5.

1.2.5.5 LC Sessile Junction

For understanding hardening mechanisms, junction formations are the most important reaction between dislocations. The LC reaction and the resultant LC junction (or lock) formation are of particular importance for FCC metals, among others, simply because it is the strongest, that is, it is a sessile lock yielding maximum strength. Since the reaction takes place between two leading partial dislocations belonging to different planes, as depicted in Figure 1.2.42, the SFE also plays a decisive role in terms of both the frequency and the strength. As indicated in the figure, the smaller the SFE is, the higher the strength, but with lower frequency.

This reaction is expressed as

$$\frac{a}{6}\left[\bar{1}2\bar{1}\right]+\frac{a}{6}\left[21\bar{1}\right]\rightarrow\frac{a}{6}\left[1\bar{1}0\right]. \tag{1.2.25}$$

https://doi.org/10.1017/9781108874069.003 Published online by Cambridge University Press

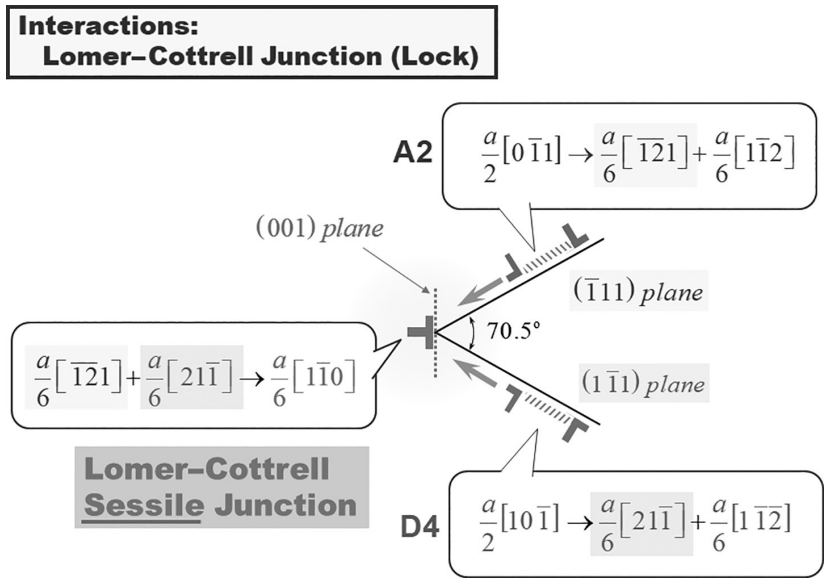

Figure 1.2.42 Formation mechanism of an LC junction as a result of the reaction between two leading partial dislocations. Since the reaction product has a resultant Burgers vector with the "third" direction, it becomes sessile.

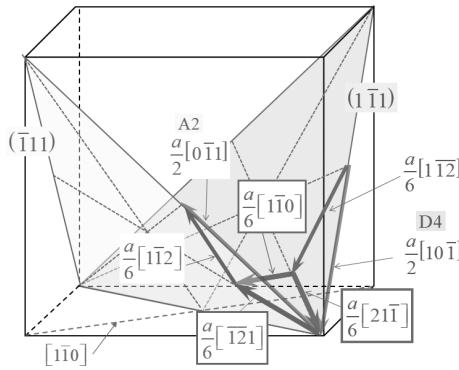

Figure 1.2.43 Geometrically tractable representation of the formation of an LC junction.

As a result of the reaction, a junction segment having a different Burgers vector $a/6[1\bar{1}0]$ from the parent dislocations is produced, which makes the lock sessile (Figure 1.2.43). Figures 1.2.44 and 1.2.45 provide two more schematics representing the LC junction. An intersection of dislocations on the primary and the conjugate systems is illustrated in the figures.

Figure 1.2.46 presents simulation results for the LC junction formations produced by Shenoy et al. (2000) based both on molecular dynamics (atomistic; not shown here) and dislocation dynamics (linear elasticity), comparing the configurations between Al and Ag. In Al, the slightly extended dislocations due to high SFE react to form an LC

https://doi.org/10.1017/9781108874069.003 Published online by Cambridge University Press

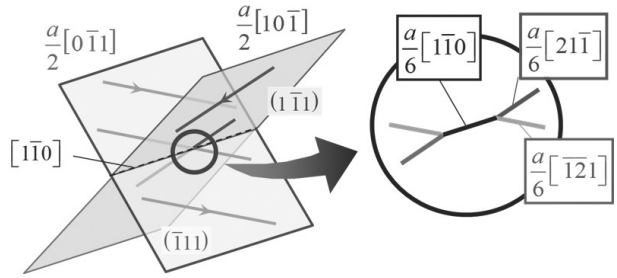

Figure 1.2.44 Schematics of the LC junction formed between two intersecting dislocations on the primary and conjugate slip systems, where the close-up view indicates the reaction product having the "third" Burgers vector $a/6[.1\bar{1}0]$

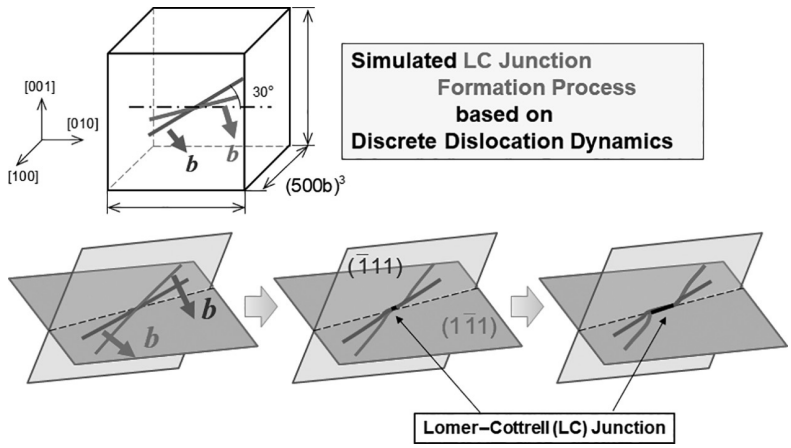

Figure 1.2.45 Simulated LC junction formation process by discrete dislocation dynamics.

sessile junction along the intersection line of the two slip planes, while Ag exhibits a similar LC junction but with largely extended dislocations because of low SFE. The excellent agreement between the atomistics and continuum elasticity implies that the configuration is determined so as to lower the strain energy, excluding the core region where the linear elasticity is considered to become inaccurate. This implies that the configuration of the LC junction is basically dominated by the linear elasticity.

Figure 1.2.47 shows a TEM micrograph of an LC junction observed in stage II for Cu-15at%Al (Karnthaler and Winter, 1975). The configuration of the simulated result for Al in Figure 1.2.46 agrees well with the experimentally observed one for Cu alloy, even for the stair-rod shape at the edge of the junction.

To summarize this discussion, we now understand many of the mechanical properties of FCC metals, which can be relatively easily captured if we focus on the "SFE," as overviewed in Figure 1.2.48. Here, Cu and Al are taken as representatives of low and high SFE, respectively (Figure 1.2.48(d)), as they normally exhibit mutually contrasting mechanical properties, manifested as the hardening characteristics appearing

https://doi.org/10.1017/9781108874069.003 Published online by Cambridge University Press

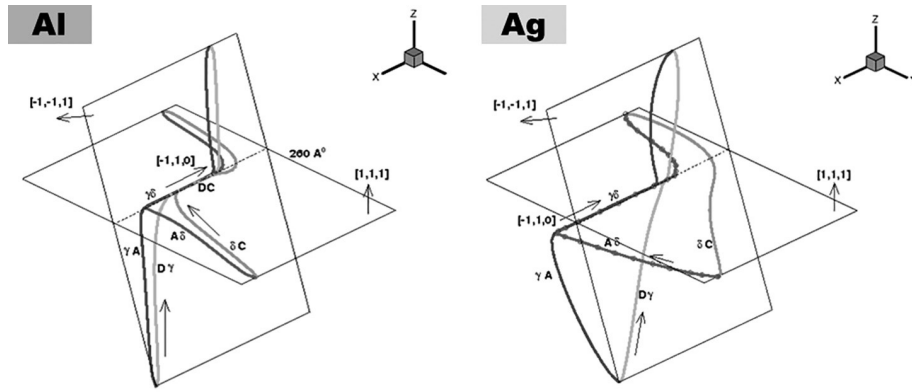

Ag	Cu	Ni	Al
20	40	80	200

$[mJ/m^2]$

Figure 1.2.46 Simulated LC junctions based on linear elasticity-based dislocation dynamics for two typical FCC metals with high and low SFE, that is, Al and Ag. The configurations are demonstrated to agree nicely with those via atomistic simulations (Shenoy et al., 2000, p. 1491). Adapted with permission of the publisher (APS Publishing Co.).

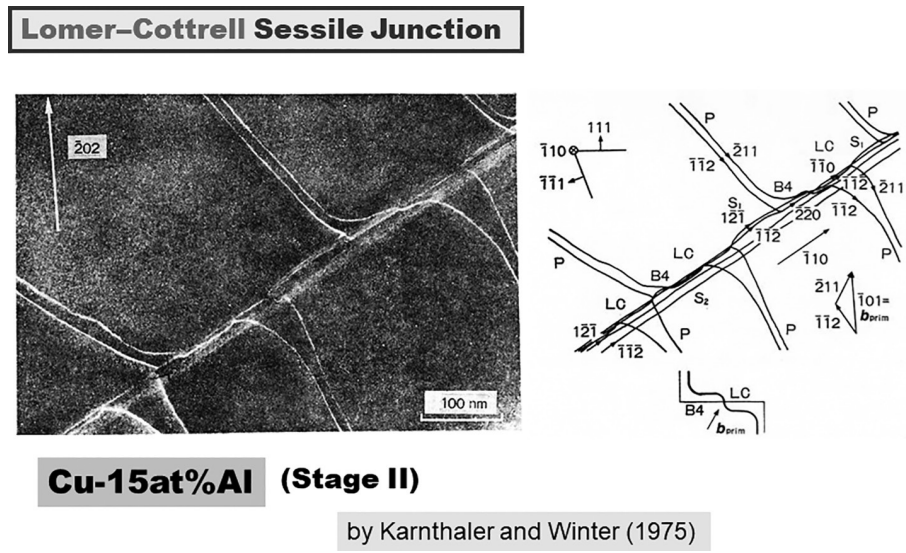

Figure 1.2.47 Experimentally observed LC junction for Cu-15at%Al during stage II hardening (Karnthaler and Winter, 1975). Adapted with permission of the publisher (Elsevier Science & Technology Journals).

https://doi.org/10.1017/9781108874069.003 Published online by Cambridge University Press

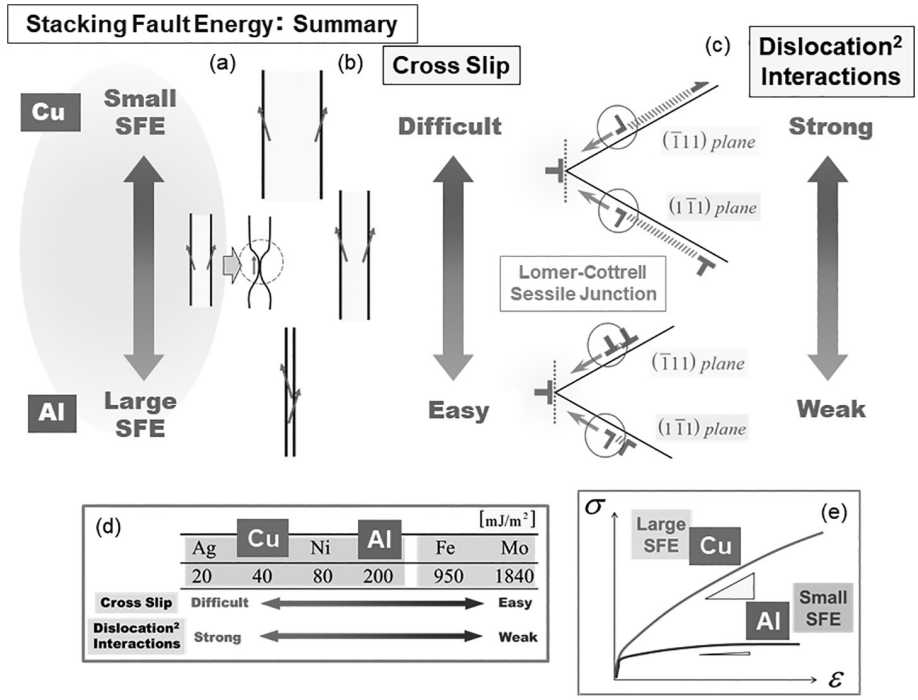

Figure 1.2.48 Overview of the dislocation-based unified perspective for macroscopic mechanical properties in FCC metals as a summary from the viewpoint of SFE.

in the stress–strain responses, yet both, nevertheless, belong to the same FCC family. A schematic comparison of their stress–strain relations under monotonic tension is presented in Figure 1.2.48(e), emphasizing the difference in the hardening moduli. With large enough SFE, as in Al, one may safely ignore the extension of dislocations into partials (Figure 1.2.48(a)), resulting in frequent cross slip and subsequent pair annihilations (dynamic recovery) (Figure 1.2.48(b)), while easily dissociable LC junctions scarcely contribute to strain hardening (Figure 1.2.48(c)). The reverse is true for Cu with small enough SFE, that is, less frequent cross slip tends to hinder dynamic recovery on one hand, while fully extended dislocations are apt to form strong LC sessile locks that ultimately enhance strain hardening on the other.

Some practical examples of such SFE-based views are presented in both Appendix A2 and Chapter 3 (Figure 3.3.13), which may provide strong leverage for justifying the above views. In the former, a systematic series of experiments on the coupling effects between the nonproportional (NP) strain history and the strain rate, including the impact loading regime, are extensively discussed, while, in the latter, a systematic set of variations observed in the evolved dislocation cell structures strongly depending on the SFE are discussed based on experimental results under NP cyclic straining.

It should be noted that understanding BCC metals is not that simple, unlike the FCC case described previously, but a good start for tackling the issue is provided in the "FCC versus BCC" perspective.

https://doi.org/10.1017/9781108874069.003 Published online by Cambridge University Press

1.2.5.6 Jog Formation

Let us mention "jog," which may become important, particularly in understanding hardening in BCC metals, as summarized in Figure 1.2.49. Jog is a product of the orthogonal intersecting of two dislocation lines (one of the forest intersection), characterized as a step formed on a dislocation line in the out-of-slip plane (those formed on the same slip plane are called "kinks" [see Figure 2.2.7]). There are four kinds of such orthogonal intersection depending on the combinations of edge and screw components, that is, "edge against edge or screw" and "screw against edge or screw."

The intersection expected to be exceptionally important in BCC metals (in terms of hardening) is that formed between two screws (i.e., on a screw dislocation against a screw segment), as schematically shown in Figure 1.2.50. The intersecting screw dislocation line leaves "jog" on it. Since the "jog" portion of the dislocation segment

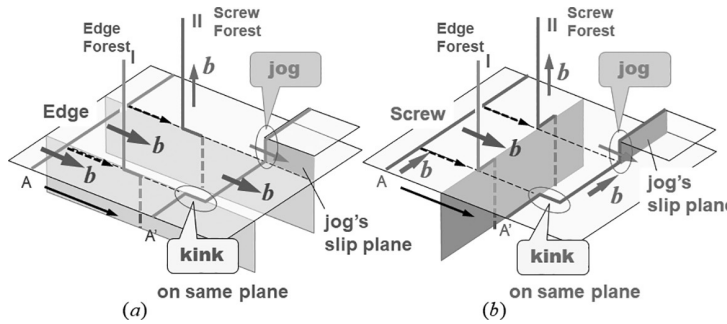

Figure 1.2.49 Formations of jog and kink as a result of intersecting edge dislocation (a) and screw dislocation (b) against edge and screw forests, respectively.

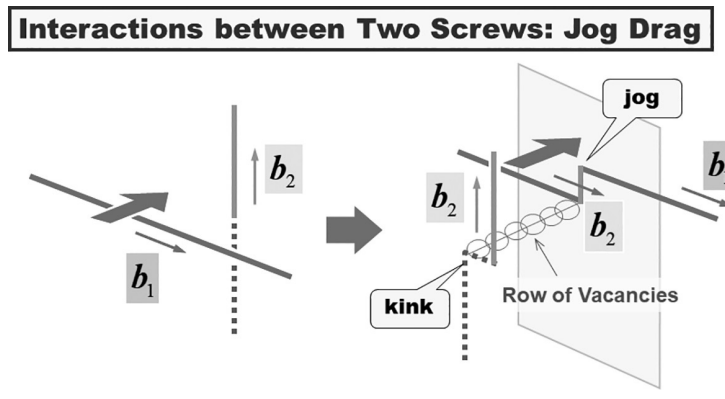

Figure 1.2.50 The jog-drag mechanism as a result of the intersection of two mutually perpendicular screw dislocations. One of the dislocations yields a "jog" with the nature of an edge component, which cannot continue to glide except a climb motion, where vacancies are provided from the surroundings, which induces resistance against the dislocation motion.

https://doi.org/10.1017/9781108874069.003 Published online by Cambridge University Press

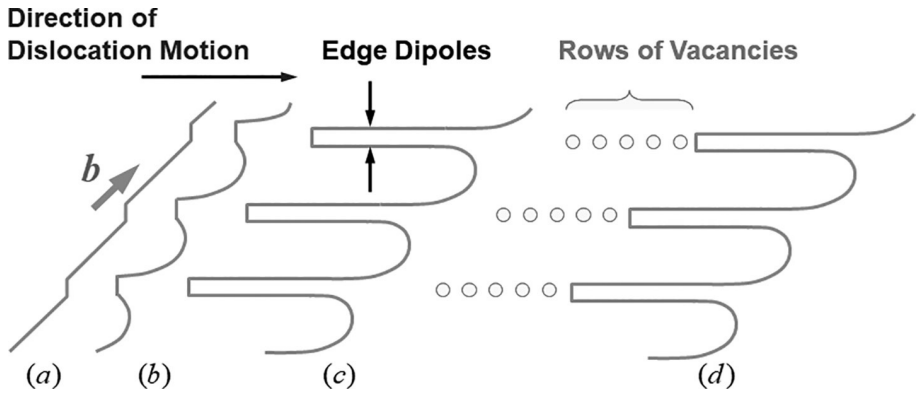

Figure 1.2.51 Schematics of "jog drag" showing the sequence of motion of a jogged screw dislocation line (a), followed by (b) bowing out, (c) formation of edge dipoles, and (d) resultant jog dragging leaving vacancy rows behind.

is perpendicular to the Burgers vector b_l (which is conserved), it acts as an "edge" component that cannot be slipped along the same slip plane any further. For it to glide further, vacancies must be brought from somewhere to replace the "excessive" atoms (this process is thus "nonconservative," in contrast to other dislocation motions, and is called a "climb" motion). Therefore, the glide motion of a screw jog must leave an array of vacancies along the trace, as depicted on the right-hand side of Figure 1.2.50 (this is called "jog drag"). The "jog-dragging" process will also produce an edge dipole, as illustrated in Figure 1.2.51, since dislocations tend to bow out due to the line tension, while the jog is highly resistant compared with the other portions of the screw dislocation line. Note that the reverse motion of the screw jog produces an array of "interstitial" atoms instead of vacancies.

Examples of discrete dislocation-based simulation results for the "jog-related" processes, including "jog drag," are displayed in Figure 1.2.52, that is, (a) formation of a jog dipole, (b) the jog-dragging process, and (c) bypassing after jog dipole formation. Continuous stressing against (a) results in (c), further acting as a Frank–Read source that leads to multiplication. These overall observations remind us of a versatile aspect of the "jog-related" processes critical to many aspects of plasticity.

Note that the process just described is of further importance when we look into a fatigue-crack initiation mechanism from persistent shear band (PSB) ladder structures (under high-cycle fatigue, see Section 3.7.1), because the "jog-dragging" accompanying-edge dipoles produced within the interladder wall regions can produce a number of vacancies, as will be briefly discussed in Appendix A9.

1.2.5.7 About Dislocation Density

Let us consider afresh an intuitive image of "dislocation density" for metals, by focusing on two typical extreme cases (Kato, 1999), as displayed in Figure 1.2.53: For well-annealed pure metals, we normally have $\rho \sim 10^9 - 10^{10}\,\mathrm{m}^{-2}$, whereas for deformed states the values reach $10^{14} - 10^{15}\,\mathrm{m}^{-2}$.

https://doi.org/10.1017/9781108874069.003 Published online by Cambridge University Press

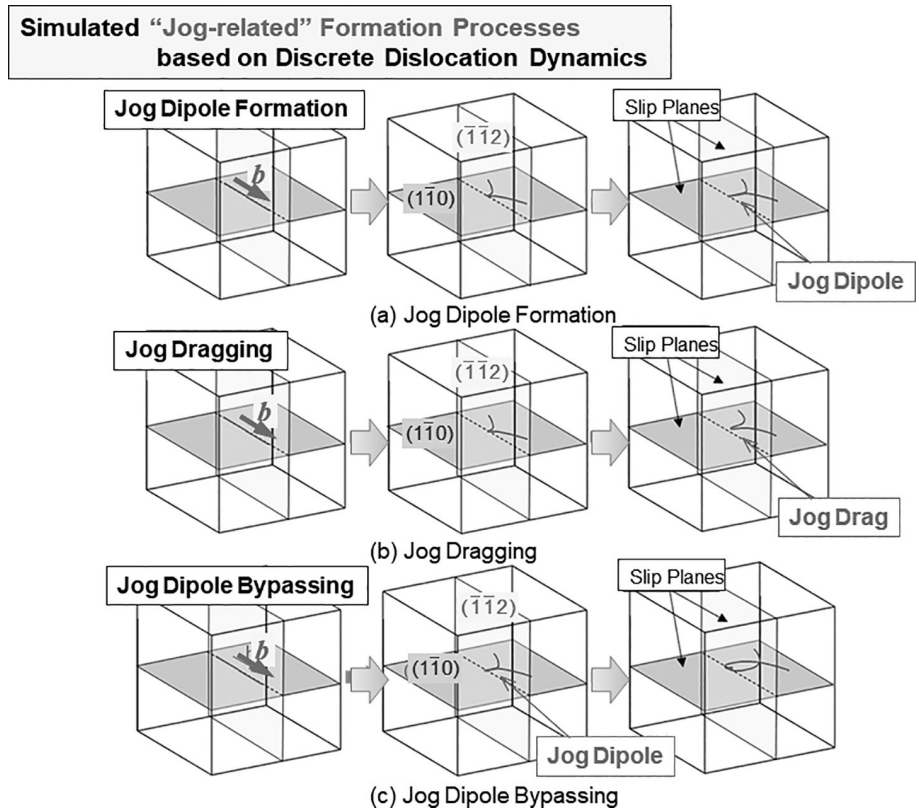

Figure 1.2.52 Simulated "jog-related" processes by discrete dislocation dynamics: (a) jog dipole formation, (b) jog-dragging process, and (c) bypassing a formed jog dipole.

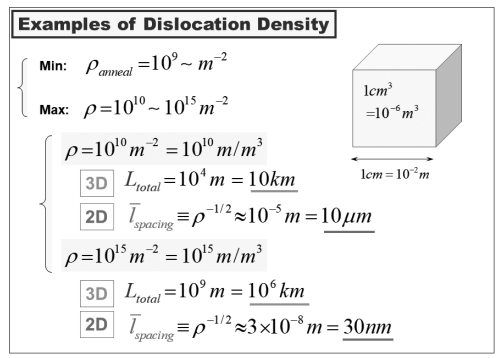

Figure 1.2.53 Examples of typical dislocation density for fully annealed and work-hardened samples, together with the commensurate total length of the dislocation line assumed to be contained in a unit cube. See also Figure 1.4.2.

https://doi.org/10.1017/9781108874069.003 Published online by Cambridge University Press

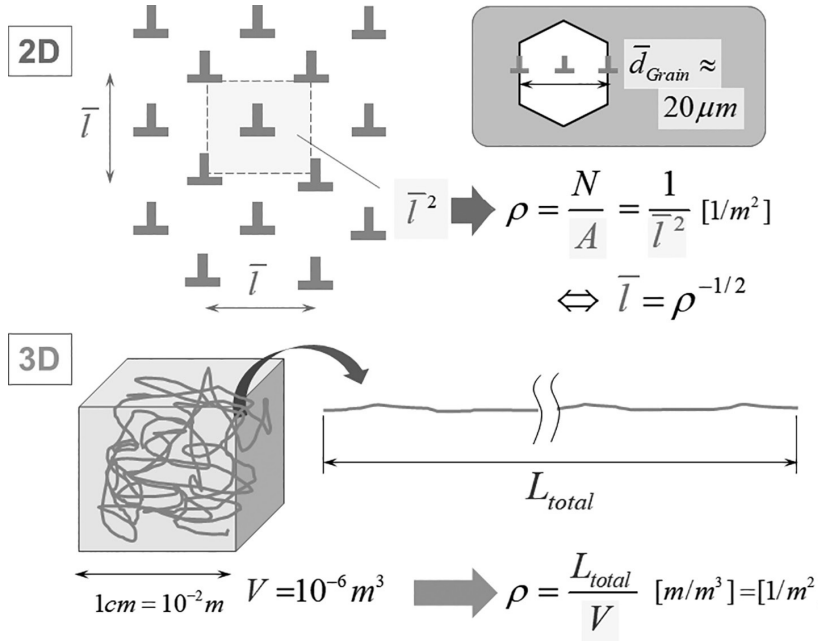

Figure 1.2.54 Intuitive images of 2D and 3D dislocation density, that is, mean spacing for 2D and total length per unit volume for 3D definitions, based on which we evaluate typical values of the smallest and largest dislocation density, as listed in Figure 1.2.53.

For an intuitive image of "dislocation density," let us use two quantities – "mean spacing" and "total length" per unit volume (m^3). The former is directly related to the two-dimensional (2D) definition of ρ, while the latter to the 3D definition. Figure 1.2.54 schematically illustrates how we define "dislocation density" in the context of 2D and 3D images, respectively.

As can be readily understood from the schematics illustrated in Figure 1.2.54, the mean spacing of dislocations can be roughly estimated from the density via $\rho^{-1/2}$, assuming uniform distribution. The dislocation density of $10^{10}\,m^{-2}$ corresponds to $\bar{l}_{spacing} \approx 10\,\mu m$ (Figure 1.2.53). This is of the order of the grain size in conventional polycrystalline metals, meaning few dislocations included within a crystal grain. In sharp contrast, the density of $10^{15}\,m^{-2}$ is commensurate with $\bar{l}_{spacing} \approx 30$ nm, roughly corresponding to 100 atoms. From this fact one can discover the maximum density that crystals can contain to be around $10^{16}\,m^{-2}$.

For the total length, the former yields $L_{total} = 10$ km, while the latter $L_{total} = 10^6$ km (Figure 1.2.53). This is equivalent to several times the distance to the moon from the Earth (which is about 3.8×10^4 km).

A typical example of the highest dislocation density is that in martensite or bainite structures. Figure 1.2.55 shows a TEM picture of lath martensite observed in Fe-0.6%C (Maki et al., 1979), where the black contrasted regions depict high-density

https://doi.org/10.1017/9781108874069.003 Published online by Cambridge University Press

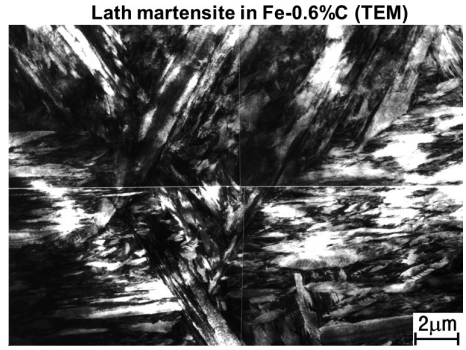

Figure 1.2.55 TEM micrograph of a martensite lath structure as an example of one of the highest dislocation densities.

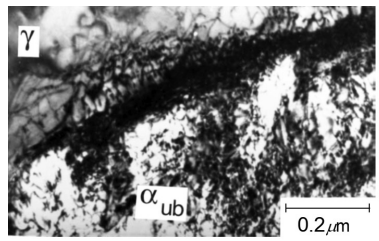

Figure 1.2.56 TEM micrograph presenting an example of intense dislocation debris with the highest density observed in the proximity of the bainite/austenite transformation front (Bhadeshia, 2001). Reprinted with permission of the publisher (Cambridge University Press).

dislocations. They are basically introduced for accommodation reasons when martensitic phases with body-centered tetragonal (BCT) structures abruptly emerge during quenching and intrude into the FCC-structured matrix phase (austenite). A close up of such an "intruded" front can be found in Figure 1.2.56 (not for a "martensitic" transformation, but for a "bainitic" one) (Bhadeshia, 2001), where extremely high-density debris of dislocations have been introduced at the austenite (γ)-bainitic ferrite (α_{ub}) interface for the purpose of accommodating the attendant incompatibility. The corresponding situations for the lath martensite formation process are schematically illustrated in Figure 1.2.57, where lath-shaped martensitic phases are nucleated and subsequently grown from the prior austenite (γ) boundaries, ultimately evolving into lath block/packet structures. Note that thus-introduced high-density dislocations are pinned by minute precipitates and/or solute atoms introduced separately, without which most of them do not remain anchored. Figure 1.2.58 shows a set of measured plots of dislocation density ρ as a function of the transformation temperature, including those not only for the martensite and bainite, but also for some ferritic phases (Bhadeshia, 2001).

https://doi.org/10.1017/9781108874069.003 Published online by Cambridge University Press

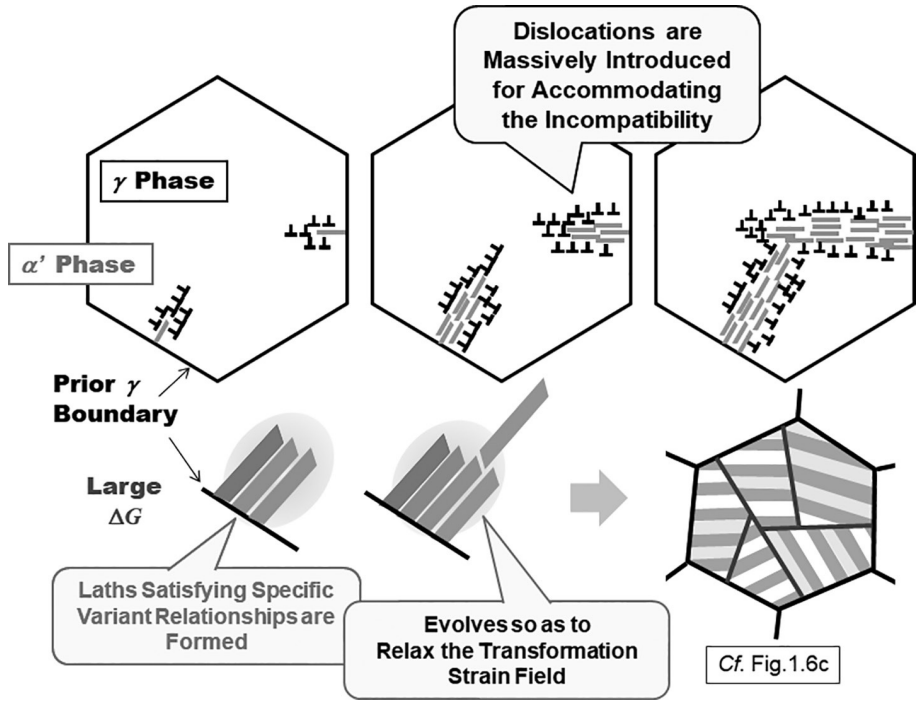

Figure 1.2.57 Schematic illustration of the lath martensite formation process under austenite/martensite transformation.

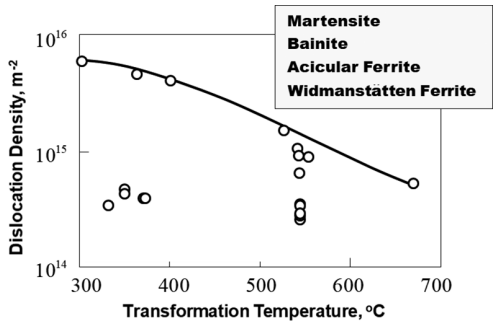

Figure 1.2.58 Variation of dislocation densities in martensite, bainite, acicular ferrite, and ferrite, with transformation temperature (Bhadeshia, 1997, 2001). Adapted with permission of the publishers (Routledge and Cambridge University Press).

1.3 Crystallography

1.3.1 Crystal Systems (Structures)

Crystal structure is typically classified into three systems as schematically depicted in Figure 1.3.1, that is, FCC, BCC, and hexagonal close-packed (HCP) structures. As

https://doi.org/10.1017/9781108874069.003 Published online by Cambridge University Press

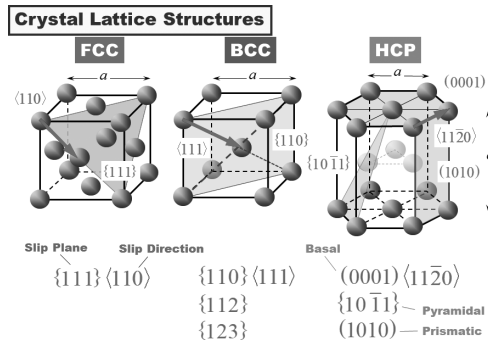

Figure 1.3.1 Typical crystal lattice structures for FCC, BCC, and HCP metals, together with representative slip systems in the Miller index notation.

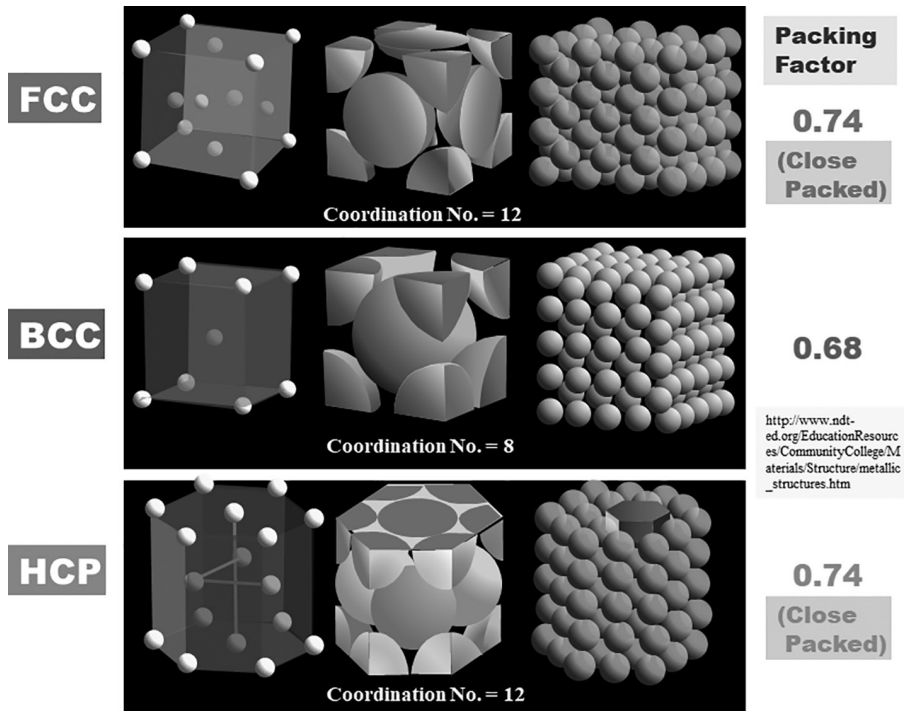

Figure 1.3.2 Various atomistic representations of typical crystal lattice structures of FCC, BCC, and HCP, together with respective coordination numbers and packing factors. This schematic is adapted by permission (© Iowa State University Center for Nondestructive Evaluation).

atomically represented in Figure 1.3.2, the FCC and HCP are the closest-packed systems with the maximum density of atoms. The isotropic bonding state of the outer-shell electrons of the metals results in these structures, while a slight distortion of the bonding structure due to additional anisotropy tends to lead HCP. The two structures differ in the order of stacking of the atomic layers. ABAB … stacking produces the HCP, while the

https://doi.org/10.1017/9781108874069.003 Published online by Cambridge University Press

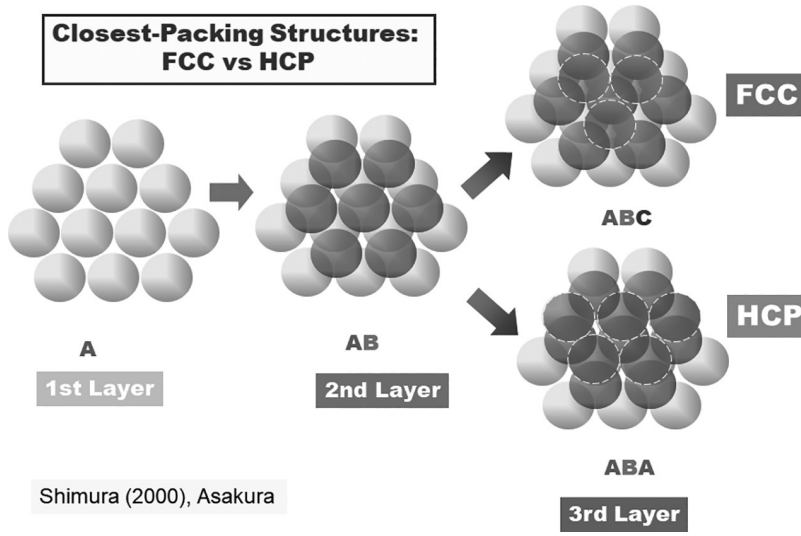

Figure 1.3.3 Distinction between FCC and HCP structures in terms of packing sequences of atomic layers (both are the closest-packing structures) (Shimura, 2000). Adapted with permission of the publisher (Asakura Publishing Co.).

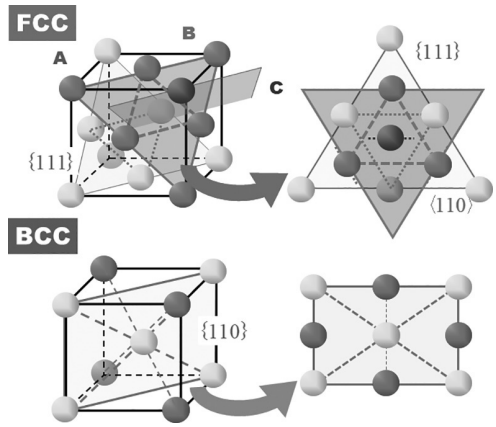

Figure 1.3.4 Comparison of stacking sequence of atoms between FCC and BCC structures.

ABCABC … stacking corresponds to the FCC, as depicted in Figure 1.3.3. As one can readily understand, these are the ways to stack bolls (atomic layers) in the densest manner.

The BCC, on the other hand, is a loosely packed system, as a result of the directionality in the electronic boding states, normally reflecting, for example, the *d*-bands for transition metals. Typical metals yielding this system are Mo, W, Ta, Nb, and Co. They have partially "covalent-type" bonds, making them relatively high-temperature resistant. The difference in the atomic stacking sequence between FCC and BCC is presented in Figure 1.3.4.

https://doi.org/10.1017/9781108874069.003 Published online by Cambridge University Press

1.3.2 FCC versus BCC

In this section, distinctions between FCC and BCC metals in terms of plasticity are discussed. In my experience, many researchers will tend to answer such a question as "what is the substantial difference between FCC and BCC?" in an obvious context. One of the most frequent answers is likely to be about "the number of slip systems." Some might mention "interactions among dislocations," especially in recent years. While these answers are true, they are rather insubstantial and rather secondary at most, in the sense that they are derivable. A more fundamental difference would be FCC and BCC's mutually "dual" construction of atomic structures, on which almost all the specifics are derived, from dislocation core structures to contrasting rate and temperature dependencies. Needless to say, this originates from the electronic structures, governed ultimately by quantum mechanics, however it is not always necessary to proceed down this path, unless chemistry is explicitly involved, as in Fe, which is revisited in Section 4.2.2 (citing a work reported in Chen et al., 2008).

The dual-atomic constitutions manifest themselves as the dual constructions of the slip systems, that is, {110}<111> for FCC and {111}<110> for BCC, as depicted in Figure 1.3.5. Note that, as is widely known, for BCC other planes containing <111> orientations may also be slip planes, for example, {112}, {123}, and so on, but they are excluded here for simplicity. As can be seen, BCC and FCC combinations are totally opposite; the slip planes in the FCC are the slip directions in the BCC and vice versa. The same is true for "twin" deformations (see Section 1.4.1).

The dual construction in the slip system is primarily due to the dual-atomistic configurations between the FCC and BCC, whose dual interrelationship is defined in the context of the reciprocal lattice (Kittel, 1953). Figure 1.3.6 provides such comparisons, summarizing the interrelationship between the FCC and BCC lattices. The reciprocal lattice to the FCC lattice agrees with the BCC lattice, and vice versa. (Note that the reciprocal of a simple cubic lattice is also a simple lattice.) In other words, the

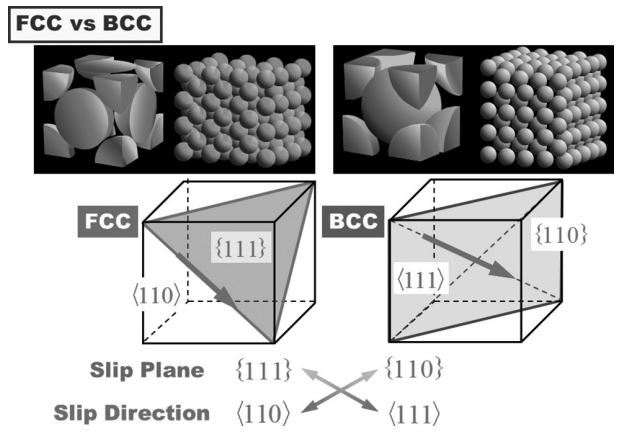

Figure 1.3.5 Dual constitution of FCC and BCC crystal structures; the nature of crystalline plasticity substantially differs between the two.

https://doi.org/10.1017/9781108874069.003 Published online by Cambridge University Press

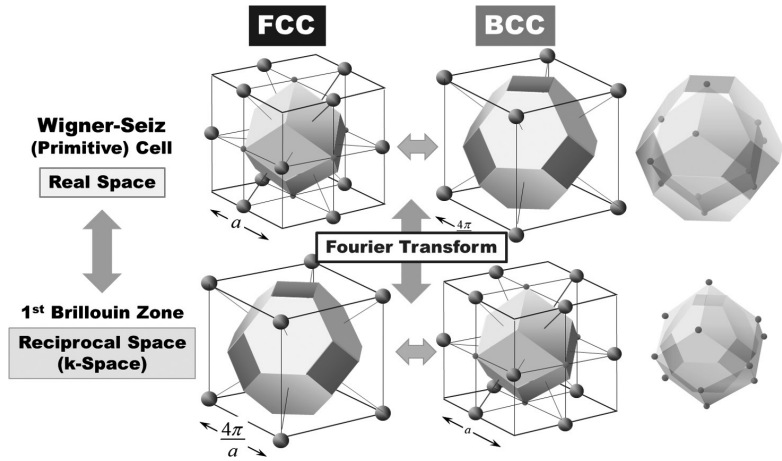

Figure 1.3.6 Dual constitution of FCC and BCC metals in terms of the atomic structure, known as Wigner–Seitz primitive cells in real space, and their reciprocal relationship, termed as the first Brillouin zone, which are mutually transferable via Fourier transform.

Fourier transform of the FCC lattice generates the BCC lattice, and the reverse is true. In the field of solid state physics, we often use the "Wigner–Seitz cell" representation in the Bravais lattice for determining the first Brillouin zone based on the reciprocal space representation, since they coincide with the Bragg-reflected wave vectors. A similar procedure with attendant "duality" is found in Section 6.6.1, where we discuss graph theory-based representation of granular assemblies It should be noted that the "Wigner–Seitz cell" is equivalent to the "Voronoi cell," constructed (drawn) via the Voronoi tessellation procedure.

Since the FCC lattice is close packed, accordingly the dual-BCC lattice is not; indeed, it may safely be stated to be "loose." From an atomistic point of view, such looseness in the packing structure of BCC metals can cause a situation whereby the closest-packed plane is not clearly identified, unlike in the FCC, and hence several "nearly" closest-packed planes can coexist. This "looseness" in packing structure is the very reason for the resulting multiple slip systems (unidentifiable slip planes) in BCC metal. Furthermore, it is the source of the often observed complexity and variety in the mechanical responses peculiar to BCC metals as well as their much higher Peierls–Nabarro (PN) stress than FCC. Immediate examples are BCC metal's strong strain rate and temperature dependencies on the stress response and the complexities in the core structure of the screw dislocation for BCC metals in general. (These will be discussed in later chapters, especially Chapter 4.)

In the case of α-Fe, this is, as a matter of fact, not a natural-born BCC metal, as is pointed out and discussed in some detail in Section 4.2.2. The specific origin of the BCC structure, coupled with the complexity in the screw core structure (see Section 4.2.1), is considered to be a crucial source of the extreme varieties in the mechanical properties of this metal. Furthermore, combined with the fact that the high temperature austenitic phase (γ-Fe) with FCC structure is within easy reach on the phase diagram

https://doi.org/10.1017/9781108874069.003 Published online by Cambridge University Press

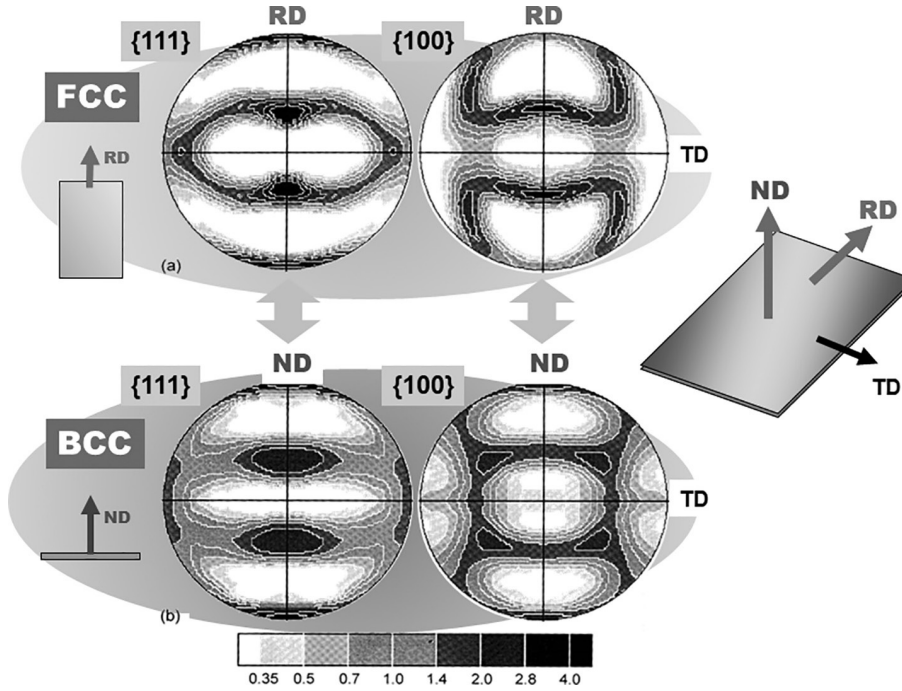

Figure 1.3.7 Intriguing correspondence in {111} and {100} pole figures representing rolling textures between FCC copper in RD and BCC Fe-3Si in ND, as a manifestation of the "dual constitution" of slip systems (Rollett and Wright, 1998). Adapted with permission of the publisher (Cambridge University Press).

via appropriate heat treatments, the complexity regarding α-Fe also provides us with such a fertile spectrum of metallurgical microstructures (such as pearlite, martensite, and bainite structures). Appreciating α-Fe this way is quite important for recognizing the phenomenology and fully understanding the necessity of multiscale approaches in the present context.

One prominent consequence of the already mentioned duality in slip-system constructions is the difference in the textures to be evolved, for example, under cold rolling (details about "texture" and "pole figure" are given in Section 1.4.2). Figure 1.3.7 compares <111> and <100> pole figures between FCC metal (Cu) and BCC alloy (Fe-3%Si) cold-rolled up to 80% reduction in thickness, where those with RD (rolling direction) for the former and ND (normal direction) for the latter are indicated (Kocks et al., 2000; Rollett and Wright, 1998). Note that the transposition of the RD and ND ensures the two sets of pole figures for FCC and BCC correspond well. This dual-texture evolution is regarded as an eloquent manifestation of the previously discussed dual construction in the atomic structures between FCC and BCC. Note that slight differences may be largely due to the geometrical effects of the elongated crystal grains along the RD, which differentiate the transposed case from the reference. As conjectured from this duality in the rolling textures, we suppose some type

https://doi.org/10.1017/9781108874069.003 Published online by Cambridge University Press

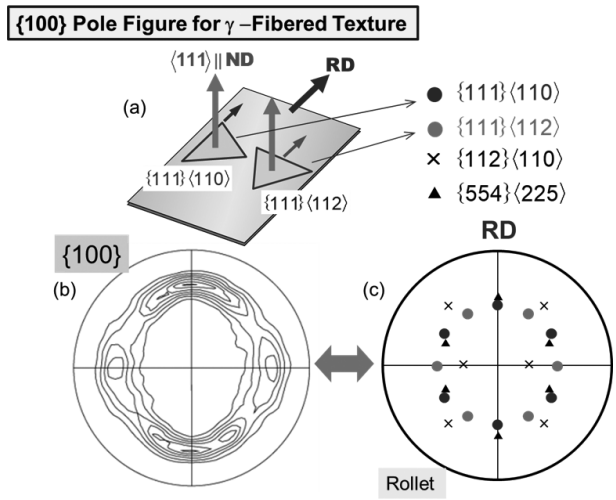

Figure 1.3.8 Typical {100} pole figure representing γ-fibered texture, specific to rolled BCC iron and IF steels, comparing experiments and a corresponding schematic.

of indigenous preferred orientation should exist in relation to the crystal structure, for example, FCC has its own inherently preferred orientations that will evolve, although the texture in FCC metals depends quite strongly on the SFE (see Figure 1.4.10). This is also true for BCC metals. Iron (Fe) or high purity steels such as IF steel, among others, are well documented to yield {111}<110>–<112> γ-fibered textures, where the {111} plane tends to be directed in parallel to the sheet sample surface, together with the preferred orientations in between <110> and <112> in RD (also expressed as that with strong <111> ‖ ND fiber). The typical γ-fibered texture for IF steels, for example, is manifested as the pole figures displayed in Figure 1.3.8, where (b) representative and (c) schematic (or ideal) {100} pole figures are compared. Since the representative γ-orientations of {111}<110> and {111}<112> are located periodically along a concentric circle on the pole figure, as shown in (c), we can understand why the experimentally observed pole figures become like the one demonstrated in (b), that is, with an isotropically converging concentration of the preferred orientation. The γ-fibered texture is revisited in Section 1.4.2, with another representation (via orientation distribution function [ODF]).

As easily imagined based on the above argument, FCC metals, having the dual-crystal structure relative to BCC metals, should give rise to totally different textures from the above, for example, β-fibered texture; it will be extremely difficult for them to yield the γ-fiber. (Typical rolling textures for FCC metals are shown in Section 1.4.2.)

1.3.3 Slip Systems in FCC and BCC

FCC metals have 12 independent slip systems, as represented in Figure 1.3.9, that is, four independent slip planes with each containing three slip directions, making the total number of the slip systems 12, where the combination of slip plane and

https://doi.org/10.1017/9781108874069.003 Published online by Cambridge University Press

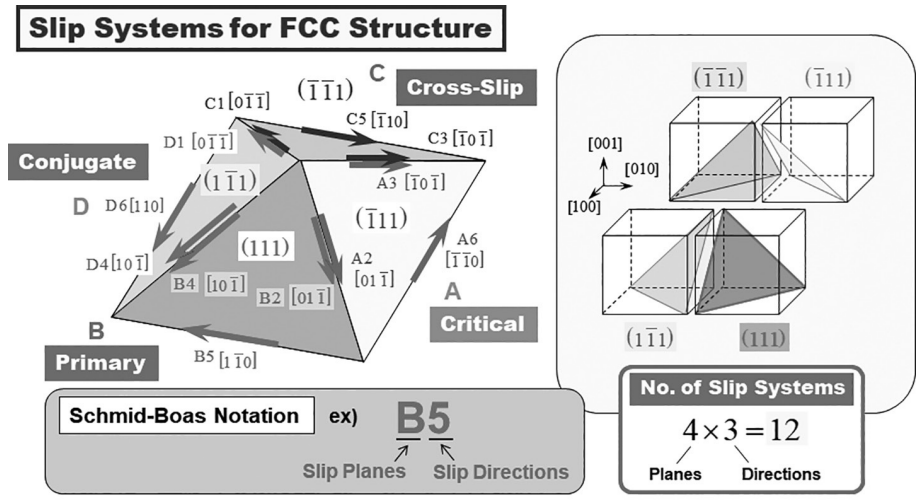

System	1	2	3	4	5	6	7	8	9	10	11	12
Schmid and Boas	B5	C5	D6	A6	B4	C3	D4	A3	B2	C1	D1	A2
Burgers vectors	$1\bar{1}0$	$1\bar{1}0$	110	110	$10\bar{1}$	101	$10\bar{1}$	101	$01\bar{1}$	011	011	$01\bar{1}$
Slip planes	111	$11\bar{1}$	$1\bar{1}1$	$1\bar{1}\bar{1}$	111	$11\bar{1}$	$1\bar{1}1$	$1\bar{1}\bar{1}$	111	$\bar{1}11$	$1\bar{1}1$	$\bar{1}11$

E. Schmid and W. Boas (1950 or 1968), "Plasticity of Crystals"
F. A. Hughes or Chapman & Hall, translation of original 1935 German edition.

Figure 1.3.9 Slip systems for FCC metals, consisting of four crystallographically equivalent slip planes, each having three independent slip directions, based on Schmid–Boas notations.

direction is called "slip system." The four slip planes are often referred to as primary (B), conjugate (D), cross-slip (C), and critical (A), respectively, according to their configurations and roles viewed from the primary system (B), while the slip directions are labeled by numbers corresponding to the six independent directions, that is, from 1 through 6. The combination of them (A–D and 1–6) is referred to as the Schmid–Boas notation (Schmid and Boas, 1950 [1968]), which is widely used in the literature for identifying each slip system. For example, "B2" denotes the slip system on the primary plane (B) with direction 2. Figure 1.3.10 displays the corresponding vector representations, where $\boldsymbol{m}^{(\alpha)}$ and $\boldsymbol{s}^{(\alpha)}$ indicate the unit vectors for the slip plane normal and the slip direction (i.e., that of the Burgers vector), respectively, with the superscript (α) denoting the slip system, that is, $\alpha = 1, 2, \ldots, 12$ for FCC metals. These notations are further used in the mathematical treatment of crystal plasticity, partially mentioned in conjunction with the Schmid factor (SF) (e.g., Figure 1.3.17).

As is inferred from the "FCC versus BCC" arguments in Section 1.3.2, BCC has a dual construction of slip systems in contrast to that of FCC crystals. The closest-packed plane for BCC crystals is {110} and we normally regard the associated slip systems of the {110}<111> type as the representative system. Figure 1.3.11 displays the 12 independent slip systems of the {110} type for BCC metals, that is, six equivalent slip planes with two slip directions each, summarized in Figure 1.3.11 in terms of the Schmid–Boas notation. The corresponding vectorial representations are given in

https://doi.org/10.1017/9781108874069.003 Published online by Cambridge University Press

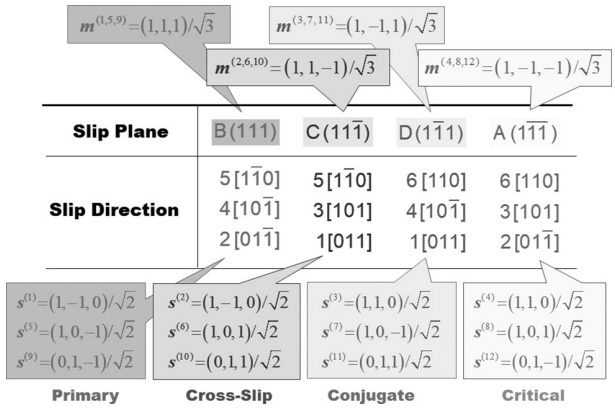

Figure 1.3.10 Explicit expressions of slip systems for FCC in Figure 1.3.9 via unit vectors for slip planes and slip directions (i.e., the Burgers vector) of FCC metals.

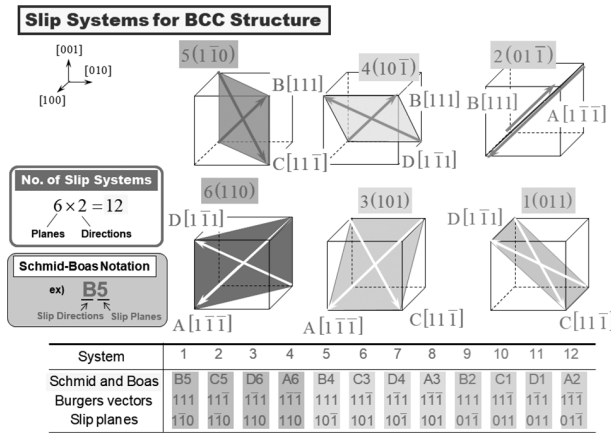

Figure 1.3.11 Slip systems for BCC metals ({110}<111> type only), consisting of six crystallographically equivalent slip planes, each having two independent slip directions, based on Schmid–Boas notations, yielding dual construction, in contrast to those of FCC counterparts shown in Figure 1.3.9.

Figure 1.3.12. From the figure, one can confirm the "duality" relative to FCC, especially by looking at the Schmid–Boas notation, that is, "A–D" denotes the slip directions, while "1–6" expresses the slip plane, based on which we readily obtain a set of expressions for BCC from that of FCC via simple transpositions of $\boldsymbol{s}_{\mathrm{fcc}}^{(\alpha)} \to \boldsymbol{m}_{\mathrm{bcc}}^{(\alpha)}$ and $\boldsymbol{m}_{\mathrm{fcc}}^{(\alpha)} \to \boldsymbol{s}_{\mathrm{bcc}}^{(\alpha)}$. Here, to avoid confusion, the subscript "fcc/bcc" is attached to the plane normal and direction vectors.

As pointed out in Section 1.2, BCC-constituting atomic structures are relatively loosely packed compared to FCC's (compare the packing factors listed in Figure 1.3.2), which gives rise to difficulty in distinguishing the most densely stacked planes from others, that is, there exist plural dense planes very close to the densest

https://doi.org/10.1017/9781108874069.003 Published online by Cambridge University Press

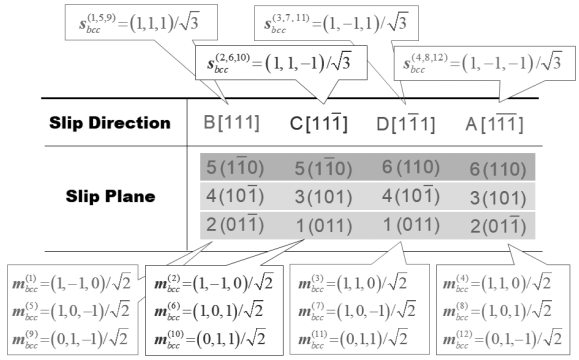

Figure 1.3.12 Explicit expressions of slip systems for BCC in Figure 1.3.11 via unit vectors for slip planes and directions (i.e., the Burgers vector), yielding dual construction in contrast to those for FCC metals in Figure 1.3.10.

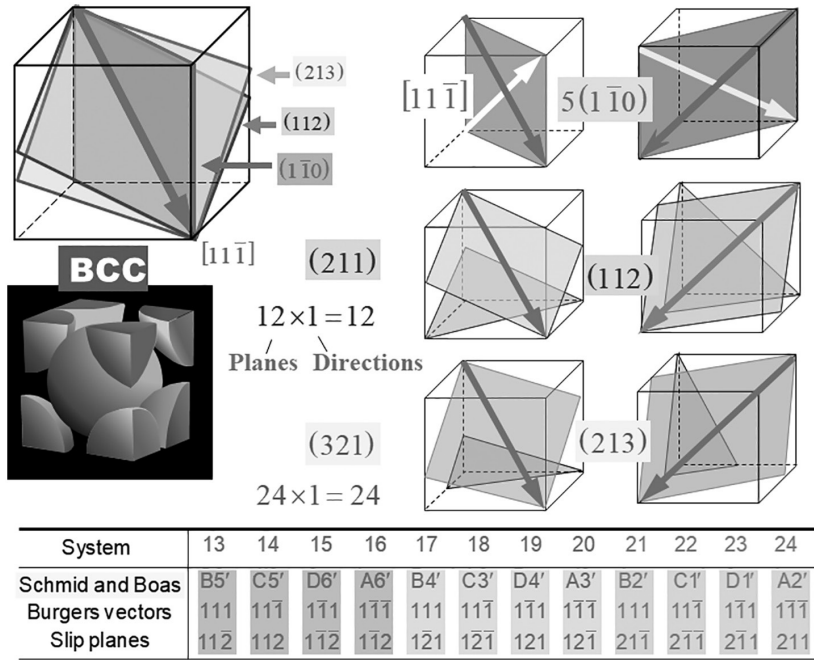

Figure 1.3.13 Three typically recognized slip planes for BCC metals containing the common slip direction in the <111> orientation.

one. This serves as the major reason for the indefinite slip planes often observed in BCC metals, combined with the extremely large SFEs, manifested typically for α-Fe as "wavy" slip-traces (c) and "pencil glide" (d) in Figure 1.2.41.

Figure 1.3.13 summarizes a set of generally postulated variations of the slip planes for BCC structures, that is, {110}, {112}, and {123}, where the most densely packed

https://doi.org/10.1017/9781108874069.003 Published online by Cambridge University Press

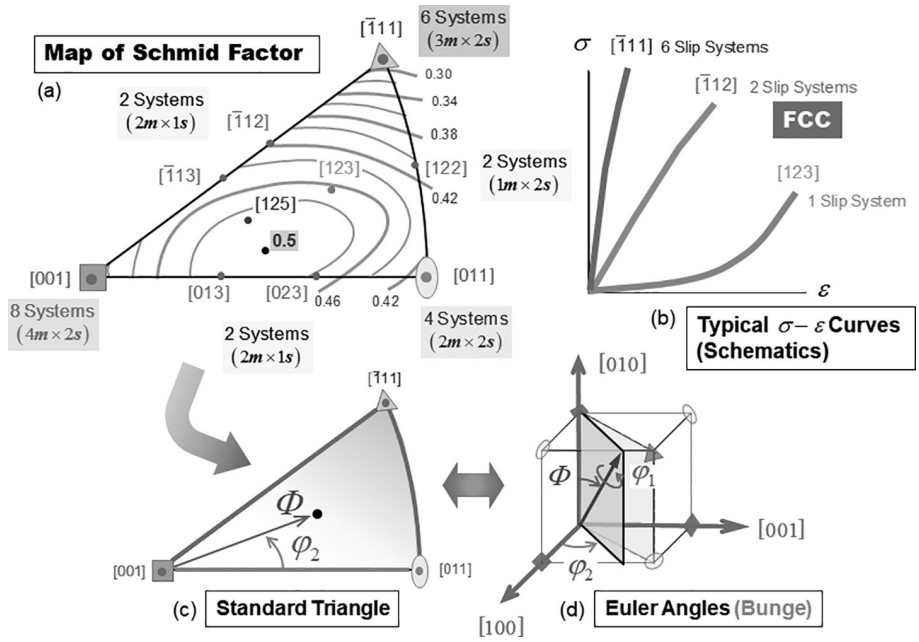

Figure 1.3.14 SF map applicable both to FCC and BCC crystals, together with schematically drawn typical stress–strain curves in the case of FCC metals.

direction is uniquely identified to be <111>, providing the definite slip direction of BCC metals. This can be visually confirmed also in Figure 1.3.13, where these three planes intersect on the common <111> line, and hence they are called to form the <111> zone. The independent slip planes for {112} and {123} types are partially shown in the figure, having 12 and 24 slip systems, respectively. Therefore, BCC metals have 48 slip systems altogether if we assume all the contributions from the above three kinds including the {123}<111> types.

Since the SF is measured by $(\boldsymbol{s}^{(\alpha)} \otimes \boldsymbol{m}^{(\alpha)})_{\mathrm{sym}}$, as detailed in Section 1.3.4, we notice from the earlier discussion about duality in slip systems between FCC and BCC, namely $(\boldsymbol{s}_{\mathrm{fcc}}^{(\alpha)} \otimes \boldsymbol{m}_{\mathrm{fcc}}^{(\alpha)})_{\mathrm{sym}} = (\boldsymbol{s}_{\mathrm{bcc}}^{(\alpha)} \otimes \boldsymbol{m}_{\mathrm{bcc}}^{(\alpha)})_{\mathrm{sym}}$, that two crystal systems' SFs coincide, as far as the {110} types for BCC are concerned. Figure 1.3.14 shows the contour map of the SF, commonly applicable to both the crystal structures. The map is drawn on the standard triangle of the stereographic projection (see Figure 1.4.13 for details), together with the number of active slip systems under tension in the prescribed orientations. The orientations [001], [111], and [011], located at the apices of the triangle, are highly symmetric, which are followed by orientations along the edges (with two equivalent slip systems), as explicitly specified in (a). The orientations inside the triangle, on the other hand, yield low symmetry, manifesting a limited number of slip-system activities, for example, single slip. Some immediate examples of the corresponding stress–strain curves are schematically shown in (b), showing a highly symmetric multiple slip orientation [111] (six equivalent slip systems) and a

https://doi.org/10.1017/9781108874069.003 Published online by Cambridge University Press

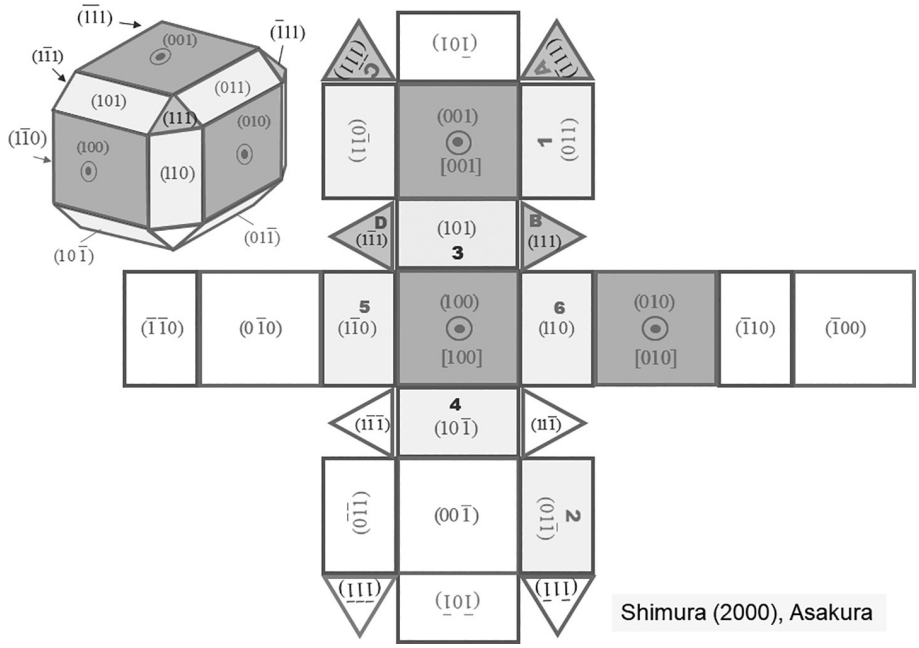

Figure 1.3.15 A do-it-yourself kit of cubic structure model containing all the fundamental planes of {100}, {110}, and {111} (Shimura, 2000). Adapted with permission of the publisher (Asakura Publishing Co.).

single-slip orientation [123], together with a moderately symmetric orientation along the triangle edge [-112] (two slip systems), for FCC metals, as examples. Single-slip orientations tend to yield two- to three-stage hardening, as also detailed in Figure 3.1.6 in conjunction with evolving dislocation structures, and revisited in Figure 4.1.3 in the context of "single crystal versus polycrystal" plasticity.

Regarding the SF, such low-symmetric orientations are apt to take relatively larger values, stemming from the biased activities of their slip systems, with a maximum of 0.5 realized at [149], followed by, for example, 0.497 at [136], and so on, located inside the triangle, as a natural consequence.

For easy understanding of the slip-system configurations for FCC and BCC crystals, Figure 1.3.15 provides a do-it-yourself kit for representing all the typical planes including <111> and <110>, in addition to the <100> cube planes for cubic structures (Shimura, 2000). The completed drawing is shown in the upper left.

1.3.4 RSS and the SF

For discussing slip-system activities and/or slip-system-wise shear deformations, we use the RSS. Figure. 1.3.16 illustrates how we define the RSS together with the associated SF. The force F acting on the cylindrical sample, as in the figure, is projected onto the slip plane in the slip direction, inclined by ϕ from the loading axis, that is,

https://doi.org/10.1017/9781108874069.003 Published online by Cambridge University Press

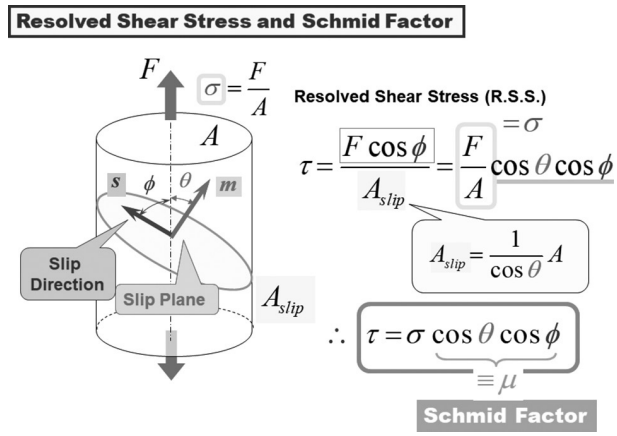

Figure 1.3.16 Schematics showing how to obtain the RSS, where the SF is defined as the measure for evaluating slip activities.

$F\cos f$. By dividing it by the area of the slip plane $A_{\text{slip}} = A/\cos\theta$, we obtain the RSS, that is,

$$\tau = \frac{F\cos\phi}{A_{\text{slip}}} = \frac{F}{A}\cos\theta\cos\phi \tag{1.3.1}$$

Since $F/A = \sigma$, we finally have

$$\tau = \sigma\cos\theta\cos\phi. \tag{1.3.2}$$

Here, the prefactor $\cos\theta\cos\phi \equiv \mu$ is called the SF, which measures the RSS. By using this factor, we can distinguish the activity of the slip systems, for example, "primary" or "secondary," and "active" or "inactive."

The equation for finding the RSS can be generalized into the one for the tensorial definition, which serves as the foundation of the kinematics of crystal plasticity (e.g., Asaro et al., 2003; Khan and Huang, 1995; Nemat-Nasser, 2004). Figure 1.3.17 displays the process and the definition. The SF is generalized as the Schmid tensor, indicating 3D slip-system constitutions, defined as

$$P_{ij}^{(\alpha)} = \frac{1}{2}\left(s_i^{(\alpha)}m_j^{(\alpha)} + s_j^{(\alpha)}m_i^{(\alpha)}\right), \tag{1.3.3}$$

$$\boldsymbol{P}^{(\alpha)} = \left(\boldsymbol{s}^{(\alpha)}\otimes\boldsymbol{m}^{(\alpha)}\right)_{\text{sym}} = \frac{1}{2}\left(\boldsymbol{s}^{(\alpha)}\otimes\boldsymbol{m}^{(\alpha)} + \boldsymbol{m}^{(\alpha)}\otimes\boldsymbol{s}^{(\alpha)}\right), \tag{1.3.4}$$

where $s_i^{(\alpha)}$ and $m_j^{(\alpha)}$ are unit vectors representing the slip direction and slip plane normal belonging to the slip system specified by the superscript (α), respectively. The subscript "sym" in Eq. (1.3.4) denotes "symmetrization." By using the Schmid tensor, we can calculate the RSS via

$$\tau = P_{ij}^{(\alpha)}\sigma_{ij}\,, \tag{1.3.5}$$

$$\tau = \boldsymbol{P}^{(\alpha)}:\boldsymbol{\sigma} = tr(\boldsymbol{P}^{(\alpha)}.\boldsymbol{\sigma}), \tag{1.3.6}$$

https://doi.org/10.1017/9781108874069.003 Published online by Cambridge University Press

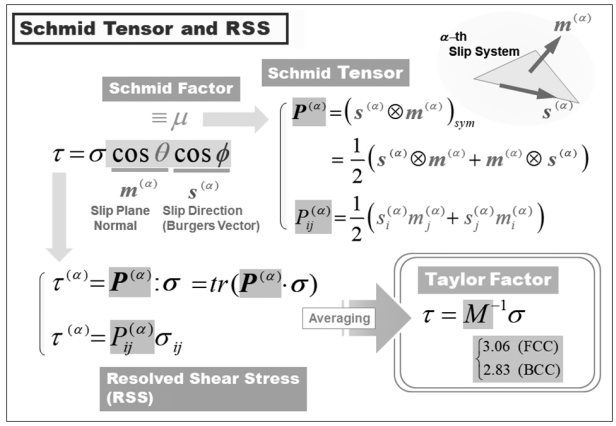

Figure 1.3.17 Three-dimensional generalization of the SF, referred to as the Schmid tensor or direction tensor, which is constructed by the tensor product of two unit vectors representing slip direction and slip plane normal, together with the corresponding relationship for calculating the RSS. Two expressions, via direct and index notations, indicated for both SF and RSS, are presented.

where ":" denotes the scalar product for tensors. The rewriting of the second expression in Eq. (1.3.6) is simply due to a computational reason, because algorisms for calculating the multiplication $\boldsymbol{P}^{(\alpha)}\cdot\boldsymbol{\sigma}$ are simpler than directly computing $\boldsymbol{P}^{(\alpha)}:\boldsymbol{\sigma}$.

It is also known that BCC metals do not always obey the Schmid law, often referred to as the "non-Schmid effect," requiring additional calculations (Ito and Vitek, 2001). Some related topics are discussed in Section 4.2 in relation to the complexity of screw core structures peculiar to BCC metals.

When the SF is summed up over multi-orientations for the purpose of representing polycrystal versions of the relationship between σ and τ, this is called Taylor factor, that is, M for $\sigma = M\tau$. Roughly, it has been reported that $M = 3.06$ for FCC metals and $M = 2.83$ for BCC metals (Figure 1.3.17).

The skew-symmetric part of $\boldsymbol{s}^{(\alpha)}\otimes\boldsymbol{m}^{(\alpha)}$, defines the spin tensor, to be used in the kinematics of finite crystal plasticity formulation for expressing deformation-induced lattice rotations, that is,

$$W_{ij}^{(\alpha)} = \frac{1}{2}\left(s_i^{(\alpha)}m_j^{(\alpha)} - s_j^{(\alpha)}m_i^{(\alpha)}\right), \tag{1.3.7}$$

$$\boldsymbol{W}^{(\alpha)} = \left(\boldsymbol{s}^{(\alpha)}\otimes\boldsymbol{m}^{(\alpha)}\right)_{\text{skew}} = \frac{1}{2}\left(\boldsymbol{s}^{(\alpha)}\otimes\boldsymbol{m}^{(\alpha)} - \boldsymbol{m}^{(\alpha)}\otimes\boldsymbol{s}^{(\alpha)}\right), \tag{1.3.8}$$

where "skew" indicates "skew (anti)-symmetrization."

1.3.5 Dislocation–Dislocation Interactions Revisited: Interaction Matrix

Figure 1.3.18 displays an example of the interaction matrix for FCC metals, classifying the kinds of pairwise interaction for the arbitrary combinations of the slip systems. In the case of FCC metals, such interactions are expressed by a 12×12 matrix. Here,

https://doi.org/10.1017/9781108874069.003 Published online by Cambridge University Press

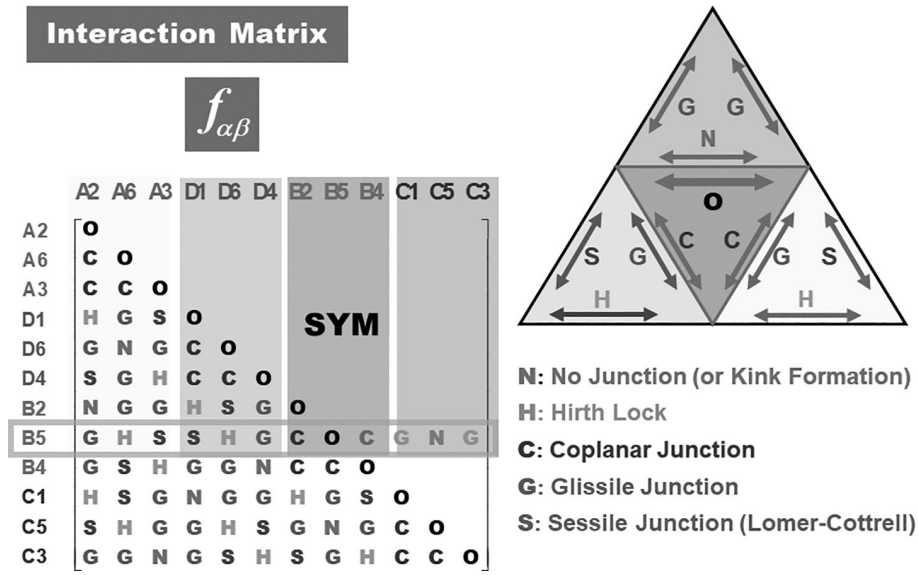

Figure 1.3.18 Example of an interaction matrix for FCC metals expressing kinds and strengths of dislocation–dislocation interactions, also explaining how to view the interaction matrix, for example, from the primary slip system denoted by thick double-pointed arrow in Thompson's tetrahedron on the right.

the Schmid–Boas notation (see Figure 1.3.9) is used to symbolize the slip systems. The inset shows a 2D representation of Thompson's tetrahedron, expressing the constitution of the FCC slip systems, together with the interactions specified with respect to the primary slip system, indicated by a broad doubled-pointed arrow.

The interactions among dislocations in FCC metals have empirically been classified into five kinds, that is, (**O**) self-hardening, (**H**) Hirth lock or reaction-producing jogs, (**C**) coplanar junction among those on the same slip plane, (**G**) glissile junction, and (**S**) LC sessile junction. The last one is described in detail in Section 1.2.5.5. The interaction associated with the LC sessile junction formation exhibits the maximum strength, which is followed by the glissile lock. There have been arguments about the others (Bassani and Wu, 1991; Francoisi et al., 1980).

Also explained in Figure 1.3.18 is how to read the interaction matrix. If the primary system denoted by **O** be the reference, which corresponds to B5 according to the Schmid–Boas notation (corresponding to the slip system along the lower edge of the primary plane in Figure 1.3.9), we need first to find it in the row. As can be confirmed in the figure, "B5" is located on the eighth row from the top. Then we can identify all the interactions with arbitrary others by looking at this row. For example, the interaction with D1 is found to be "**S**," meaning LC sessile junction formation, and so on.

The values of the components in the above interaction matrix, that is, the strengths of the interactions, can be identified (or at least evaluated) by a series of experiments which make up the latent hardening test.

https://doi.org/10.1017/9781108874069.003 Published online by Cambridge University Press

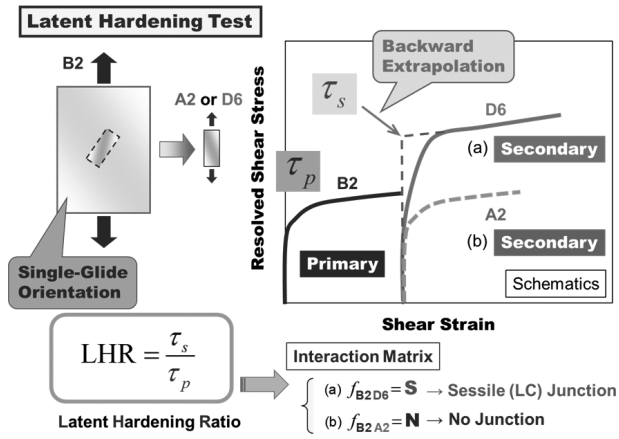

Figure 1.3.19 Schematics of the latent hardening test consisting of two-step loading (tensile) tests, by which the components in the interaction matrix can be evaluated (Wu et al., 1991). Adapted with permission of the publisher (Royal Society Publishing).

Schematics of the latent hardening test are shown in Figure 1.3.19, where a two-step test on a single crystal specimen is performed. The details of the test are as follows. The first test is conducted on a parent specimen normally directed in single slip, and the second test follows it on a child sample machined from the parent with a specified direction from its stress axis, such that the interaction between the primary slip system activated in the first test and the latent systems start operation in the second test can be measured. The graph in the figure shows an example of the output results, where shear stress–strain curves for the primary and the secondary tests are indicated, from which the latent hardening ratio (LHR) is obtained as

$$\mathrm{LHR} = \frac{\tau_s}{\tau_p}. \tag{1.3.9}$$

Here, τ_p and τ_s are the values of flow stress in the primary and secondary tests, respectively, where A2 or D6 orientation is assumed in the secondary tension against a B2 primary orientation, corresponding to LC junction and no junction formations, respectively, as extrema. There are some arguments about how to determine τ_s since the secondary curve contains a number of subtleties. Usually the backward extrapolation is employed, as in the figure.

Examples of experimentally observed responses for Cu are displayed in Figures 1.3.20 (Wu et al., 1991) and 1.3.21 (Jackson and Basinski, 1967), respectively. In the former (Figure 1.3.20), the backward extrapolation procedure is indicated for evaluating the secondary flow stress. In Figure 1.3.21, on the other hand, three secondary orientations of B2, A2, and D1 are chosen against the B4 primary counterpart, corresponding to **G** (glissile junction) in common in the interaction matrix $f_{\alpha\beta}$ listed in Figure 1.3.18. As observed, D1 and A2 exhibit marked stress increase around the reyielding, whereas B2 shows no additional hardening but is demonstrated to smoothly continue the primary stress curve. Since B4 → B2 is classified as **C**

https://doi.org/10.1017/9781108874069.003 Published online by Cambridge University Press

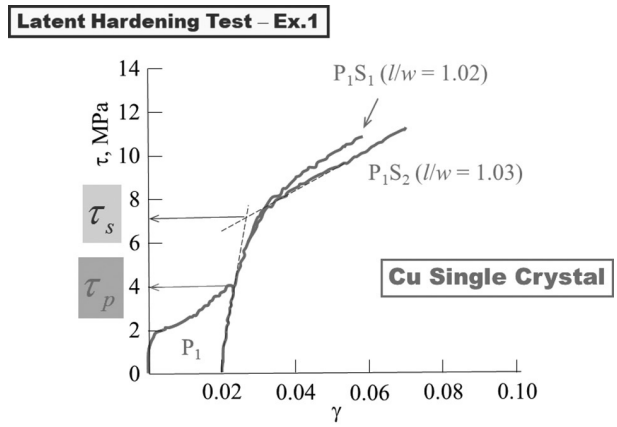

Figure 1.3.20 Example of the latent hardening test for a Cu single crystal (Nemat-Nasser, 2004; Wu et al., 1991). Adapted with permission of the publishers (Cambridge University Press and Royal Society Publishing).

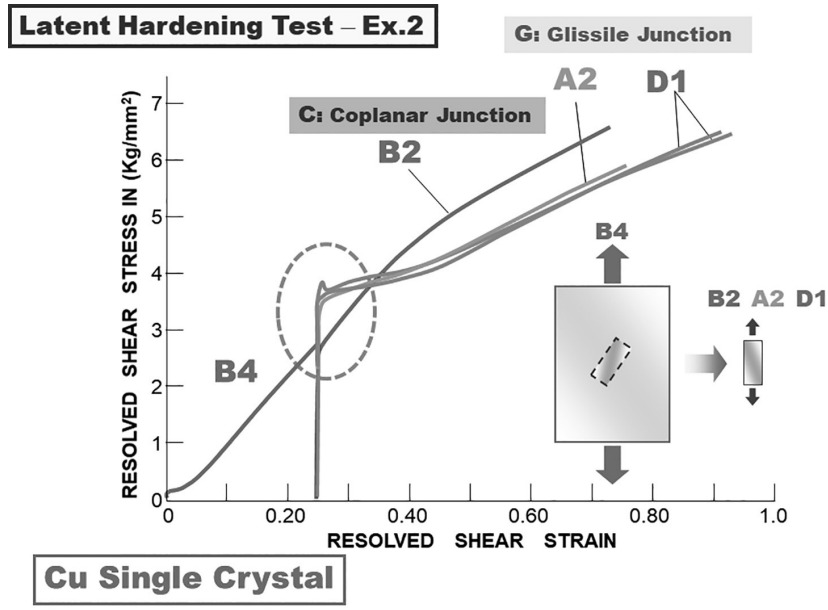

Figure 1.3.21 Examples of latent hardening test results with various orientations in the secondary experiments for a single crystal Cu (Jackson and Basinski, 1967). Adapted with permission of the publisher (Canadian Science Publishing).

(coplanar junction) in $f_{\alpha\beta}$, the present result implies no distinction among the three coplanar slip systems in their contributions to the strain hardening at least for Cu, meaning that the **C** component in $f_{\alpha\beta}$ is supposed to take the value of 1.0, that is, no extra/additional contribution to the self-hardening.

https://doi.org/10.1017/9781108874069.003 Published online by Cambridge University Press

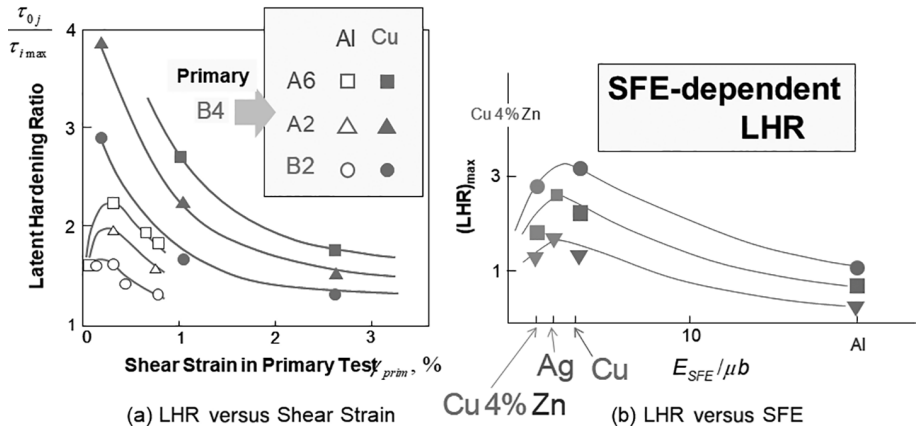

Figure 1.3.22 Variations of LHR with (a) shear stress in the primary test (Francoisi et al., 1980) and (b) normalized SFE (Francoisi, 1985), respectively, where the maximum values of LHR are used for each material for the latter (b). The primary system for all the tests is B4, yielding formations of sessile (A6), glissile (A2), and coplanar junctions (B2), respectively. Adapted with permission from the publisher (Elsevier Science & Technology Journals).

It is noteworthy that the components of the interaction matrix $f_{\alpha\beta}$ are not constant in general, but roughly yield a decreasing function of the primary shear strain, as shown in Figure 1.3.22(a). From the comparison of LHR among the secondary orientations, A6, A2, and B2, not only can we confirm the strength order of the dislocation interactions as **S** (sessile) > **G** (glissile) > **C** (coplanar), but we also learn that all these interactions follow the same decreasing trend for both Al and Cu. It is further worth noting that a rough negative correlation of the LHRs for **S**, **G**, and **C** with increasing SFE exists, as observed in Figure 1.3.22(b). This corroborates the summarized overview concerning SFE-hardening behavior relationship for FCC metals given in Figure 1.2.48.

We next consider the case of BCC metals, although they have been quite limited, in contrast to FCC metals, primarily due to complexity relating to BCC indefinite slip-system activities (cf. Figures 1.2.41 and 1.2.13). Among others, Nakada and Keh (1966) systematically investigated – for single crystal Fe, choosing $[11\bar{1}]$ as the primary system direction – the effects of a Burgers vector combination, the amounts of prestrain, and temperature, concluding the LHR tends to vary between 1.2 and 1.4, roughly independent of those factors. Figures 1.3.23 and 1.3.24 show examples of their results. In Figure 1.3.23, what we can readily confirm is the markedly pronounced additional hardening at yielding compared to the FCC cases shown earlier, followed by similar flow responses regardless of the secondary slip systems (oriented in #1$[\bar{1}1\bar{1}]$, #2 $[\bar{1}\bar{1}\bar{1}]$, #3 $[1\bar{1}1]$, and #4 $[111]$). In Figure 1.3.24, on the other hand, an exceptionally high rate of additional hardening is found for the reloaded curve #4′, in which two secondary slip systems, where double slip with $[1\bar{1}1]$ and $[1\bar{1}\bar{1}]$ directions are activated simultaneously, distinctly differ from FCC. Figure 1.3.24 provides a comparison of results for the case of "coplaner" latent hardening, where the RSS was designated to be zero on the latent system during the first test, and, similarly, the

https://doi.org/10.1017/9781108874069.003 Published online by Cambridge University Press

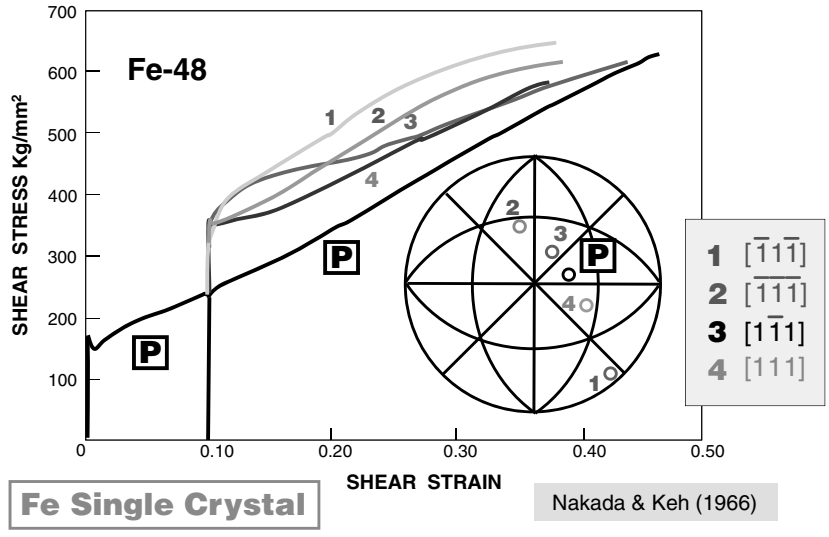

Figure 1.3.23 Examples of latent hardening tests for a BCC Fe single crystal with various secondary orientations, denoted as 1 to 4 on the stereographic projection (Nakada and Keh, 1966). Adapted with permission of the publisher (Elsevier Science & Technology Journals).

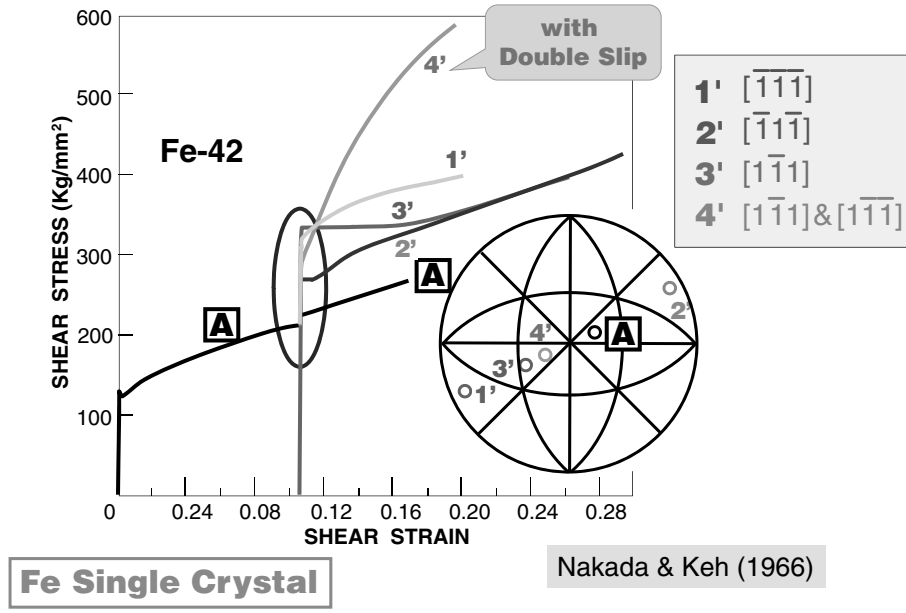

Figure 1.3.24 Examples of latent hardening tests for a BCC Fe single crystal with various secondary orientations, denoted as 1′ to 4′ on the stereographic projection, with 4′ being double-slip oriented (Nakada and Keh, 1966). Adapted with permission of the publisher (Elsevier Science & Technology Journals).

https://doi.org/10.1017/9781108874069.003 Published online by Cambridge University Press

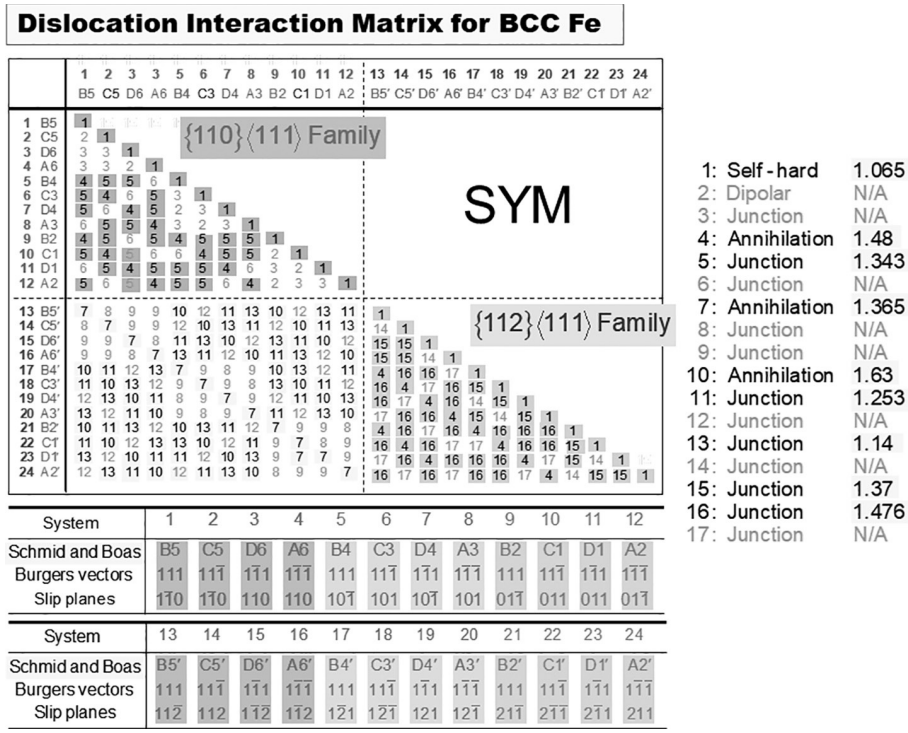

System	1	2	3	4	5	6	7	8	9	10	11	12
Schmid and Boas	B5	C5	D6	A6	B4	C3	D4	A3	B2	C1	D1	A2
Burgers vectors	111	$11\bar{1}$	$1\bar{1}1$	$1\bar{1}\bar{1}$	111	$11\bar{1}$	$1\bar{1}1$	$1\bar{1}\bar{1}$	111	$11\bar{1}$	$1\bar{1}1$	$1\bar{1}\bar{1}$
Slip planes	$1\bar{1}0$	$1\bar{1}0$	110	110	$10\bar{1}$	101	$10\bar{1}$	101	$01\bar{1}$	011	011	$01\bar{1}$

System	13	14	15	16	17	18	19	20	21	22	23	24
Schmid and Boas	B5′	C5′	D6′	A6′	B4′	C3′	D4′	A3′	B2′	C1′	D1′	A2′
Burgers vectors	111	$11\bar{1}$	$1\bar{1}1$	$1\bar{1}\bar{1}$	111	$11\bar{1}$	$1\bar{1}1$	$1\bar{1}\bar{1}$	111	$11\bar{1}$	$1\bar{1}1$	$1\bar{1}\bar{1}$
Slip planes	$11\bar{2}$	112	$1\bar{1}2$	$1\bar{1}2$	$12\bar{1}$	$12\bar{1}$	121	$12\bar{1}$	$21\bar{1}$	$21\bar{1}$	$2\bar{1}1$	211

Figure 1.3.25 Interaction matrix for BCC Fe integrated from literatures, that is, with reactions classified by Madec and Kubin (2004), and values evaluated by Francoisi (1983).

RSS on the primary system was zero during the second test, meaning latent hardening in the absence of secondary activation of the slip systems. Relatively large coplaner interaction is observed, which is another feature of BCC metals.

Figure 1.3.25 provides an example of the interaction matrix for BCC Fe which will be used in the simulations that follow in the present book. The values of the components are determined in an integrated manner and refer to several data sources, that is, the classification of the interactions is based on a series of dislocation dynamics simulations (Madec and Kubin, 2004; Tang et al., 1999), and the values themselves specified in the list in the right are from those evaluated by Francoisi (1983) in the latent hardening tests, where the slip systems are limited to the {110}<111> and {112}<111> families, that is, B5 through A2 and B5′ through A2′, respectively. Since there is no distinction in the reaction of the two dislocations, the interaction matrix in this case is symmetric. Note that in the following series of simulations we used "1.0" for components not available in the literature.

Figure 1.3.26 displays another source of the interaction matrix for BCC metal (Cuitinõ et al., 2001) where a specific interaction, that is, between a moving edge dislocation and a stationary screw dislocation, forming jogs as a result of the reaction, is considered (see also Figure 1.2.49(a)). Cuitinõ et al. evaluated all the 24×24 interactions in terms of the formation of energy based on energy and mobility considerations for Ta. Since the reactions of an edge dislocation against a screw counterpart

https://doi.org/10.1017/9781108874069.003 Published online by Cambridge University Press

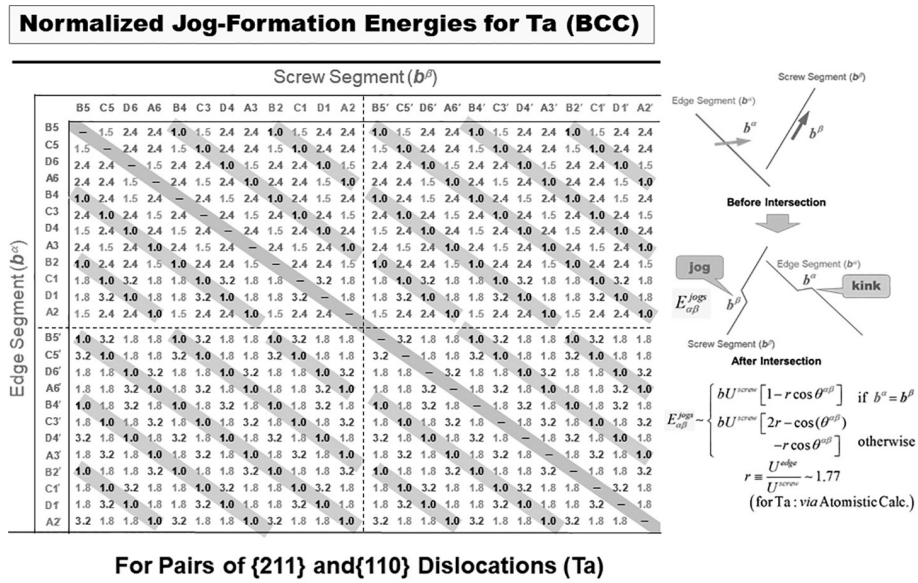

Figure 1.3.26 Interaction matrix for BCC Ta representing normalized jog formation energy numerically evaluated (Cuitinõ et al., 2001).

are assumed, the matrix becomes asymmetric, in contrast to that in Figure 1.3.25. Sorting the original matrix by the number, from 1 through 24, used in Figure 1.3.25, we notice some noteworthy features that are roughly classified into four submatrices corresponding to the reactions for

(1) {110} edge against {110} screw (upper left),
(2) {110} edge against {112} screw (upper right),
(3) {112} edge against {110} screw (lower left), and
(4) {112} edge against {112} screw (lower right),

exhibiting mutually common trends in the component structure, with some minor exceptions, for example, periodically crossing cater-corner bands of "1.0" or "-" (shaded in the figure), and intercorrespondence of the values between "1.5 and 3.2" and "2.4 and 1.8" (these can be mutually converted by swapping). These common features imply qualitatively similar contributions of the {110}<111> and {112}<111> family dislocations to the jog formations.

1.4 Miscellaneous

1.4.1 Twin

Another mode of plastic deformation is "twinning." There are two types of twin in terms of their forming mechanisms, that is, annealing twin and deformation (or mechanical) twin. The former is introduced to reduce the energy of the system as a

https://doi.org/10.1017/9781108874069.003 Published online by Cambridge University Press

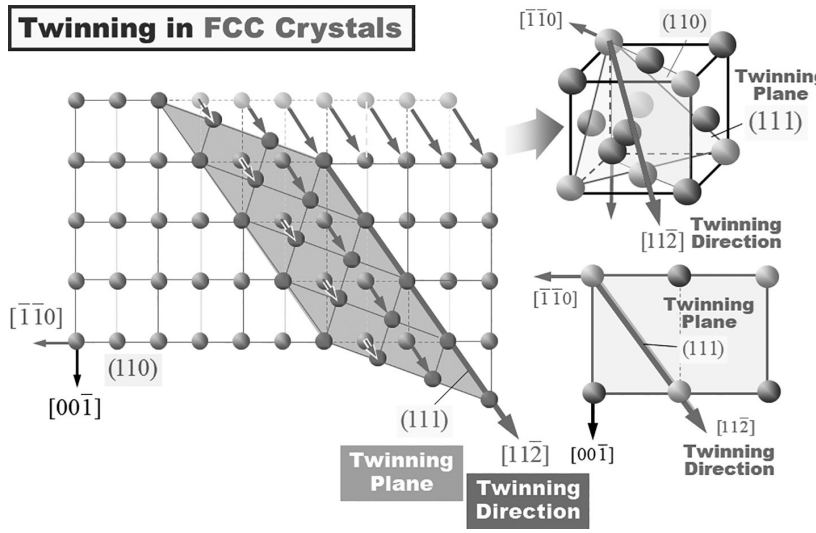

Figure 1.4.1 Schematics of twinning in FCC metals.

part of "static recovery" in the absence of stress or deformation, while the latter takes place in order to accommodate the imposed deformation under stress. This subsection basically deals with the latter – deformation twin.

The deformation twin is considered to be a major deformation mode for HCP metals, and also for some FCC metals with low SFE less than 25 mJ m^{-2} and BCC metals under high strain rates and low temperatures. Even in FCC metals with intermediate SFE around 50–70 mJ m^{-2} (such as Cu and Ni), where most of the plastic deformation can be carried out by the dislocation motion, mechanical twinning can take place, for example, under impact or hypervelocity impact loading, as partially shown in Figure 3.5.2. It is known that the critical stress for the onset of mechanical twinning for FCC metals is in proportion to the SFE. This means that small SFE metals and alloys (such as α-brass and SUS304 [austenitic stainless steels]) tend to exhibit mechanical twinning quite easily.

Figures 1.4.1 and 1.4.2 detail the crystallography of the twinning for FCC and BCC metals, respectively. As can be confirmed by comparing the two, putting them side by side, as in Figure 1.4.3, there also exists a "dual" constitution, that is, {112}<111> for FCC and {111}<112> for BCC. It is worth comparing this with the case of "slip" in Section 1.3.2 or Figure 1.3.5.

For BCC metals, another distinction should be kept in mind, which is that between twin and antitwin directions, depending on the directionality of deformation due to its geometrical constitution, causing, for example, tension–compression asymmetry. Note that the emission of a partial dislocation from a GB in nanocrystalline aggregates, leading to the formation of twins across the grain, has been considered to be responsible for the outset of plastic deformation in such nanocrystal samples (e.g., Asaro et al., 2003; Van Swygenhoven et al., 2002).

https://doi.org/10.1017/9781108874069.003 Published online by Cambridge University Press

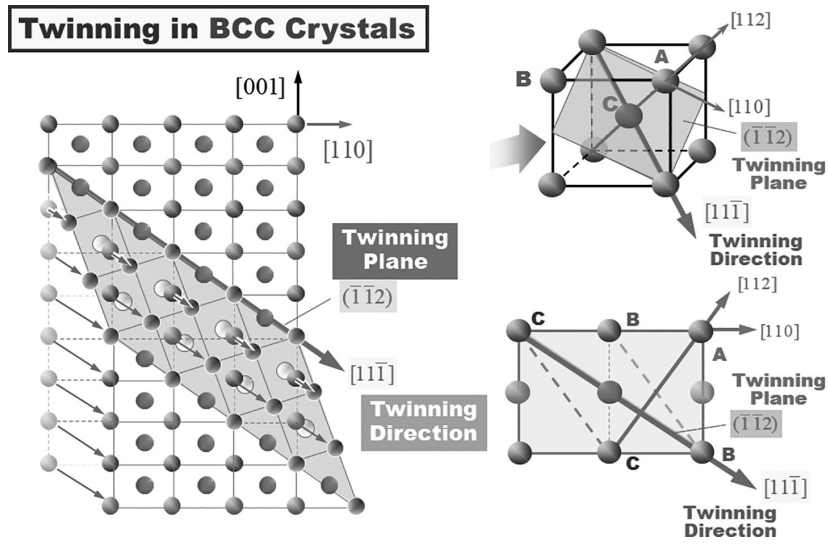

Figure 1.4.2 Schematics of twinning in BCC metals.

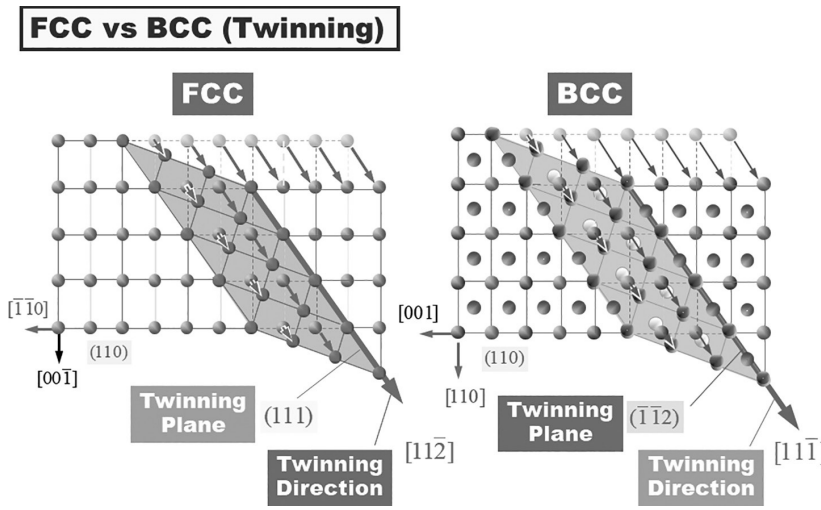

Figure 1.4.3 Duality in twin deformation modes between FCC and BCC metals as a consequence of their dual constitution of crystallographic structures.

Figure 1.4.4 presents a schematic comparison of dislocation-based representations of "twin" and "microband (MB)" between FCC and BCC (Murr et al., 1996), where we can find some similarity between the twin and MB, except for the case of twin for FCC. Comparisons between deformation twins and MBs formed under oblique shock/hypervelocity impact loading for Cu can be found in Figure 1.4.5, which demonstrates the micrographically resembling morphologies between them. It is worth noting that

https://doi.org/10.1017/9781108874069.003 Published online by Cambridge University Press

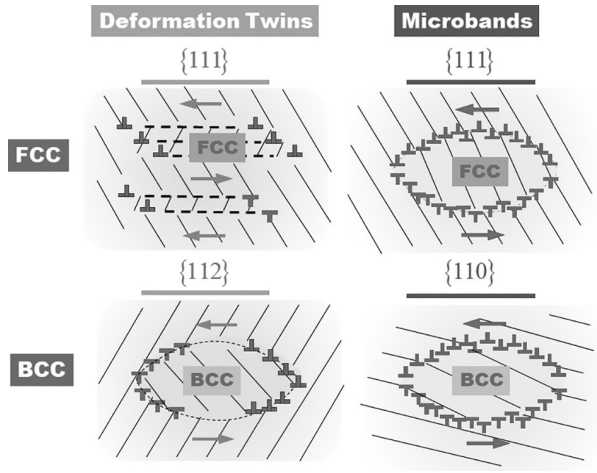

Figure 1.4.4 Schematics of deformation twins and MBs, comparing FCC and BCC metals and demonstrating the similarity of the two deformation modes (Murr et al., 1996, p. 131, figure 8). Adapted with permission of the publisher (ASM International).

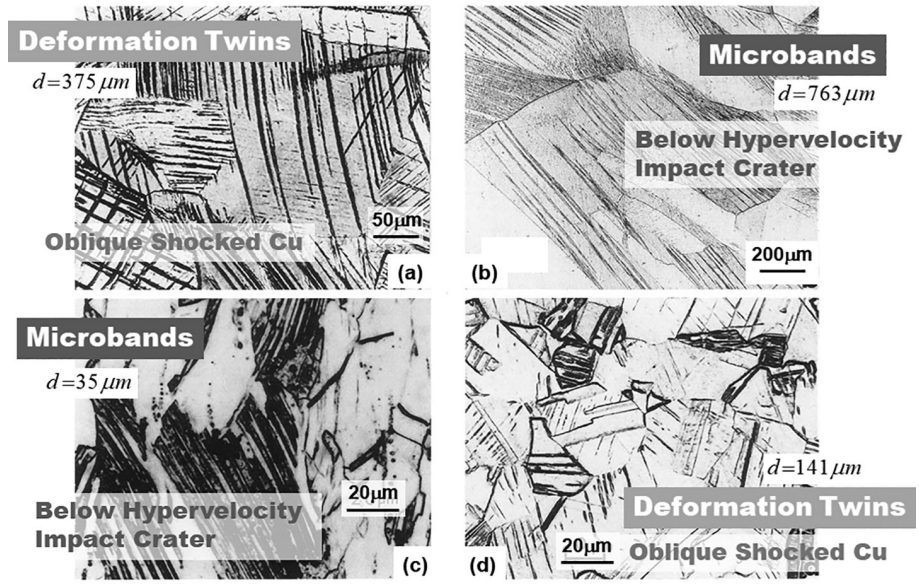

Figure 1.4.5 Comparison of deformation twin and MB formed on a polycrystalline Cu surface: (a)(d) twins in oblique shocked copper targets with d_G = 375 μm and 141 μm, respectively, and (b)(c) MBs below hypervelocity impact crater in copper targets with d_G = 763 μm and 35 μm, respectively (Murr et al., 1996, p. 124, figure 2). Adapted with permission of the publisher (ASM International).

https://doi.org/10.1017/9781108874069.003 Published online by Cambridge University Press

the arrays of dislocations illustrated there will not always be "lattice" dislocations, but more likely CD ones (namely, "virtual" – see Section 1.4.4 for details). This tends to mean researchers experienced in TEM observations may not always accept (or be rather skeptical about) such dislocation-based representations.

The twinning in FCC can be interpreted quite distinctly from that in BCC, as a serial stacking of plural "stacking faults" sandwiched between pairs of partial dislocations. Therefore, the formation mechanism is greatly attributed to the motion of leading and trailing partial dislocations.

Since, basically, both the twins and MBs are well described as CD dislocations to be introduced via accommodation of a sort of "excessive" local deformation, extended use of the "incompatibility tensor"-based model will be effective for descriptions of them, as discussed in Chapter 11 in the context of application to single crystal pure Mg.

1.4.2 Texture and Pole Figure

Another important item to be added to Part I, "Fundamentals," is "texture," especially rolling texture, that is, recrystallization texture and deformation texture. Figure 1.4.6 provides a schematic drawing of the rolling process of sheet metal, together with the attendant deformation of crystal grains rotated toward and elongated into the RD. This is accompanied by the developments of "preferred orientations" of grains in addition to their significant shape changes. The term "texture" refers formally to the former, the preferred orientation, not the latter. However, the actual texture, presented via the pole figure or ODF, inevitably includes the effect of such morphological aspects of the composing grains, together with likely occurring intragranular inhomogeneous deformations manifested as various forms of deformation structure (cf. Chapter 3). Representative rolling textures are schematically summarized in Figure 1.4.7, that is, cube, copper, brass, γ, and gross orientations, expressed via $\{hkl\}\langle uvw\rangle$ as $\{rolling\ direction\}\langle rolling\ plane\rangle$, together with their relationships with the Bunge-type Euler angles $(\varphi_1, \Phi, \varphi_2)$. Euler angles are described in some detail in Appendix A1.7.

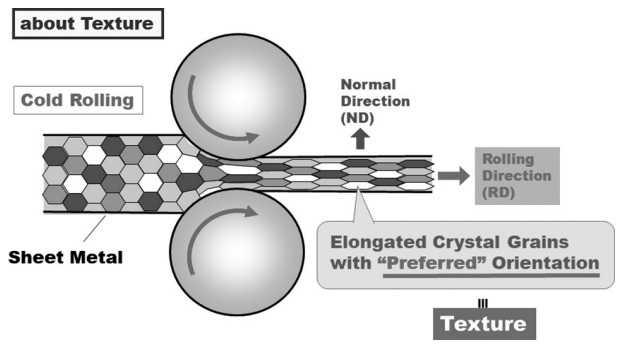

Figure 1.4.6 Schematic illustration of rolling process and attendant "texture" development with preferred orientation.

https://doi.org/10.1017/9781108874069.003 Published online by Cambridge University Press

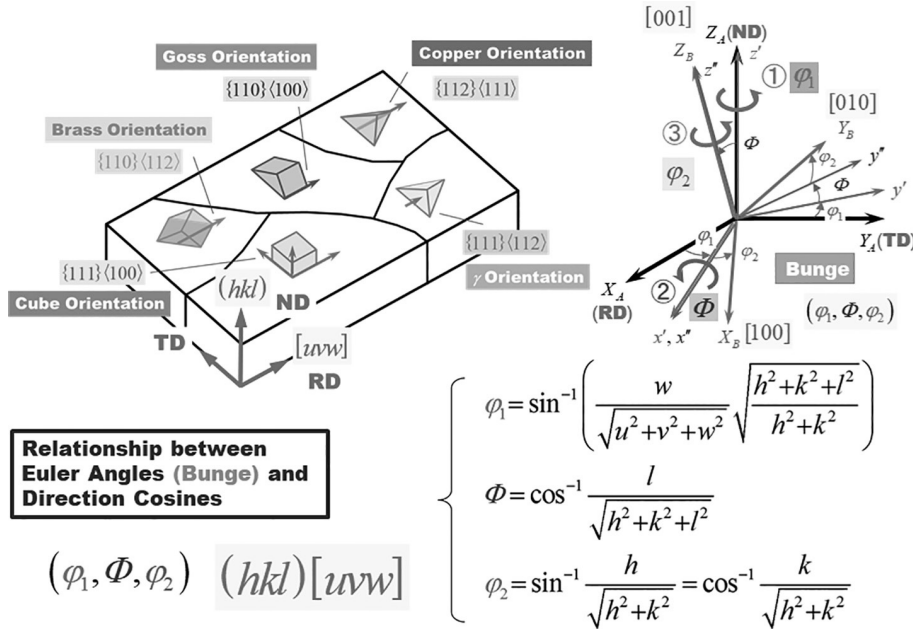

Figure 1.4.7 Schematics showing representative rolling textures, that is, cube, gross, and γ orientations, together with copper and brass orientations, represented as {rolling plane}<rolling direction>.

For scrutinizing the texture, we generally need the pole figure, or more precisely, the ODF for their 3D totality. Figure 1.4.8 concisely explains how we obtain a pole figure, while Figure 1.4.9 provides an overview of the ODF, both assuming texture presentations. The pole figure is a 2D stereographic representation of the orientation of a "selected" plane normal (pole) with respect to the sample reference frame, often utilized to describe texture, for example, for a rolled sheet metal, on which a set or group of all the equivalent specific crystallographic orientations of the crystal phases involved in the targeted sample are stereographically projected. In Figure 1.4.8, a <100> pole is taken as an example with respect to a sample reference frame, specified as RD, ND, and transverse direction (TD). Here, a single crystal cube located at the center of a projection sphere is depicted, from which three cube directions of [100], [010], and [001] are ultimately projected onto the projection plane, resulting in the pole figure (a). By repeating the process, we obtain the corresponding plot (b) and the contour plot (c), indicating the intensity of such distributions of projected points. For the ODF, on the other hand, Figure 1.4.9 displays presentations in (a) full 3D, (b) 2D, and (c) a selected 2D Euler angle space $(\varphi_1, \Phi, \varphi_2)$, together with typical examples of the rolling textures (c) and (d), respectively, specifying typical α, β, and γ fibered textures. Special emphasis is placed on the γ fibered texture, to be discussed as follows.

As shown already in the context of "FCC versus BCC" (in Section 1.4.1), the dual constitution of the atomic structures is also manifested as distinct textures of high contrast between them (see Figure 1.3.7). Typical textures for FCC metals observed

https://doi.org/10.1017/9781108874069.003 Published online by Cambridge University Press

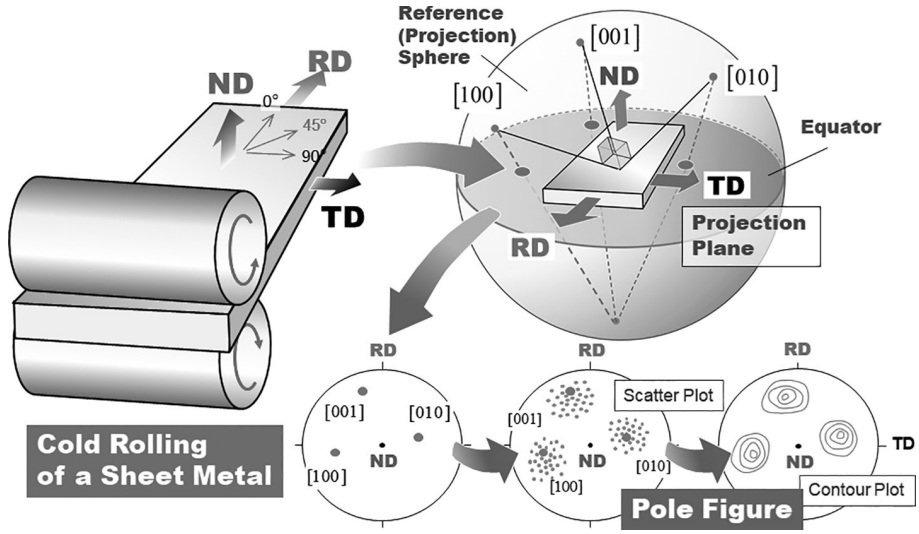

Figure 1.4.8 Schematic drawing showing how to obtain and view the pole figures for a textured sheet via cold rolling, taking an example of {100} poles of a cubic single crystal. A stereographic projection of <100> directions onto a projection plane is illustrated, together with rolling, transverse, and normal directions of the rolled sheet sample, indicated as RD, TD, and ND, respectively (Hatherly and Hutchinson, 1979).

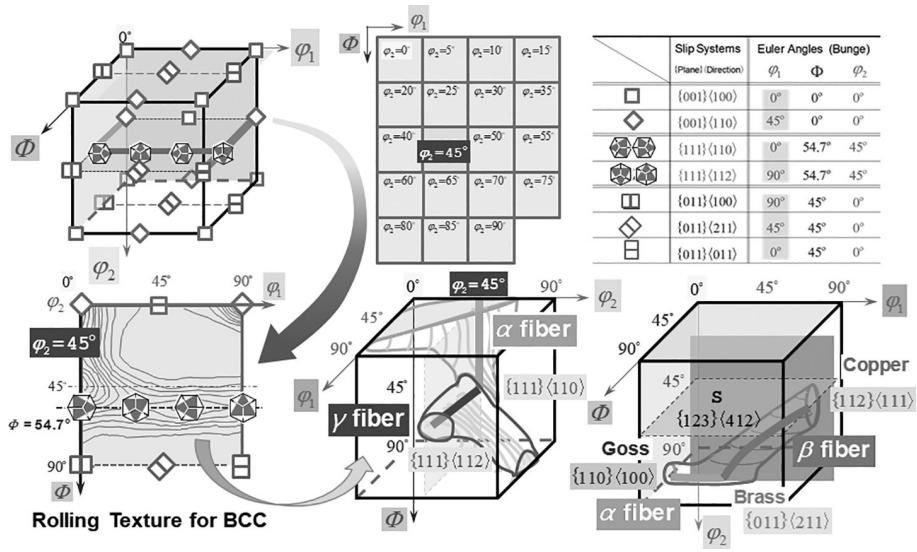

Figure 1.4.9 An overview of the ODF presented in Euler angle space, $(\varphi_1, \Phi, \varphi_2)$, with an emphasis on the γ fibered texture, typical to Fe and low-carbon steels such as IF steel. (a) 2D presentation on the (φ_1, Φ) plane at $\varphi_2 = 45°$ (Urabe and Jonas, 1994, p. 437, figure 4), (b) 3D view of (b) (Hirsch and Lücke, 1988a, p. 142, figure 5(b)), and (c) that for FCC metals, schematizing typical rolling textures (Hirsch and Lücke, 1988b, p. 2869, figure 3). Adapted with permission of each publisher (Iron and Steel Institute of Japan, Hindawi, and Elsevier).

https://doi.org/10.1017/9781108874069.003 Published online by Cambridge University Press

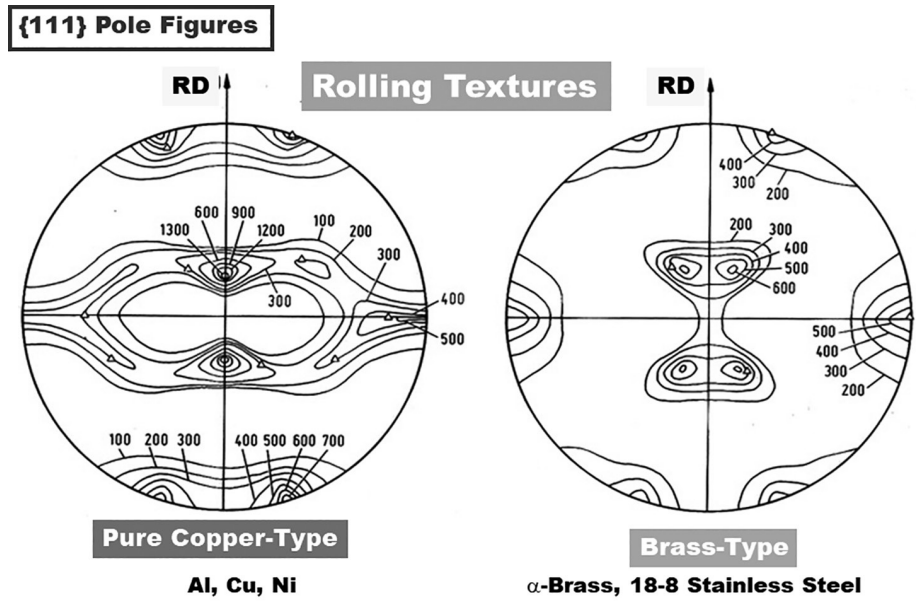

Figure 1.4.10 Typical pole figures in FCC metals, referred to as "pure copper" type and "α-brass" type (Hu et al., 1952). Used with permission of The Minerals, Metals & Materials Society.

in cold rolling are depicted in Figure 1.4.10, that is, (a) pure Cu type and (b) α-brass type compared on {111} pole figures (Hu et al., 1952), where the former is for 95%-rolled Al, while the latter is 95%-rolled for 70–30 brass. The BCC metals, on the other hand, have their own counterpart, widely known as γ-fibered texture (see Figure 1.3.8). It is worth noting that the difference observed between (a) and (b) in Figure 1.4.10 is largely attributed to the difference in the SFE, where type (b) is considered to be greatly affected by the alternative deformation mode, that is, twinning (Section 1.4.1). The former type of pole figure (described as $(123)[\bar{4}\bar{1}2]$ and $(146)[\bar{2}\bar{1}1]$) has been widely observed for FCC metals with relatively high SFE, whereas the latter type (described as $(110)[\bar{1}12]$) for those with low SFE such as brass and silver (Ag). Transition reported from the former toward the latter seems to be very informative, realized by decreasing the rolling temperature down to −196°C (e.g., Hu and Goodman, 1963), demonstrating that the high-intensity areas near the center of the former tend to split, eventually becoming closer to the former as a function of temperature. These authors discussed the close relationship with SFE change.

For the case of the γ-fibered texture for BCC metals mentioned in Section 1.3.2 in the context of high *r*-value, the <100> pole is often used where the intensity tends to be concentrated in the circular region, as schematically illustrated in the top right of Figure 1.4.11 for the case of IF steels. With this type of texture, the *r*-value can reach 2.5 or more.

https://doi.org/10.1017/9781108874069.003 Published online by Cambridge University Press

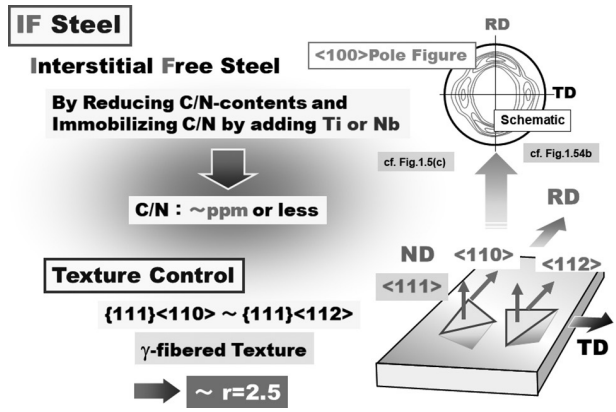

Figure 1.4.11 Schematics showing a typical texture called γ-fiber found in mild steels such as IF steels, where the C-impurity level is significantly reduced down to a few ppm or less, with the residuals being anchored by adding Ti or Nb as a form of TiC/NbN, and so on.

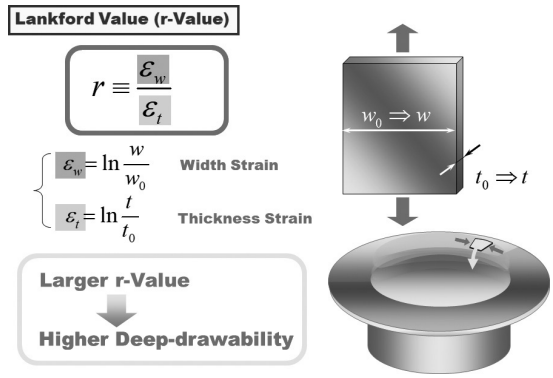

Figure 1.4.12 Definition of r-value (also referred to as the Lankford value) as a measure of deep drawability.

Incidentally, the γ-fibered texture has been known to be suitable for press forming, especially in deep drawing, because of its superior thinning resistance manifested as high *r*-value (Lankford value or plastic anisotropy parameter [Wagoner and Chenot, 2001]). The *r*-value, as schematically explained in Figure 1.4.12, is defined by the ratio of width strain ε_w to the thickness strain ε_t, that is,

$$r \equiv \frac{\varepsilon_w}{\varepsilon_t} \text{ with } \begin{cases} \varepsilon_w = \ln(w/w_0) \\ \varepsilon_t = \ln(t/t_0) \end{cases} \tag{1.4.1}$$

As understood from Eq. (1.4.1), the large *r*-value means to yield, for example, a large transverse deformation with a relatively small thickness reduction. In the metal-forming technology, this provides an index of deep drawability, since the large

https://doi.org/10.1017/9781108874069.003 Published online by Cambridge University Press

r-value yields easier shrink-type flanging deformation, allowing larger amount of materials to be drawn into a die cavity (the ability to allow circumferential shrinkage at the flange part against the reducing thickness).

The high *r*-value in the γ-fibered texture (~2.5 or larger) basically stems from the intrinsic slip-system constitutions to BCC metals as described earlier. As can be imagined, with the {111} plane in parallel to the sheet surface, the deformation through thickness direction is restricted because the slip direction <111> is normal to the surface of the sheet, as schematically illustrated in Figure 1.4.11. It is interesting to note that some researchers, assuming the same mechanism will work, have tried to realize the γ-fibered texture in certain kinds of aluminum alloy (FCC) for the purpose of enhancing the press formability. As readers may readily notice, this will probably not be possible due to the following three reasons: (1) the γ-fibered texture is indigenous to BCC structures, (2) the relationship between the γ-fibered texture and high *r*-value is peculiar to BCC metals, and (3) the slip plane to be aligned in parallel to the blank sheets ought to be {110} for FCC metals according to the above logic.

1.4.3 Stereographic Projection and Standard Triangle

One of the standard ways of describing crystallographic orientations explicitly is via stereographic projection. This is also called the "inverse" pole figure, since in this case the crystallographic axes are taken as the reference, instead of the targeted sample, as in the pole figure (see Figure 1.4.8 in Section 1.4.2). A way to obtain the stereographic projection is schematically given in Figure 1.4.13, where a two-step projection is indicated, that is, (a) from a cube (of atomic structure) to an enveloping sphere, and (b) from the sphere to a tangent circle. The resultant projection is shown in (c), where a standard triangle out of the 24 geometrical equivalents is highlighted. The standard triangle is composed of the three representative orientations of <100>, <110>, and <111>. Note that the term "stereographic projection" itself stands for the projection of a sphere onto a plane, corresponding to the above process (b), which preserves local angles (referred to as the conformal transformation [or map]) but not length or area.

Arbitrary crystallographic orientation is represented as a dot in the standard triangle, as exemplified in Figure 1.3.14(a). It should be noted that the dot in the standard triangle, however, does not contain all the crystallographic information because it represents just a single direction with respect to the cube axes. Based on Euler angles, it is represented by two angles, for example (Φ, φ_2). Therefore, we need one more piece of information about the direction to fully identify the 3D configuration of the crystallographic orientation, for example, $(\varphi_1, \Phi, \varphi_2)$, as in the ODF described earlier (Figure 1.4.9).

Figure 1.4.14 summarizes the stereographic projections described in Sections 1.4.2 and 1.4.3, by compactly combining Figures 1.4.8 and 1.4.13, emphasizing the obtaining processes up to the resultant pole figure and the standard triangle, respectively. Here, the cubic structure model provided as the do-it-yourself kit in Figure 1.3.15 is

https://doi.org/10.1017/9781108874069.003 Published online by Cambridge University Press

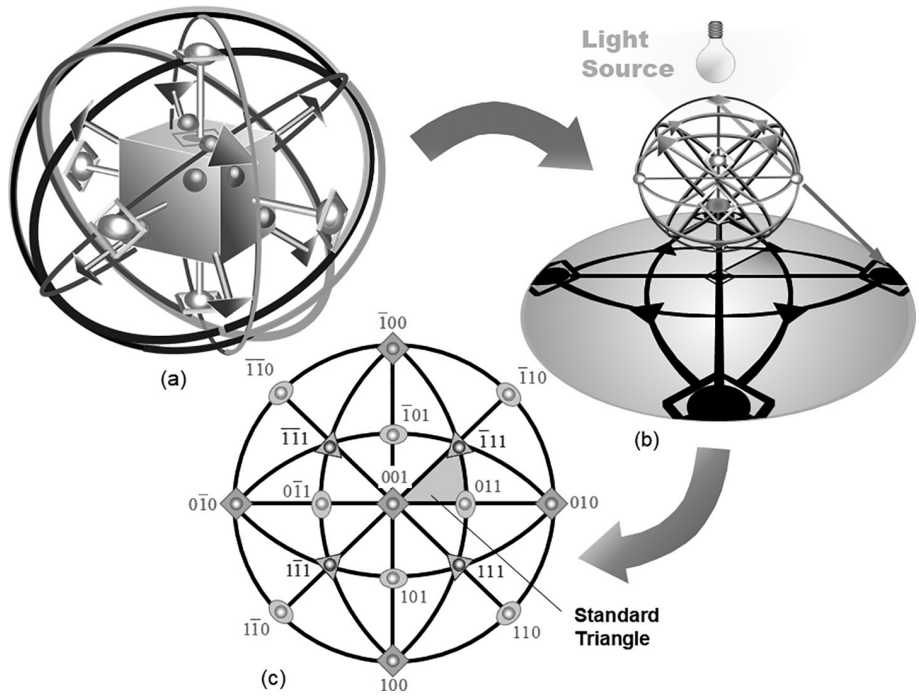

Figure 1.4.13 Schematic illustration of the process for obtaining stereographic projection of directions in a cubic crystal, where a standard triangle is highlighted in (c) ((a) and (b) are reconstructed from Marder, 2000, p. 33, figure 2.17). Adapted with permission of the publisher (John Wiley & Sons).

used as the cube to be projected in the place of the one situated in Figure 1.4.13(a), for the sake of easier comparisons.

1.4.4 Crystal Dislocations versus CD Dislocations

There is often confusion among researchers about the distinction between "CD dislocations" and "lattice or crystal dislocations." They are, as a matter of fact, essentially distinct concepts (Shiotani, 1989; Yokobori, 1968; Yokobori and Ichikawa, 1967). As pointed out in Section 1.2.1, the notion of "dislocations" (of the CD kind) were initially introduced within the continuum mechanics framework (Love, 1944; Volterra, 1907) with no explicit correspondence to the "crystal" dislocations. Furthermore, the concept had been used in solving mechanics problems of continuum solids (not based on crystalline plasticity). While the crystal dislocations have a finite Burgers vector roughly commensurate with the lattice constant of the crystal considered, the CD dislocations have an infinitesimal Burgers vector. Unless at least the slip systems are specified and projected onto it, we cannot interpret the CD dislocations as the crystal counterparts. The CD dislocations can be imaginary, and do not always need to correspond to (or be attributed to) the "crystal" ones.

https://doi.org/10.1017/9781108874069.003 Published online by Cambridge University Press

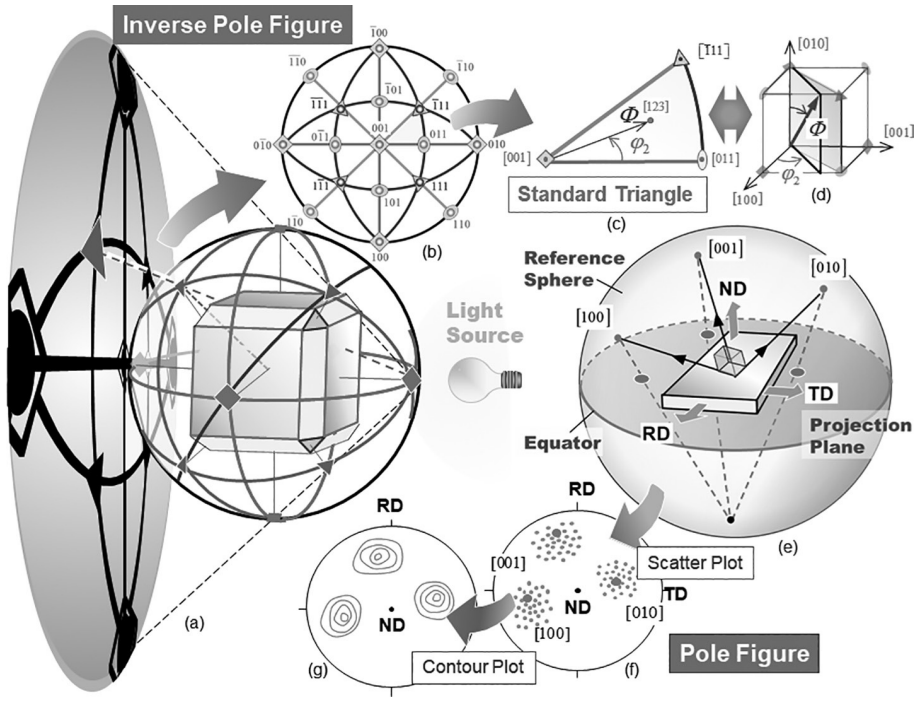

Figure 1.4.14 Summary overview of two stereographic projections in Figures 1.4.8 and 1.4.13, that is, pole and inverse pole figures, comparing how to obtain and how to view the pole figures, taking an example of {100} poles of a cubic single crystal.

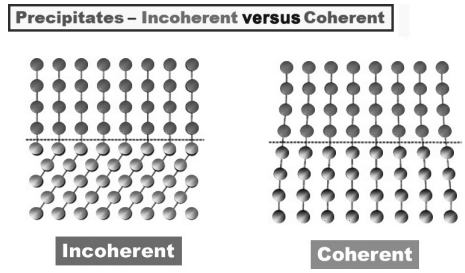

Figure 1.4.15 Comparison between interfacial dislocations and misfit dislocations, where the former can be mimicked by CD dislocations with an infinitesimal Burgers vector, thus normally yielding a long-range stress field, whereas the latter is represented by an array of isolated crystal dislocations with a finite Burgers vector introduced so as to relax the misfit situation.

Figure 1.4.15 provides an example eloquently comparing the two cases, which considers the interfaces of two atomic structures with slightly different lattice constants, like those with coherent precipitates (comparison of precipitates between coherent

https://doi.org/10.1017/9781108874069.003 Published online by Cambridge University Press

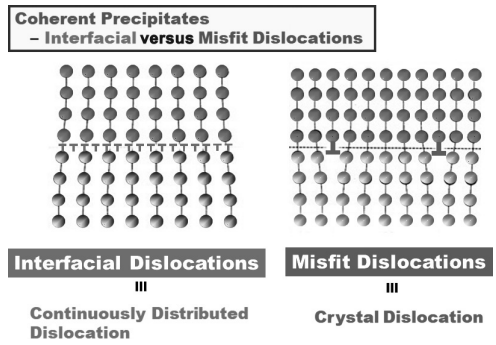

Figure 1.4.16 Comparison of precipitate-matrix interfaces between coherent and incoherent types.

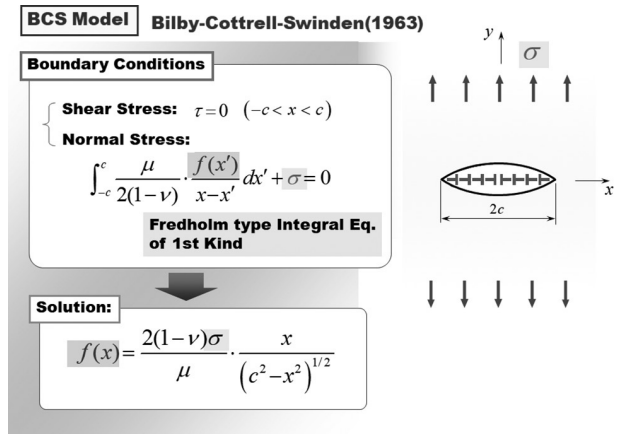

Figure 1.4.17 Application of the notion of CD dislocations to the crack problem (mode I type) (Bilby et al., 1963).

and incoherent types is given in Figure 1.4.16). The left denotes CD dislocations accommodating the misfit caused by the difference in the lattice spacing between the two phases, whereas the right is for the same interface but has been relaxed via an array of "crystal" dislocations. The former is called "interfacial" dislocations, while the latter "misfit" dislocations. As can be readily understood, the former case does not actually include "crystal" dislocation at all, meaning the illustrated dislocation array is imaginary. Instead, such a situation is well described via a stress field based on the dislocation theory.

Another example where such "imaginary" arrays of dislocations can work nicely as a model is "crack" (known as the BCS [Bilby-Cotterell-Swinden] model [Bilby et al., 1963]). Figure 1.4.17 displays a crack model via CD dislocations under mode I loading. The long-range nature of the stress field (as mentioned in Section 1.2.3.2) as well as the singularity of dislocations (in the present example, edge dislocations) are

https://doi.org/10.1017/9781108874069.003 Published online by Cambridge University Press

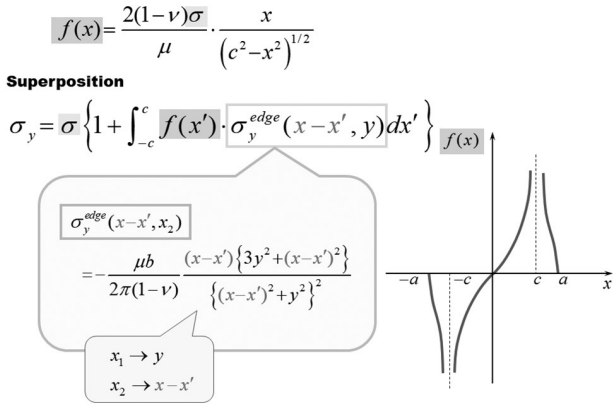

Figure 1.4.18 Analytical solution of the crack problem given in Figure 1.4.17 in the form of the distribution function of CD dislocations.

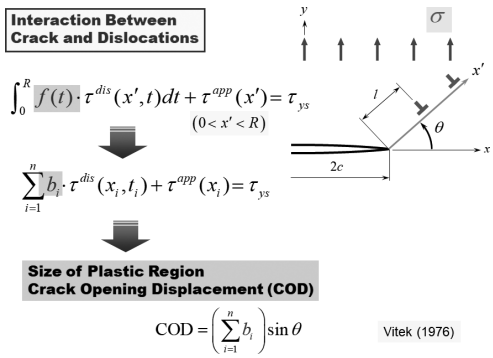

Figure 1.4.19 A crack expressed by CD dislocations interacting with emitted discrete dislocations for evaluating COD (Vitek, 1976b).

the reasons this model works well. As you can see, the assumed dislocation array is nothing more than the imaginary one, situated so as to satisfy both the crack-tip stress field and the boundary conditions. The corresponding distribution of dislocations to the crack is obtained by solving a kind of integral equation (1st Fredholm type) with respect to the distribution function $f(x)$ (inset of Figure 1.4.17), and is explicitly shown in Figure 1.4.18. Application examples of this technique to the fatigue-crack propagation problem can be found in Homma (1989) and Homma et al. (1984). Figure 1.4.19 displays an example of such applications to crack-tip problems, for the purpose of evaluating the crack-opening displacement (COD), where interactions with a discrete array of dislocations are considered (Vitek, 1976b). Elaborate achievements in dislocation theory-based fracture mechanics have been published as a monograph by Johannes Weertman (1996).

https://doi.org/10.1017/9781108874069.003 Published online by Cambridge University Press

Appendix A1 Energy Landscape for Dislocation Pairs

A1.1 Derivation of Peach–Koehler Equation (Formula)

Forces acting on dislocations are called the "Peach–Koehler (P–K) force" and the formula for calculating them is generally referred to as the "Peach–Koehler (P–K) equation." We show in the following a standard derivation process for the P–K equation. Note that the expression for the P–K force is a specific version of the energy-momentum tensor that applied to a dislocation line, just like the J-integral against a crack tip. We derive the P–K equation along this line in Chapter 7, in the context of the gauge field-based formalism of dislocations and defects; reference is also make to the J-integral.

Consider a straight dislocation line (the unit vector along with it is represented as ξ) with the Burgers vector $\boldsymbol{b}$ (inclined to it at an angle θ). Displacing the dislocation line by $\delta \boldsymbol{r}$, we measure the area swept by the operation as

$$d\boldsymbol{s} = \xi \times d\boldsymbol{r}. \tag{A1.1.1}$$

Under the application of stress $\boldsymbol{\sigma}$, the corresponding force acting on the dislocation line is calculated as

$$\boldsymbol{f}_{\xi} = \boldsymbol{\sigma} \cdot d\boldsymbol{s} = \boldsymbol{\sigma} \cdot \left(\xi \times d\boldsymbol{r}\right). \tag{A1.1.2}$$

Since the resultant shear displacement should be $\boldsymbol{b}$, the work done by the above operation is given by

$$\begin{aligned} \delta W &= \boldsymbol{f}_{\xi} \cdot \boldsymbol{b} \\ &= \left[\boldsymbol{\sigma} \cdot \left(\xi \times d\boldsymbol{r}\right)\right] \cdot \boldsymbol{b}, \end{aligned} \tag{A1.1.3}$$

$$\begin{aligned} &= \boldsymbol{b} \cdot \left[\boldsymbol{\sigma} \cdot \left(\xi \times d\boldsymbol{r}\right)\right] \\ &= \left(\boldsymbol{b} \cdot \boldsymbol{\sigma}\right) \cdot \left(\xi \times d\boldsymbol{r}\right) \\ &= \left(\boldsymbol{b} \cdot \boldsymbol{\sigma}\right) \times \xi \cdot d\boldsymbol{r} \\ &= \left(\boldsymbol{\sigma} \cdot \boldsymbol{b}\right) \times \xi \cdot d\boldsymbol{r}. \end{aligned} \tag{A1.1.4}$$

To obtain the last line, we used the invariance of the operation under cyclic permutations, that is, $\boldsymbol{a} \cdot \left(\boldsymbol{b} \times \boldsymbol{c}\right) = \left(\boldsymbol{a} \times \boldsymbol{b}\right) \cdot \boldsymbol{c} \equiv \left[\boldsymbol{abc}\right] = \left[\boldsymbol{bca}\right] = \left[\boldsymbol{cab}\right]$.

Therefore, the force per unit length of dislocation line is obtained as

$$\boldsymbol{f} = \left(\boldsymbol{\sigma} \cdot \boldsymbol{b}\right) \times \xi. \tag{A1.1.5}$$

This is called P–K equation, defining the P–K force (cf. Eq. (7.3.65) in Section 7.3.7). The corresponding index notation is expressed as

$$f_k = \in_{kji} \sigma_{jl} b_l \xi_i = - \in_{ijk} \sigma_{jl} b_l \xi_i. \tag{A1.1.6}$$

From this result, we immediately learn that the force on dislocation lines $\boldsymbol{f}$ always acts perpendicularly to them ξ, that is, $\boldsymbol{f} \perp \xi$.

From projections of the P–K force, $\boldsymbol{f}$, on the appropriate directions, we readily obtain the corresponding components (Hirth and Lothe, 1982). For the climb component, for example, it should be the direction both normal to $\boldsymbol{b}$ and ξ, which can be calculated by taking the inner product with the unitary vector of $(\boldsymbol{b} \times \xi)$, that is,

https://doi.org/10.1017/9781108874069.003 Published online by Cambridge University Press

$$f_{\text{climb}} = \boldsymbol{f} \cdot \frac{(\boldsymbol{b}\times\xi)}{|\boldsymbol{b}\times\xi|} = \frac{\left[(\sigma\cdot\boldsymbol{b})\times\xi\right]\cdot(\boldsymbol{b}\times\xi)}{|\boldsymbol{b}\times\xi|} \tag{A1.1.7}$$

Similarly, for the glide component we obtain

$$f_{\text{glide}} = \boldsymbol{f} \cdot \frac{\xi\times(\boldsymbol{b}\times\xi)}{|\boldsymbol{b}\times\xi|} = \frac{\left[(\sigma\cdot\boldsymbol{b})\times\xi\right]\cdot\left[\xi\times(\boldsymbol{b}\times\xi)\right]}{|\boldsymbol{b}\times\xi|}, \tag{A1.1.8}$$

because this should be normal to both ξ and $(\boldsymbol{b}\times\xi)$.

If the Burgers vector $\boldsymbol{b}$ is inclined to the dislocation line (ξ) at an angle θ, it is made up of two components, that is, the edge component, $\boldsymbol{b}_{\text{edge}} \equiv \boldsymbol{b}\sin\theta$, normal to ξ, and the screw component, $\boldsymbol{b}_{\text{screw}} \equiv \boldsymbol{b}\cos\theta$, parallel to ξ. The glide plane is defined as that which contains both the dislocation line and the Burgers vector.

Another important thing we should know is that applied stress σ can be replaced by more generalized stress, or the linear superposition of various contributions or origins. Such stress typically includes those produced by or associated with: (1) self-interaction of a curved dislocation, (2) image force in the presence of the free surface, and (3) interactions with other dislocations and defects.

$$\sigma = \sigma_{\text{ext}} + \sigma_{\text{self}} + \sigma_{\text{image}} + \sigma_{\text{int}} \tag{A1.1.9}$$

Correspondingly, we can deal with the P–K forces independently as

$$\boldsymbol{f} = \boldsymbol{f}_{\text{ext}} + \boldsymbol{f}_{\text{self}} + \boldsymbol{f}_{\text{image}} + \boldsymbol{f}_{\text{int}} \tag{A1.1.10}$$

A1.1.1 Examples of P–K Force

Consider a dislocation line $\xi = [0,0,1]^T$. Assuming edge and screw dislocation lines $\boldsymbol{b} = [b,0,0]^T$ and $\boldsymbol{b} = [0,0,b]^T$, respectively, we have, explicitly,

$$\begin{aligned}
\boldsymbol{f}_0 &= \left[\sigma_{11}b,\ \sigma_{12}b,\ \sigma_{13}b\right]^T \times [0,0,1]^T = \begin{vmatrix} \boldsymbol{e}_1 & \boldsymbol{e}_2 & \boldsymbol{e}_3 \\ \sigma_{11}b & \sigma_{12}b & \sigma_{13}b \\ 0 & 0 & 1 \end{vmatrix} \\
&= \left[\sigma_{12}b,\ -\sigma_{11}b,\ 0\right]^T \text{ for the edge dislocation.} \\
\boldsymbol{f}_0 &= \left[\sigma_{31}b,\ \sigma_{32}b,\ \sigma_{33}b\right]^T \times [0,0,1]^T \\
&= \left[\sigma_{32}b,\ -\sigma_{31}b,\ 0\right]^T \text{ for the screw dislocation.}
\end{aligned}$$

A1.2 Force Acting on a Parallel Dislocation Pair

Consider two straight-edge dislocation lines $\xi = [0,0,1]^T$ aligned in parallel. Assume they have $\boldsymbol{b}_A = [b_A,0,0]^T$ and $\boldsymbol{b}_B = [b_B,0,0]^T$, respectively, and are situated d apart. The interaction energy between the two edge dislocations A and B is given by

$$E_{\text{int}0}^{\text{edge}} = \int_V \sigma_A^{\text{edge}} : \varepsilon_B^{\text{edge}} d\boldsymbol{x} \tag{A1.2.1}$$

https://doi.org/10.1017/9781108874069.003 Published online by Cambridge University Press

Rewritten in terms of the eigenstrain, this becomes

$$\begin{aligned} E_{\text{int}0}^{\text{edge}} &= -\int_V \boldsymbol{\sigma}_A^{\text{edge}} : \varepsilon_B^{*\text{edge}} d\boldsymbol{x} \\ &= -\int_V \left(\sigma_{A\,21}^{\text{edge}} \varepsilon_{B\,21}^{*\text{edge}} + \sigma_{A\,12}^{edge} \varepsilon_{\boldsymbol{B}\,12}^{*\text{edge}} \right) d\boldsymbol{x} \end{aligned} \tag{A1.2.2}$$

Here, the eigenstrain components for the edge dislocation B is given by (see Eq. (A1.5))

$$\varepsilon_{B21}^{*\text{edge}} = \varepsilon_{B12}^{*\text{edge}} = \frac{b_B}{2} \delta\left(x_2 - d\right) H\left\{-\left(x_1 - x\right)\right\}, \tag{A1.2.3}$$

while the stress component is

$$\sigma_{A21}^{\text{edge}}\left(x_1, x_2\right) = \sigma_{A12}^{\text{edge}}\left(x_1, x_2\right) = \frac{\mu b_A}{2\pi\left(1-\nu\right)} \frac{x_1\left(x_1^2 - x_2^2\right)}{\left(x_1^2 + x_2^2\right)^2} \tag{A1.2.4}$$

Substituting them into Eq. (A1.2.2), we have

$$\begin{aligned} E_{\text{int}0}^{\text{edge}} &= -\frac{\mu b_A b_B}{2\pi(1-\nu)} \int_{-\infty}^{\infty}\int_{-\infty}^{\infty} \frac{x_1(x_1^2 - x_2^2)}{(x_1^2 + x_2^2)^2} \delta(x_2 - d) H\left\{-(x_1 - x)\right\} dx_1 dx_2 \\ &= -\frac{\mu b_A b_B}{2\pi(1-\nu)} \int_{-\infty}^{x} \frac{x_1(x_1^2 - d^2)}{(x_1^2 + d^2)^2} dx_1 \\ &= -\frac{\mu b_A b_B}{2\pi(1-\nu)} \left\{ \int_{-\infty}^{x} \frac{x_1^3}{(x_1^2 + d^2)^2} dx_1 - \int_{-\infty}^{x} \frac{d^2}{(x_1^2 + d^2)^2} dx_1 \right\}. \end{aligned}$$

The above integration can be analytically performed, provided the lower bound $-\infty$ is replaced by a reasonable value $-R$, as,

$$E_{\text{int}0}^{\text{edge}} = -\frac{\mu b_A b_B}{2\pi(1-\nu)} \left\{ \frac{1}{2} \ln\left(\frac{x_1^2 + d^2}{R^2 + d^2} \right) + \frac{d^2}{x_1^2 + d^2} - \frac{d^2}{R^2 + d^2} \right\}$$

A1.3 Elastic Strain Energy for Dislocations

Elastic strain energy for dislocations is given in two ways as

$$E^{\text{disloc}} = \frac{1}{2} \int_V \boldsymbol{\sigma} : \boldsymbol{\varepsilon}^e d\boldsymbol{x} = -\frac{1}{2} \int_V \boldsymbol{\sigma} : \varepsilon^* d\boldsymbol{x}, \tag{A1.3.1}$$

where ε^* represents the eigenstrain introduced by the dislocations. Correspondingly, $\boldsymbol{\sigma}$ in the second expression indicates the induced internal stress field.

By rewriting the elastic strain $\boldsymbol{\varepsilon}^e$ using $\boldsymbol{\varepsilon}^*$ in the first expression, that is, $\boldsymbol{\varepsilon}^e = \boldsymbol{\varepsilon} - \boldsymbol{\varepsilon}^*$, we have

$$\begin{aligned} E^{\text{disloc}} &= \frac{1}{2} \int_V \boldsymbol{\sigma} : \left(\boldsymbol{\varepsilon} - \boldsymbol{\varepsilon}^* \right) d\boldsymbol{x} \\ &= \frac{1}{2} \int_V \boldsymbol{\sigma} : \left(\frac{\partial \boldsymbol{u}}{\partial \boldsymbol{x}} \right) d\boldsymbol{x} - \frac{1}{2} \int_V \boldsymbol{\sigma} : \boldsymbol{\varepsilon}^* d\boldsymbol{x} \end{aligned} \tag{A1.3.2}$$

Here, $\boldsymbol{\sigma} : \boldsymbol{\varepsilon}$ in the first line can be replaced by $\boldsymbol{\sigma} : (\partial \boldsymbol{u} / \partial \boldsymbol{x})$ ($\partial \boldsymbol{u} / \partial \boldsymbol{x} \equiv \boldsymbol{\beta}$ is the distortion tensor that is generally asymmetric) because of the symmetry of $\boldsymbol{\sigma}$. The first term is further rewritten as follows by performing integration by parts:

https://doi.org/10.1017/9781108874069.003 Published online by Cambridge University Press

$$\begin{aligned}\frac{1}{2}\int_V \boldsymbol{\sigma} : \left(\frac{\partial \boldsymbol{u}}{\partial \boldsymbol{x}}\right) d\boldsymbol{x} &= \frac{1}{2}\int_s \boldsymbol{\sigma}\cdot\boldsymbol{u} ds - \frac{1}{2}\int_V \left(\frac{\partial \boldsymbol{\sigma}}{\partial \boldsymbol{x}}\right)\cdot \boldsymbol{u} d\boldsymbol{x} \\ &= \frac{1}{2}\int_s \boldsymbol{n}\cdot\boldsymbol{\sigma}\cdot\boldsymbol{u} ds - \frac{1}{2}\int_V div\boldsymbol{\sigma}\cdot\boldsymbol{u} d\boldsymbol{x} \\ &= 0.\end{aligned} \tag{A1.3.3}$$

Since we are looking at the internal stress that yields zero at the surface, the first term in the second line vanishes. The second term, on the other hand, also becomes zero because $div\boldsymbol{\sigma} = 0$ in the absence of body force. Therefore, we ultimately obtain the expression Eq. (A1.3.1) from Eq. (A1.3.2).

A1.4 Elastic Interaction Energy for a Dislocation Pair

For elasticity, the interaction between two dislocation fields can be evaluated by the linear superposition (the superposition principle if linear elasticity) as

$$\begin{aligned}E^{\text{disloc}} &= \frac{1}{2}\int_V \left(\boldsymbol{\sigma}_A + \boldsymbol{\sigma}_B\right) : \left(\boldsymbol{\varepsilon}_A^e + \boldsymbol{\varepsilon}_B^e\right) d\boldsymbol{x} \\ &= \frac{1}{2}\int_V \boldsymbol{\sigma}_A : \boldsymbol{\varepsilon}_A^e \, d\boldsymbol{x} + \frac{1}{2}\int_V \boldsymbol{\sigma}_B : \boldsymbol{\varepsilon}_B^e \, d\boldsymbol{x} + \frac{1}{2}\int_V \boldsymbol{\sigma}_A : \boldsymbol{\varepsilon}_B^e \, d\boldsymbol{x} + \frac{1}{2}\int_V \boldsymbol{\sigma}_B : \boldsymbol{\varepsilon}_A^e \, d\boldsymbol{x} \\ &\equiv E_A^{\text{disloc}} + E_B^{\text{disloc}} + E^{\text{int}}\end{aligned} \tag{A1.4.1}$$

Here, the interaction energy is defined as

$$\begin{aligned}E^{\text{int}} &\equiv \frac{1}{2}\int_V \boldsymbol{\sigma}_A : \boldsymbol{\varepsilon}_B^e \, d\boldsymbol{x} + \frac{1}{2}\int_V \boldsymbol{\sigma}_B : \boldsymbol{\varepsilon}_A^e \, d\boldsymbol{x} \\ &= \int_V \boldsymbol{\sigma}_A : \boldsymbol{\varepsilon}_B^e \, d\boldsymbol{x} = \int_V \boldsymbol{\sigma}_B : \boldsymbol{\varepsilon}_A^e \, d\boldsymbol{x},\end{aligned} \tag{A1.4.2}$$

where $\boldsymbol{\sigma}_A : \boldsymbol{\varepsilon}_B^e = \boldsymbol{\sigma}_B : \boldsymbol{\varepsilon}_A^e$ is used. Using the eigenstrain formalism, we alternatively have

$$E^{\text{int}} = -\int_V \boldsymbol{\sigma}_A : \boldsymbol{\varepsilon}_B^* \, d\boldsymbol{x} \quad \left(= -\int_V \boldsymbol{\sigma}_B : \boldsymbol{\varepsilon}_A^* \, d\boldsymbol{x}\right). \tag{A1.4.3}$$

A1.5 Examples of Dislocations in Eigenstrain Representation

Let us consider a straight-edge dislocation on the $x_1 - x_2$ plane. We can introduce it by the following operation.

A cut is made in the $x_1 < 0$ region (Figure 1.2.16) first, and then the opposite surfaces of the cut are welded to restore the continuity after displacing them relative to each other by $\boldsymbol{b}$. This results in an edge dislocation situated at the origin with the Burgers vector $\boldsymbol{b} = (b,0,0)$. This procedure is the so-called Volterra operation. Since the displacement caused by this operation is $\boldsymbol{u} = (b,0,0)$, the strain components are given as

$$\varepsilon_{21}^{*\text{edge}} = \varepsilon_{12}^{*\text{edge}} = \frac{b}{2}\delta(x_2)H\left(-x_1\right), \tag{A1.5.1}$$

https://doi.org/10.1017/9781108874069.003 Published online by Cambridge University Press

otherwise zero.

Here, $\delta(x)$ is the Dirac delta function and $H(x)$ represents the Heaviside step function. They are defined respectively as

$$\delta(x)=\begin{cases}\infty & (at\ \ x=0)\\ 0 & (at\ \ x\neq 0)\end{cases}\ \int_{-a}^{a}\delta(x)dx=1\ \ (a>0), \tag{A1.5.2}$$

and

$$H(x)=\begin{cases}0 & (at\ \ x<0)\\ 1/2 & (at\ \ x=0)\\ 1 & (at\ \ x>0)\end{cases}. \tag{A1.5.3}$$

There is a following relationship between the two functions, that is,

$$\delta(x)=\frac{dH(x)}{dx}\left(\Leftrightarrow H(x)=\int_{-\infty}^{x}\delta(x)dt\right) \tag{A1.5.4}$$

A1.6 Energy Landscape of Edge Dislocation Pairs

Consider a pair of straight-edge dislocations on the x_1-x_2 plane, as depicted in the inset in Figure A1.6.1, where relative angles θ_1 and θ_2 are ranged from 0 to 180°, as well as the mutual distance between them. Here, $\theta=180°$ corresponds to

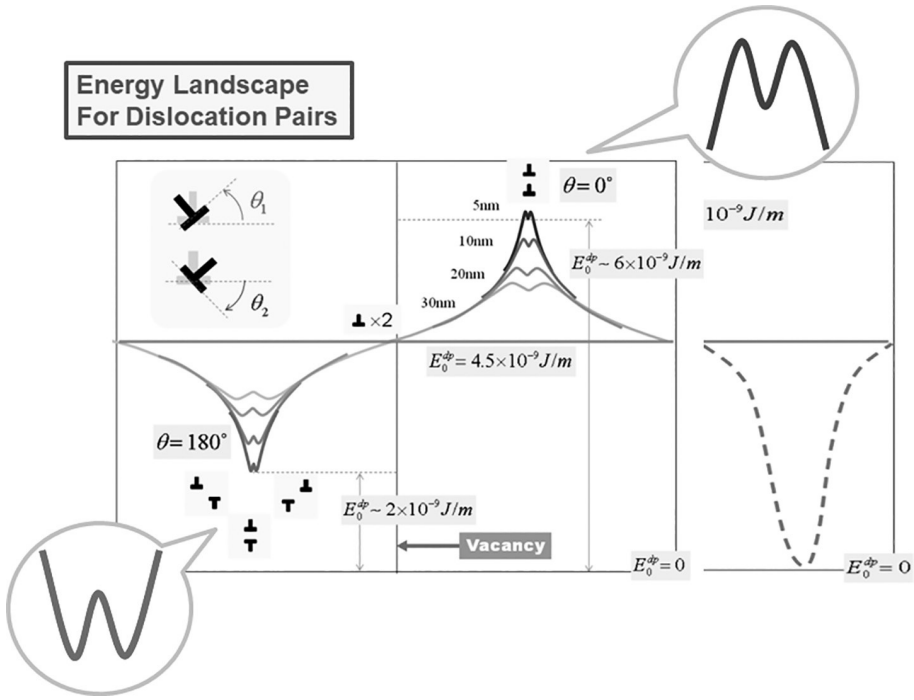

Figure A1.6.1 Energy landscape for pairwise configurations of edge dislocations.

https://doi.org/10.1017/9781108874069.003 Published online by Cambridge University Press

vacancy-type dipole configuration, while $\theta = 0°$ represents the monopole alignment. The former, with the 45° alignment, yields the minimum energy, as shown in the bottom-left region in Figure A1.6.1, whereas the latter takes the maximum, as displayed in the middle-upper region. With the mutual distance tending to 0 for the dipole configuration, the energy decreases down to 0, as shown in the bottom-right region, demonstrating roughly a double-well-type energy landscape responsible for the pairwise interaction. This is assumed in Chapter 10 for the derived effective theory with respect to the annihilated field.

A1.7 Euler Angles

Euler angles can uniquely specify 3D rotations of the targeted coordinates with respect to a reference coordinate system by using three angles. In metallurgy, there are two conventions for defining the Euler angles, that is, Bunge and Roe (Nagashima, 1984). Throughout the book, we use the Bunge-type definition, represented conventionally by $(\varphi_1, \Phi, \varphi_2)$. Note, the Roe convention uses (ψ, θ, ϕ) instead.

An easy way to understand Euler angles is to break down the associated coordinate transformation process into three steps, as illustrated in Figure A1.7.1, that is, from (X_A, Y_A, Z_A) to (X_B, Y_B, Z_B). Since each step is simply a rotation about an axis, all we have to consider is the order of the axes. For the Bunge convention, we choose $Z \to X \to Z$. This is the very reason for this style to use $\varphi_1 \to \Phi \to \varphi_2$ as the notation. Note that, in the Roe style, the choice is $Z \to$ "Y" $\to Z$, thus a simple set of conversions holds between the two conventions, as $\varphi_1 = \psi + \pi/2$, $\Phi = \theta$, $\varphi_2 = \phi + \pi/2$.

The three steps are as broken down sequentially as follows, as displayed in Figure A1.7.1(a) and (b). The first step is the rotation about Z_A-axis, specified by the angle φ_1, given by

$$\begin{Bmatrix} x' \\ y' \\ z' \end{Bmatrix} = \begin{bmatrix} \cos\varphi_1 & \sin\varphi_1 & 0 \\ -\sin\varphi_1 & \cos\varphi_1 & 0 \\ 0 & 0 & 1 \end{bmatrix} \begin{Bmatrix} X_A \\ Y_A \\ Z_A \end{Bmatrix} \equiv [\varphi_1] \begin{Bmatrix} X_A \\ Y_A \\ Z_A \end{Bmatrix}, \tag{A1.7.1}$$

which transforms from (X_A, Y_A, Z_A) to (x', y', z'). Likewise, since the second step refers to the rotation about the "X_A-axis," specified by Φ, we have

$$\begin{Bmatrix} x'' \\ y'' \\ z'' \end{Bmatrix} = \begin{bmatrix} 1 & 0 & 0 \\ 0 & \cos\Phi & \sin\Phi \\ 0 & -\sin\Phi & \cos\Phi \end{bmatrix} \begin{Bmatrix} x' \\ y' \\ z' \end{Bmatrix} \equiv [\Phi] \begin{Bmatrix} x' \\ y' \\ z' \end{Bmatrix}, \tag{A1.7.2}$$

expressing the transformation from (x', y', z') to (x'', y'', z''). Lastly, the third step is again the rotation about the z'-axis with angle φ_2, which is given by the same form as that for the first step, that is,

$$\begin{Bmatrix} X_B \\ Y_B \\ Z_B \end{Bmatrix} = \begin{bmatrix} \cos\varphi_2 & \sin\varphi_2 & 0 \\ -\sin\varphi_2 & \cos\varphi_2 & 0 \\ 0 & 0 & 1 \end{bmatrix} \begin{Bmatrix} x'' \\ y'' \\ z'' \end{Bmatrix} \equiv [\varphi_2] \begin{Bmatrix} x'' \\ y'' \\ z'' \end{Bmatrix}. \tag{A1.7.3}$$

https://doi.org/10.1017/9781108874069.003 Published online by Cambridge University Press

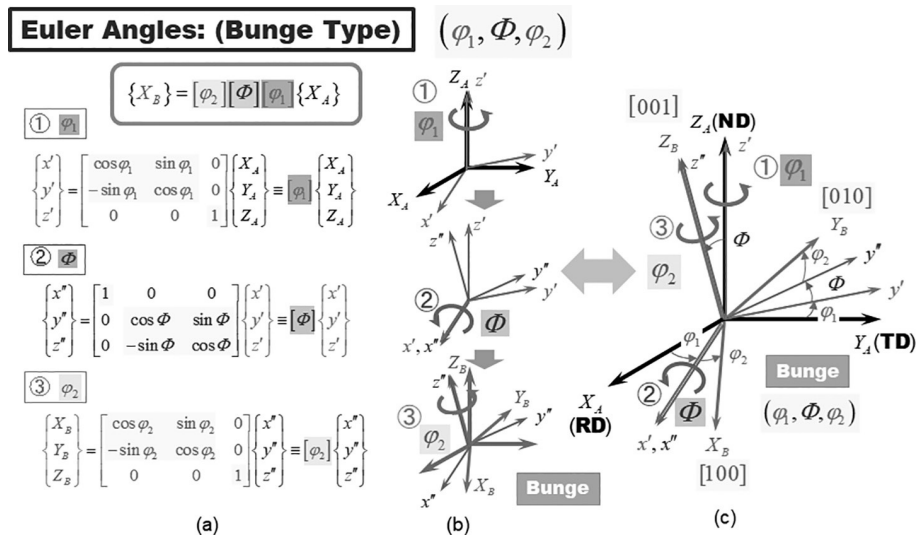

Figure A1.7.1 A series of processes obtaining Euler angles (Bunge style).

By combining the above three processes, Eqs. (A1.7.1) to (A1.7.3), we define the Euler angles of Bunge type as

$$\{X_B\} = [\varphi_2][\Phi][\varphi_1]\{X_A\}, \tag{A1.7.4}$$

$$\Leftrightarrow \begin{Bmatrix} X_B \\ Y_B \\ Z_B \end{Bmatrix} = \begin{bmatrix} \cos\varphi_2 & \sin\varphi_2 & 0 \\ -\sin\varphi_2 & \cos\varphi_2 & 0 \\ 0 & 0 & 1 \end{bmatrix} \begin{bmatrix} 1 & 0 & 0 \\ 0 & \cos\Phi & \sin\Phi \\ 0 & -\sin\Phi & \cos\Phi \end{bmatrix} \begin{bmatrix} \cos\varphi_1 & \sin\varphi_1 & 0 \\ -\sin\varphi_1 & \cos\varphi_1 & 0 \\ 0 & 0 & 1 \end{bmatrix} \begin{Bmatrix} X_A \\ Y_A \\ Z_A \end{Bmatrix}$$

$$= \begin{bmatrix} \cos\varphi_2\cos\varphi_1 - \sin\varphi_2\cos\Phi\sin\varphi_1 & \cos\varphi_2\sin\varphi_1 + \sin\varphi_2\cos\Phi\cos\varphi_1 & \sin\varphi_2\sin\Phi \\ -\sin\varphi_2\cos\varphi_1 - \cos\varphi_2\cos\Phi\sin\varphi_1 & -\sin\varphi_2\sin\varphi_1 + \cos\varphi_2\cos\Phi\cos\varphi_1 & \cos\varphi_2\sin\Phi \\ \sin\Phi\sin\varphi_1 & -\sin\Phi\cos\varphi_1 & \cos\Phi \end{bmatrix}$$

$$\times \begin{Bmatrix} X_A \\ Y_A \\ Z_A \end{Bmatrix} \tag{A1.7.5}$$

Notice that the first two steps determine the [001] direction away from the referential $Z_A - X_A$ (ND-TD) plane, as conformed in Figure A1.7.1(c). Therefore, if we assume we skip the first step, the [001] direction stays on the $Z_A - X_A$ (ND-TD) plane, while the [100] direction coincides with the X_A (RD) axis. Based on this consideration, we obtain a simple schematic, as inserted in Figure 1.3.14(d) and Figure 1.4.14(d), indicating a crystal orientation with respect to the cube axes by using the remaining two angles (Φ, φ_2). This is convenient for quick and intuitive recognitions of crystal orientations, for example, on standard triangles (Figure 1.3.14(c) and Figure 1.4.14(c)). In this case, of course, the other two crystal orientations are indefinite, and should be specified by φ_1.

https://doi.org/10.1017/9781108874069.003 Published online by Cambridge University Press